



Small Interfering RNA Imaging Probes for Neurological Applications

Citation

Ifediba, Marytheresa Akuigwe. 2012. Small Interfering RNA Imaging Probes for Neurological Applications. Doctoral dissertation, Harvard University.

Permanent link

<http://nrs.harvard.edu/urn-3:HUL.InstRepos:10445637>

Terms of Use

This article was downloaded from Harvard University's DASH repository, and is made available under the terms and conditions applicable to Other Posted Material, as set forth at <http://nrs.harvard.edu/urn-3:HUL.InstRepos:dash.current.terms-of-use#LAA>

Share Your Story

The Harvard community has made this article openly available.
Please share how this access benefits you. [Submit a story](#).

[Accessibility](#)

© 2012 Marytheresa Akuigwe Ifediba
All rights reserved.

Small Interfering RNA Imaging Probes for Neurological Applications

Abstract

Small interfering RNAs (siRNAs) have emerged as a potent new class of therapeutics that regulate gene expression through sequence-specific inhibition of mRNA translation. Clinical trials of siRNAs have highlighted the need for robust delivery and detection techniques that would enable the application of these therapeutics to increasingly complex diseases and organ systems. Here we detail the generation and evaluation of siRNA-based optical and magnetic resonance imaging (MRI) contrast agents for the treatment of neurological diseases, including ischemic stroke and glioblastoma multiforme brain cancer.

First, we designed and tested a fluorescent probe for neuroprotection in the setting of stroke that consists of siRNA complexed with myristoylated poly-arginine peptide (MPAP). MPAP, a peptide shown to cross cell membranes and the blood brain barrier, promoted robust internalization of siRNA by neurons in vitro and in mouse brain after intracerebral injection. Cellular uptake of MPAP-siRNA probes directed against a protein implicated in stroke pathology, c-Src, led to statistically-significant reductions of endogenous mRNA expression. The neuroprotective potential of probes was tested in a mouse model of ischemic stroke.

Second, superparamagnetic iron oxide nanoparticles were investigated as vectors for siRNA delivery to glioblastoma multiforme brain tumors. Nanoparticles were designed to enhance chemotherapeutic treatment of tumors through siRNA-mediated knockdown of O6-methylguanine–DNA methyltransferase (MGMT), a protein

implicated in glioblastoma chemotherapy resistance. The iron oxide core of nanoparticles rendered them detectable by MRI while fluorescent labeling was used for optical imaging. Functionalizing nanoparticles with the peptide chlorotoxin enabled tumor targeting and cellular accumulation of probe. Probe uptake was accompanied by reductions in MGMT activity and enhanced cellular responses to the chemotherapeutic temozolomide. Nanoparticles were tested in an orthotopic glioblastoma mouse model, where intratumoral administration proved effective in suppressing MGMT expression and tumor volume. These studies serve as proof-of-principle that siRNA-based imaging agents can be used as therapeutic tools for diseases of the central nervous system.

Table of Contents

List of Figures.....	vii
List of Tables	ix
Acknowledgments	x
1. In vivo Imaging of the Systemic Delivery of Small Interfering RNA.....	1
1.1 Introduction	1
1.2 Naked and Chemically-Modified siRNA Delivery	3
1.3 Lipid-Based Delivery	5
1.4 Peptide- and Polymer-Based Delivery	9
1.5 Nanoparticle-Based Delivery	13
1.6 Conclusion.....	20
2. Small Interfering RNA Fluorescent Probes for Ischemic Stroke Therapy	21
2.1 Introduction	21
2.1.1 RNA Interference and Cell Penetrating Peptide (CPP) Delivery	22
2.1.2 MPAP-siRNA Stroke Therapeutics	27
2.2 Experimental Procedures	29
2.2.1 MPAP Probe Synthesis	29
2.2.2 Gel Mobility Shift Assay and Zeta Potential Characterization	30
2.2.3 Serum Stability	31
2.2.4 Cell Culture and MPAP-Mediated siRNA Delivery	31
2.2.5 Cytotoxicity Assays	33
2.2.6 Fluorescence-Activated Cell Sorting (FACS)	34
2.2.7 Fluorescence Confocal Microscopy of MPAP-siRNA Delivery	35
2.2.8 Real-Time Quantitative RT-PCR	35
2.2.9 Middle Cerebral Artery Occlusion (MCAo) Surgery	36
2.2.10 Evans Blue Dye Evaluation of Blood-Brain Barrier Permeability	42
2.2.11 Therapeutic Treatment with MPAP-Src: Systemic Administration	43
2.2.12 Therapeutic Treatment with MPAP-Src: Intracerebral Injection	44
2.2.13 Concentration Dependence of Intracerebrally-Injected MPAP-Src	45
2.2.14 Stroke Volume Assessment by Triphenyltetrazolium Chloride (TTC) Staining.....	46
2.2.15 Behavioral Testing	47
2.2.16 Western Blot Analysis	48
2.2.17 Fluorescence Optical Imaging	49
2.3 Results	49
2.3.1 Characterization of MPAP-Src Probes	49
2.3.2 In Vitro Testing of MPAP-Src Probes.....	51
2.3.3 MPAP Delivery in Experimental Stroke	59
2.3.4 The Efficacy of MPAP-Src Pretreatment in Experimental Stroke	62
2.3.5 The Therapeutic Potential of MPAP-Src Administered Post-Stroke	71
2.3.6 The Efficacy of MPAP-Src Intracerebral Injection in Experimental Stroke	73
2.4 Discussion.....	77
2.4.1. Alternative Therapeutic Targets	85
3. Theranostic imaging probes for the treatment of malignant brain tumors.	94
3.1 Introduction	94
3.2 Experimental Procedures	98
3.2.1 Theranostic Probe Synthesis	98
3.2.2 Characterization of siMGMT-CLX-NP Probes	100

3.2.3 In vitro siMGMT-CLX-NP Probe Uptake.....	101
3.2.4 Optical/MR Imaging of Cellular Phantoms	102
3.2.5 Real Time Quantitative RT-PCR	103
3.2.6 Western Blot Analysis	104
3.2.7 MGMT Activity Assay	104
3.2.8 Synergistic Effect of siRNA and Temozolomide Treatment.....	106
3.2.9 Establishment of Flank Tumor Xenografts.....	106
3.2.10 Establishment of Orthotopic Tumor Xenografts	107
3.2.11 In vivo Magnetic Resonance Imaging	108
3.2.12 Nanoparticle/Chemotherapy Treatment.....	109
3.2.13 Histological Staining	111
3.3 Results	113
3.3.1 Characterization of siMGMT-CLX-NP Probes	113
3.3.2 In vitro siMGMT-CLX-NP Probe Uptake.....	113
3.3.3 Bioactivity of siMGMT-CLX-NPs	119
3.3.4 Intravenous Delivery of siMGMT-CLX-NP Probes in Glioblastoma Model	124
3.3.5 Intratumoral Delivery of siMGMT-CLX-NP Probes in Glioblastoma Model	128
3.4 Discussion.....	136
4. References.....	141

List of Figures

Figure 1.1 Multimodality imaging of NIR-labeled iron oxide nanoparticle (MN-NIRF-siGFP) delivery to tumors.....	15
Figure 1.2 Efficacy of siGFP delivered with iron oxide nanoparticles.....	16
Figure 1.3 Tumor-targeted siRNA delivery with iron oxide nanoparticles (MN-EPPT-siBIRC5).....	17
Figure 2.1. Middle cerebral artery occlusion (MCAo) surgery with cerebral blood flow monitoring.....	38
Figure 2.2 Gel mobility shift assay and serum stability.....	50
Figure 2.3. Flow cytometry.....	52
Figure 2.4. Cellular uptake of MPAP-Src probes.....	54
Figure 2.5. Uptake mechanism of MPAP-Src.....	55
Figure 2.6. Bioactivity of MPAP-Src probes.....	57
Figure 2.7. Cytotoxicity Assays.....	58
Figure 2.8. The effect of occlusion duration on infarct volume.....	61
Figure 2.9. Ex vivo detection of Evans blue dye extravasation.....	63
Figure 2.10. Fluorescence imaging of MPAP-Src probe delivery.....	64
Figure 2.11. Fluorescence imaging of MPAP probe pre-stroke treatment.....	67
Figure 2.12. Infarct volumes and cerebral edema.....	70
Figure 2.13. MPAP-src post-stroke treatment effects.....	72
Figure 2.14. Intracerebral MPAP-Src treatment effects.....	74
Figure 2.15. Concentration dependence of intracerebral MPAP-Src treatment.....	76
Figure 3.1. Scheme for the preparation of multifunctional nanoparticle probes.....	99
Figure 3.2. The siRNA content and R_2 relaxivity of siMGMT-CLX-NP probes.....	114
Figure 3.3. Iron uptake assay.....	116
Figure 3.4. Cellular distribution of siMGMT-CLX-NPs.....	117
Figure 3.5. Optical and MR imaging of cell pellets.....	118

Figure 3.6. Bioactivity of probes.....	120
Figure 3.7. Synergic effects of siMGMT-CLX-NP and temozolomide (TMZ) treatment.....	123
Figure 3.8. Establishment of T98G xenograft model.....	125
Figure 3.9. Intravenous delivery of siMGMT-CLX-NPs.....	127
Figure 3.10. T98G and U87MG tumor vasculature.....	129
Figure 3.11. Intratumoral siMGMT-CLX-NP delivery and efficacy.....	130
Figure 3.12. Bioactivity of siMGMT probes in glioblastoma tumors.....	133
Figure 3.13. Histological staining of T98G brain tumors.....	135

List of Tables

Table 2.1 Cell Penetrating Peptides.....	24
Table 2.2. Potential Targets for Neuroprotection in Stroke.	86

Acknowledgments

I would like to acknowledge with the deepest gratitude the support of my mother,
Karen Goble Ifediba.

1. In vivo Imaging of the Systemic Delivery of Small Interfering RNA

1.1 Introduction

The discovery of small RNA molecules that regulate gene expression has had a transformative impact on the study of gene function and has led to the emergence of a new class of RNA-based therapeutics being investigated in human trials. Double-stranded small interfering RNAs (siRNAs) mediate gene silencing through complementary base-pairing, leading to potent, sequence-specific suppression of mRNA translation (Fire, Xu et al. 1998; Elbashir, Harborth et al. 2001). This process, known as RNA interference (RNAi), can theoretically be harnessed to treat any pathology caused by aberrant protein. Effective RNAi therapy requires that exogenous siRNAs be introduced into affected cells in quantities sufficient to inhibit target gene expression and improve clinical outcome. This is complicated by several factors, including rapid nuclease degradation of siRNA molecules after exposure to blood and a negatively-charged sugar phosphate backbone that impedes siRNA translocation across cellular and biological membranes. The first clinical trials of siRNA therapeutics circumvented these delivery issues by focusing on organ systems that were amenable to simple topical or local drug administration, such as the eyes, respiratory system, and skin (Vaishnav, Gollob et al. 2010). However, for RNAi therapy to expand to additional disease targets, it is necessary that robust, site-specific delivery of siRNAs be perfected. To this end, extensive research has focused on the development of vector systems that stabilize siRNA while promoting siRNA targeting, uptake and expression following systemic administration. Chemical modifications of siRNA duplexes, novel injection techniques, and lipid-, polymer- and nanoparticle-based delivery vehicles have all proven effective in

improving the bioavailability of siRNAs in a variety of disease models. In contrast, significantly less focus has been placed on developing methods to non-invasively image the delivery and actions of siRNAs in vivo, a process that will be important in a clinical setting where understanding the pharmacodynamics of drugs is crucial.

During the past decade, several studies have illustrated how the versatility of siRNA therapies expands once molecular imaging capabilities are incorporated. The first demonstration of siRNA efficacy in mammalian cell culture employed bioluminescent reporter genes to assess silencing (Elbashir, Harborth et al. 2001). A year later, whole body bioluminescence imaging of adult mice following hydrodynamic co-injection of luciferase plasmid and siRNA enabled noninvasive monitoring and quantification of RNA interference (McCaffrey, Meuse et al. 2002). Imaging of reporter gene expression has since been used to acquire organ-specific siRNA silencing profiles (Lewis, Hagstrom et al. 2002), to evaluate nuclease stabilization of siRNAs for in vivo applications (Layzer, McCaffrey et al. 2004; Bartlett and Davis 2007), and to elucidate biological pathways (Zhang, Safran et al. 2004). More recently, the focus of the siRNA imaging field has shifted to include clinically-relevant imaging modalities. Accordingly, siRNAs are increasingly being integrated into contrast agents for detection by radionuclide or magnetic resonance (MR) imaging. This requires flexible siRNA delivery systems that stabilize siRNA molecules while acting as a platform for modification by targeting or imaging reporter groups for improved probe contrast and specificity. In this chapter, we review the current status of siRNA imaging and therapy, with particular emphasis placed on the novel methods that have been developed to improve siRNA delivery and detection following administration in vivo.

1.2 Naked and Chemically-Modified siRNA Delivery

The earliest examples of siRNA imaging utilized reporter gene systems to evaluate the handling of synthetic naked siRNAs in mice (Lewis, Hagstrom et al. 2002; McCaffrey, Meuse et al. 2002). These studies used an *in vivo* transfection strategy originally developed for plasmid DNA, hydrodynamic high-pressure tail vein injection (Liu, Song et al. 1999), to promote cellular delivery of naked siRNAs and luciferase-expressing plasmids. The primary site of siRNA uptake following hydrodynamic injection was the liver, with suppression of luciferase gene expression of 80-90% (Lewis, Hagstrom et al. 2002; McCaffrey, Meuse et al. 2002). Though these delivery and imaging methods are impractical in a clinical setting, they have been instrumental in the transition to *in vivo* siRNA therapies. This was excellently demonstrated in a report that investigated luciferase knockdown efficiency as a function of siRNA dose, siRNA delivery method, and target cell division rate (Bartlett and Davis 2006). By monitoring luminescence knockdown kinetics *in vitro* and *in vivo* in both nondividing hepatocytes (transfected by hydrodynamic injection) and rapidly dividing tumor cells (transfected using a targeted siRNA carrier), Bartlett et al. was able to show that the duration of gene silencing is dictated by cell division, not intracellular siRNA half-life. These results formed the basis of a mathematical model that predicts siRNA efficacy and persistence as target protein half-life, target cell doubling time, and siRNA dosing parameters are varied, providing a valuable aid for the design of future experiments.

An alternative method of naked siRNA delivery that has been investigated by imaging is *in vivo* electroporation (Takabatake, Isaka et al. 2005; Golzio, Mazzolini et al. 2007). In rats, selective uptake of siRNA by kidney mesangial cells was promoted by

applying electrical pulses to the renal artery following co-injection of luciferase-expressing plasmids and siRNA (Takabatake, Isaka et al. 2005). Bioluminescence imaging confirmed significant luciferase reduction of 70%. Similarly, fluorescence imaging has been used to investigate *in vivo* electroporation in tumors expressing an EGFP reporter gene (Golzio, Mazzolini et al. 2007). Electrical pulses applied to tumors following direct microinjection of siRNAs mediated intracellular delivery and a modest degree of silencing in a mouse subcutaneous tumor model.

Chemical modification of naked siRNAs has proven effective in extending the half-life of siRNAs exposed to serum (Braasch, Jensen et al. 2003; Czauderna, Fechtner et al. 2003), helping them to persist in the blood following conventional systemic injection. Additionally, several groups have chemically-modified siRNAs to include radioactive tracers to extend their application to clinically-relevant imaging modalities. Liu et al. created a tracer for single photon emission computed tomography (SPECT) imaging by conjugating chelator S-Acetyl N-hydroxysuccinimide (NHS) hydrazine nicotinamide (HYNIC) to naked siRNAs for labeling with ^{99m}Tc (Liu, Ding et al. 2007). Precise tissue distributions of ^{99m}Tc -siRNAs were acquired by analysis of whole body scintigraphic images of mice bearing human kidney cancer tumors. An alternative chelator, N-hydroxysuccinimide-mercaptoacetyltriglycine (NHS-MAG3), for ^{99m}Tc radiolabeling of siRNA has similarly been used to generate siRNA biodistributions in tumor-bearing mice (Kang, Wang et al. 2010). Viel et al. performed a detailed investigation of the bioavailability and pharmacokinetics of siRNAs labeled with a positron emitter, fluorine-18, and subsequently assessed the *in vivo* effects of their probes (Viel, Boisgard et al. 2008). Tissue distributions and blood persistence and stability of

siRNAs with different chemically-modified riboses were performed, and time-activity curves of siRNA in rat organs were generated from dynamic whole-body positron emission tomography (PET) scans. In vivo RNA interference of the siRNAs was assessed using a luciferase-expressing xenograft nude mouse model, which resulted in very small, though significant, decreases in luciferase expression in tumors 48 hours after siRNA injection. Results from these studies serve as an important proof-of-concept that siRNAs can be effectively adapted for nuclear imaging and provide valuable insight into the in vivo trafficking and stability of the resulting probes. They also highlight the importance of incorporating a method of delivery assistance into siRNA probes to overcome limited cellular uptake following intravenous administration. The sections below detail the different vector systems that have been investigated as integrated imaging and delivery platforms for improved delivery of siRNA to target tissues.

1.3 Lipid-Based Delivery

Lipid-based vectors have been used as transfection agents for oligonucleotides for over two decades (Felgner, Gadek et al. 1987), preferred for their efficiency, low immunogenicity, and straightforward preparation. Recent success of stable nucleic acid lipid particles (SNALPs) for siRNA delivery to the liver of non-human primates has set lipid-based siRNA carriers apart as promising candidates for clinical translation (Zimmermann, Lee et al. 2006; Frank-Kamenetsky, Grefhorst et al. 2008). Most lipid carriers are cationic liposomes that electrostatically complex with siRNAs, spontaneously associate with negatively-charged cell membranes and become endocytosed by cells. Upon cell entry, liposomes are believed to destabilize endosomal membranes, enabling delivery of siRNAs to the cytoplasm where they are processed by RNAi machinery (Xu

and Szoka 1996). Liposome size, stability, and circulation half-life can readily be varied by changing lipid content and by adding surface modifications. Therefore, lipid nanoparticles are particularly valuable from a molecular imaging perspective because functional groups can be complexed or covalently grafted to form targeted or labeled probes.

The simplest lipid-based imaging probes consist of fluorescently-tagged siRNAs that have been either encapsulated by or complexed with liposomes. Though the utility of this approach is generally limited to *ex vivo* microscopic examinations of excised tissues, studies that have used it have clarified aspects of siRNA delivery including siRNA organ distributions, cellular handling, clearance and dosing (Sioud and Sorensen 2003; Landen, Chavez-Reyes et al. 2005; Morrissey, Lockridge et al. 2005; Santel, Aleku et al. 2006). The addition of targeting groups to fluorescently-labeled liposomes has been shown to increase the bioavailability of siRNA duplexes in even the most inaccessible tissues, as was demonstrated recently when cationic liposomes complexed with siRNA and peptide derived from rabies virus glycoprotein were delivered across the mouse blood-brain barrier, resulting in 25% suppression of cellular prion protein in the brain (Pulford, Reim et al. 2010).

In vivo imaging of siRNA delivery using lipids has routinely been investigated with fluorochromes in the near infrared (NIR) range and luciferase reporter genes. One approach incorporated NIR fluorochrome-labeled siRNA into nanoparticles through electrostatic interaction with lipidoids, a class of lipid-like molecules formed by the coupling of aliphatic side chains to an amine backbone (Goldberg, Xing et al. 2011). Intraperitoneal injection of the lipidoid-siRNA formulation resulted in significant tumor

uptake of nanoparticles in a murine ovarian cancer model as assessed by whole body optical imaging. Additionally, dual siRNA treatment promoted the induction of tumor apoptosis and ultimately increased animal survival. Whole body optical imaging was also used to investigate a siRNA ‘wraposome’ consisting of a cationic liposome and Cy5-labeled siRNA complex surrounded by a PEGylated, neutral lipid bilayer envelope that prolongs the systemic half-life of siRNA and reduces toxicity (Yagi, Manabe et al. 2009). In mice bearing a human prostate carcinoma tumor, NIR imaging revealed retention of wraposomes in the tumor 11 days after administration by tail vein injection. Wraposome siRNA mediated mRNA and protein knockdown of transcription factor *Klf5* in tumors, leading to reductions in both angiogenesis and tumor growth. Another group developed a mouse model with liver-specific expression of a luciferase reporter to non-invasively screen a library of lipid nanoparticles for siRNA delivery (Tao, Davide et al. 2010). Lipid nanoparticles composed of different cationic lipid, polyethylene glycol (PEG) and cholesterol contents were evaluated for their efficiency in carrying siRNA to hepatocytes following systemic injection. Whole body bioluminescence imaging was used to select the optimized delivery vehicle, capable of up to 90% silencing of luciferase-specific siRNA for 10 days. A combination of bioluminescence and optical imaging was used in a study that targeted cationic liposomes to the liver using apolipoprotein A-I (Kim, Shin et al. 2007). Biodistribution of the liposomes was evaluated using two methods, including whole body optical imaging of near infrared dye-labeled liposomes and gamma camera evaluation of ¹³¹I-labeled liposomes. In addition to these methods, bioluminescence imaging was used to demonstrate 70% gene silencing by liposomes when loaded with luciferase-specific siRNA.

Liposomes have also been adapted for clinical imaging modalities. The biodistribution of systemically-administered cationic liposome/siRNA complexes has been acquired through radiolabeling of the siRNA component with positron emitter ^{18}F [SFB] and subsequent PET imaging (Hatanaka, Asai et al. 2010). Other groups have taken advantage of the functionalization and encapsulation properties of liposomes to incorporate multiple imaging moieties into probes. Mikhaylova et al. developed a multimodal imaging probe by incorporating fluorescently-labeled siRNA into liposomes (Mikhaylova, Stasinopoulos et al. 2009). Liposomes were subsequently loaded with gadolinium and iron oxide MRI contrast agents. Iron oxide lipoplexes reduced endogenous COX-2 protein expression when tested in cultured cells. Although siRNA efficacy was not evaluated, the authors demonstrated that the lipoplexes formed effective imaging probes *in vivo*, first, by monitoring the biodistribution of liposomes with optical imaging and second, by evaluating delivery to tumor cells in a breast cancer xenograft model with MRI. Another multimodal imaging approach used gadolinium- and rhodamine-labeled lipids as constituents during liposome preparation to form MR-sensitive, fluorescent delivery probes (Kenny, Kamaly et al. 2011). Therapeutic probes were created when siRNA directed against survivin, a member of the inhibitor of apoptosis family and potent antitumoral target, were added to the liposomes. The resulting probes, termed liposome-entrapped siRNA (LEsiRNA) nanoparticles, were administered to tumor-bearing mice, leading to signal enhancement in MR images of xenografts. Delivery to tumor was also confirmed by visualization of the nanoparticle rhodamine label with fluorescence microscopy and by reductions in survivin protein expression detected using western blot analysis. Furthermore, survivin LEsiRNA

nanoparticles retarded tumor growth relative to nontargeted control siRNA nanoparticles, confirming that L^EsiRNA nanoparticles are effective theranostic agents. These numerous studies provide strong evidence of the versatility of lipid-based strategies for siRNA delivery, particularly in the setting of cancer.

1.4 Peptide- and Polymer-Based Delivery

One of the most diverse and flexible approaches for siRNA delivery involves the use of peptide, protein, or polymeric carriers (Puebla, Essegir et al. 2003; Simeoni, Morris et al. 2003; Kumar, Wu et al. 2007; Peer, Zhu et al. 2007). As with lipid-based methods, siRNA cargoes become incorporated into the delivery vehicle, often through electrostatic interactions, where they are protected from degradation. Polymer-based delivery similarly allows for siRNA escape from endosomal compartments once internalized, presumably through the promotion of lysosomal rupture, or the proton sponge effect (Boussif, Lezoualc'h et al. 1995). Also, polymer-based probes can be interrogated using a variety of imaging modalities due to the ease with which they are functionalized.

One of the first protein siRNA carriers investigated with imaging was atelocollagen, a pepsin-treated form of collagen protein (Minakuchi, Takeshita et al. 2004; Takeshita, Minakuchi et al. 2005). Atelocollagen complexes with siRNA molecules to form 100-300 nm nanoparticles. Nanoparticles were tested in vivo with bioluminescence imaging in a luciferase xenograft tumor model, where they were found to enhance luciferase silencing relative to cationic liposome-mediated delivery and to inhibit tumor growth (Minakuchi, Takeshita et al. 2004). Atelocollagen siRNA complexes have also been evaluated in a bone metastasis model with optical imaging

(Takeshita, Minakuchi et al. 2005). Their therapeutic potential was confirmed by significant gene silencing of endogenous genes in metastatic lesions accompanied by tumor regression.

Several synthetic cationic polymers have been used as efficient transfection agents for siRNA and can easily be modified to facilitate imaging. Polyethylenimine (PEI), one of the best characterized polycations, was complexed with siRNA that had been radiolabeled with indium through a DTPA chelate (Merkel, Librizzi et al. 2009). The siRNA-PEI polyplexes were monitored with SPECT imaging to investigate their biodistribution and pharmacokinetics relative to free, radiolabeled siRNAs. In another study, pH-sensitive siRNA carriers composed of polycations were designed to enhance siRNA escape from acidified endosomal compartments following endocytosis (Ofek, Fischer et al. 2010). Cationic polyplexes consisted of a dendritic core and polyglycerolamine shell that formed complexes with luciferase siRNA. The polyplexes displayed low toxicity and efficient *in vivo* silencing in a mouse tumor model as confirmed by bioluminescence imaging.

Triblock copolymer PDMAEMA was selected as the basis of a group of micelle siRNA carriers (Gary, Lee et al. 2011). PDMAEMA complexed with siRNA, with multiple siRNA molecules adsorbing to the surface of micelles to form micelleplexes. *In vitro* testing revealed a small but significant effect of siRNA carriers on mRNA expression. Further modification of micelles with folate was shown to improve uptake by cancer cells, though this improved uptake was not accompanied by a significant increase in silencing relative to unmodified micelles. PET/CT imaging of tumor-bearing mice following systemic administration of I^{124} radiolabeled micelleplexes demonstrated

their accumulation and retention in tumor tissue. Another group of polymeric micelles were recently investigated as vehicles for co-delivery of the chemotherapeutic agent doxorubicin (DOX) and siRNA (Xiong and Lavasanifar 2011). The target of siRNA was drug transporter protein, p-glycoprotein, selected to improve the efficacy of DOX. Polymeric micelles composed of poly(ethylene oxide) (PEO) and poly(ϵ -caprolactone) (PCL) copolymers (PEO-b-PCL) were attached to targeting moieties RGD and TAT to form shell-functionalized micelles following assembly. RGD was selected for cancer targeting through its affinity to $\alpha v \beta 3$ integrins while the cell-penetrating peptide TAT was selected to promote cellular internalization. Therapeutics were localized to the micelle core when copolymers conjugated to DOX or complexed with siRNA were added to the micellar formulations. Spermine was incorporated into the micelles to promote nanocarrier release from endosomes. In addition, the carrier and its component siRNA were differentially tagged with near infrared dyes for imaging. RGD/TAT functionalized nanocarriers showed enhanced cellular uptake relative to controls, and following internalization, a pH-dependent release of micelle contents from endosomes was evident. In formulations where siRNA and DOX were co-delivered, DOX localized to the nucleus, leading to sensitization of multi-drug resistant cancer cells to DOX. Preliminary in vivo studies were then performed showing accumulation of nanocarriers in $\alpha v \beta 3$ -positive tumors following systemic administration.

Polymer-based delivery has also been used to create imaging probes that can be detected by MRI. Imaging of the temporal and spatial distribution of siRNA was used to direct and refine therapy in a study investigating siRNA/prodrug enzyme conjugates (Li, Penet et al. 2010). Prodrug enzyme therapy for cancer refers to the process in which an

inactive drug becomes converted to a cytotoxic one by an enzyme present in a tumor. The prodrug enzyme, bacterial cytosine deaminase (bCD), was delivered to tumors intravenously as a component of a fluorescently-labeled PEG/PEI siRNA conjugate that also contained a multimodal image reporter platform. The latter consisted of Cy5.5-labeled Gd^{3+} -DOTA for multimodal imaging. After injection of the nanoplex into tumor-bearing mice, the biodistributions of its components were acquired by in vivo optical imaging. Proenzyme concentration was monitored over time to identify the point at which concentration in normal tissues was negligible relative to the levels in the tumor, corresponding to the time of optimal prodrug administration. The presence of nanoplexes in the tumor was also evident as MR signal enhancement in MR images. The conversion of the prodrug, 5-fluorocytosine, to cytotoxic 5-fluorouracil by bCD in the tumor was confirmed by noninvasive ^{19}F MRS, while siRNA-mediated silencing of antitumoral target, Chk- α , was monitored by 1H MR spectroscopic imaging. Dual treatment of tumors with bCD and siRNA led to a significant delay in tumor growth and increases in necrosis without damage to nonmalignant tissues.

One of the most successful polymer-based delivery modules for siRNAs is cyclodextrin-containing polycations, a group of polymeric, cyclic oligosaccharides that self-assemble with siRNA molecules to form a stable delivery vehicle (Hu-Lieskovan, Heidel et al. 2005; Bartlett and Davis 2006). In one study, cyclodextrin-containing polycations were modified with targeting ligand, transferrin, to increase their affinity for cancer cells that express the transferrin receptor (Hu-Lieskovan, Heidel et al. 2005). The polycations were tested in a murine metastatic cancer model that expressed firefly luciferase. In vivo, whole-body imaging of bioluminescence confirmed delivery of

siRNA targeting luciferase to tumors. In another study, cyclodextrin-containing polycation nanoparticles were loaded with luciferase-specific siRNA that had been radiolabeled with ^{64}Cu -DOTA to form multimodality imaging probes (Bartlett, Su et al. 2007). The biodistribution of nanoparticles was monitored by micro-PET/CT, while siRNA knockdown was simultaneously evaluated by bioluminescence imaging. Direct imaging of siRNA silencing proved crucial, since it provided a way to distinguish between nanoparticles that had passively accumulated in the tumor due to the enhanced permeability and retention effect and those that had been internalized by cancer cells and were bioactive. Consequently, the improved functionality of nanoparticles modified with targeting ligand transferrin relative to nontargeting nanoparticles was confirmed with this method. These studies have paved the way for the first clinical trial to use a targeted, systemically-administered siRNA formulation, in which cyclodextrin-based siRNA carriers are being tested against solid tumors in humans (Davis, Zuckerman et al. 2010).

1.5 Nanoparticle-Based Delivery

Magnetic nanoparticles were the first siRNA delivery modules designed for in vivo visualization by magnetic resonance imaging (Medarova, Pham et al. 2007). Superparamagnetic iron oxide nanoparticles are contrast agents that decrease T2 relaxation of surrounding tissues and lead to corresponding negative contrast, or image darkening, in magnetic resonance images. Dextran-coated magnetic nanoparticles (MN) were modified with three distinct functional groups that included near-infrared fluorochrome Cy5.5 (NIRF) for optical imaging, siRNA molecules targeting GFP (siGFP), and a membrane translocation peptide (MPAP) to promote cellular internalization. Mice bearing bilateral 9L-GFP and red fluorescent protein (9L-RFP)

tumors were used to evaluate the efficacy of these MN-NIRF-siGFP probes after systemic administration. Probe accumulation in cancer cells was reflected by signal loss in MR images and distinct NIRF signal in optical images at the site of the tumors (Figure 1.1). Furthermore, probe siRNA led to significant and specific reduction in fluorescence of 9L-GFP tumors, with no effect on 9L-RFP cells (Figure 1.2). The therapeutic potential of probes was tested by designing nanoparticles bearing siRNA targeting the Birc5, a gene that encodes the protein survivin. Survivin is expressed in most tumor cells and has antiapoptotic functions. MN-NIRF-siSurvivin probes were tested in mice bearing human colorectal carcinoma tumors and were detected using MRI and optical imaging. MN-NIRF-siSurvivin probe accumulation was associated with decreased survivin expression and increased apoptosis and necrosis in tumors relative to those treated with scrambled control siRNA probes. These effects were obtained without any detectable interferon or inflammatory response. Further implementation of this approach involved adding tumor targeting functional groups to nanoparticles to reduce non-specific uptake (Kumar, Yigit et al. 2010). Probes were conjugated with EPPT peptide, the target for tumor-specific antigen uMUC-1, siRNA directed against survivin, and Cy5.5 dye. MN-NIRF-siSurvivin nanoparticles were tested in mice bearing human breast adenocarcinoma tumors. Tumoral uptake of probes was demonstrated by MRI (Figure 1.3a) and optical imaging and confirmed with follow-up fluorescent microscopy of excised tumor sections. Treatment with experimental probes induced significant tumor apoptosis and necrosis relative to control siRNA probes, as well as a two-fold reduction in tumor growth (Figure 1.3b-c).

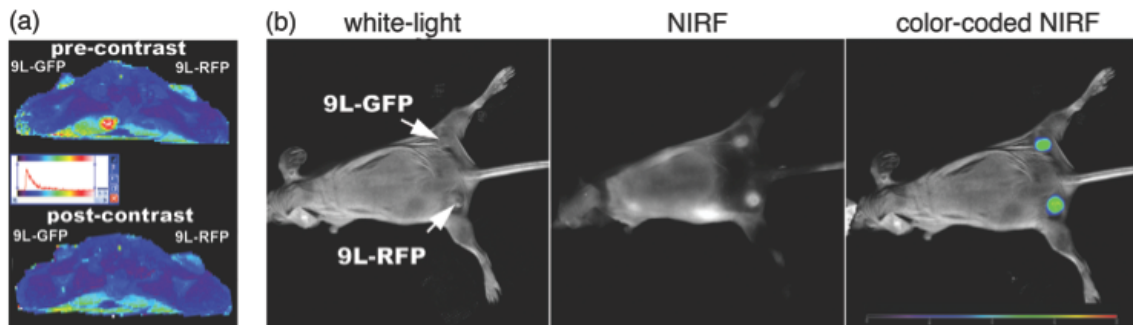


Figure 1.1. Multimodality imaging of NIR-labeled iron oxide nanoparticle (MN-NIRF-siGFP) delivery to tumors. Accumulation of MN-NIRF-siGFP in 9L-GFP and 9L-RFP bilateral tumors was confirmed by both magnetic resonance and optical imaging. MN-NIRF-siGFP delivery was reflected by decreased T2 relaxation in MR images (a) and by the emergence of high intensity NIR signal in whole body optical images (b) twenty-four hours after probe administration. Reprinted with permission from Macmillan Publishers Ltd.: Medarova et al., *Nature Medicine*, 13, 372-77 (2007).

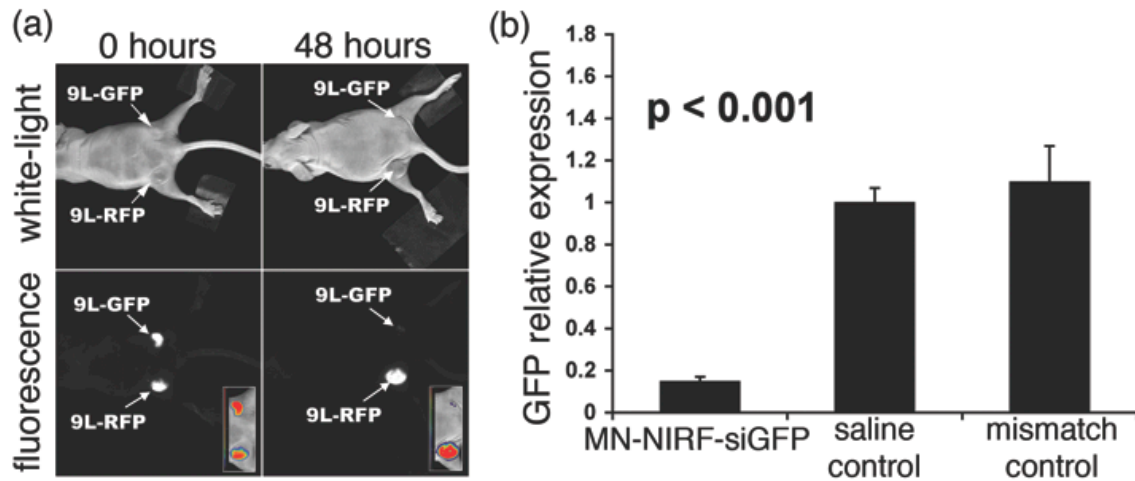


Figure 1.2. Efficacy of siGFP delivered with iron oxide nanoparticles. (a) MN-NIRF-siGFP delivery resulted in reduction of 9L-GFP tumor fluorescence 48 hours after probe administration. No reduction of 9L-RFP fluorescence was observed, indicating that silencing by MN-NIRF-siGFP was gene specific. (b) Suppression of GFP expression by MN-NIRF-siGFP was confirmed by quantitative RT-PCR analysis of RNA extracted from 9L-GFP tumors. Treatment reduced *gfp* mRNA levels by 85% and 97% relative to saline-treated and mismatch scrambled control siRNA probes, respectively ($P < 0.001$). Reprinted with permission from Macmillan Publishers Ltd.: Medarova et al., Nature Medicine, 13, 372-77 (2007).

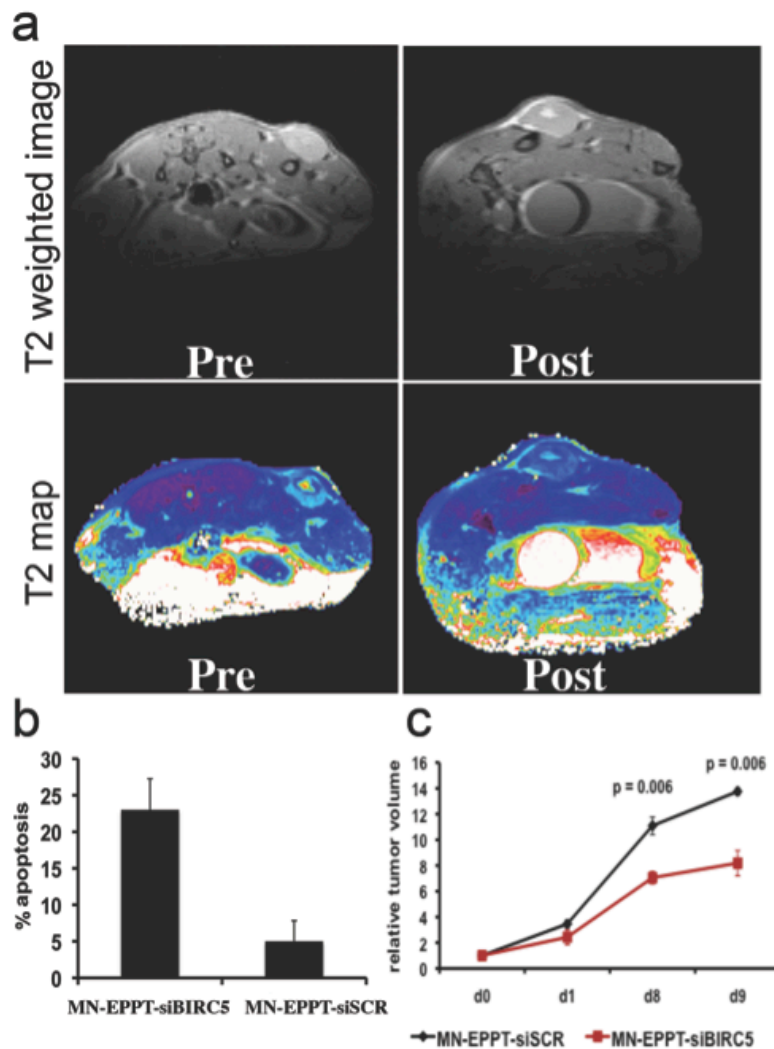


Figure 1.3. Tumor-targeted siRNA delivery with iron oxide nanoparticles (MN-EPPT-siBIRC5). (a) T2 MR images and T2 maps of mice bearing human breast adenocarcinoma tumors showed decreased signal intensity and T2 shortening in tumors following intravenous injection of MN-EPPT-siBIRC5, indicating accumulation of probe. (b) MN-EPPT-siBIRC5 accumulation was associated with a five-fold increase in apoptosis induction relative to scrambled control siRNA (MN-EPPT-siSCR) probes (P=0.003). (c) MN-EPPT-siBIRC5 also led to a 2-fold reduction in tumor growth rate relative to controls eight days after treatment (P < 0.01). Reprinted with permission from AACR: Kumar et al., Cancer Research, 70:7553-7561 (2010).

Magnetic nanoparticle-based modules designated ‘dendriworms’ are another platform investigated for siRNA delivery (Agrawal, Min et al. 2009). Elongated magnetic nanoparticle chains were surface modified with near infrared fluorochromes for imaging, siRNAs for target therapy, and polyamidoamine dendrimer cationic polymers to promote endosomal escape of the dendriworms. Following convection-enhanced diffusion of dendriworms into brain tumors in mice, reduction in the expression of the siRNA target, EGFR, was observed. Though MR imaging was not a component of the study, the iron oxide nanoparticles comprising dendriworms could potentially be evaluated with this modality to extend their versatility. Another group investigated nanocarriers composed of iron oxide nanoparticles that form a stable cluster structure when combined with alkylated PEI and luciferase siRNA. These complexes had high T2 relaxivity in MRI phantom studies, signifying their potential as MRI contrast agents (Liu, Xie et al. 2011). In vivo investigation focused on bioluminescence imaging, where significant siRNA knockdown in luciferase-expressing tumors was observed.

Recently a form of inducible RNAi using siRNA-conjugated hollow gold nanospheres was investigated (Lu, Zhang et al. 2010). When irradiated with near infrared light, gold nanospheres undergo a structural change that causes the release of siRNA molecules from the nanosphere surface in a process termed photothermal transfection. Nanoparticles conjugated to siRNA molecules were further modified with a targeting ligand, folic acid, to give them an affinity for cancer cells. In culture, NIR irradiation led to rupture of endolysosomal membranes, escape from endocytic vesicles to the cytoplasm, release of siRNA from nanospheres, and downregulation of the siRNA target, NF- κ B p65 subunit. Positron emission tomography imaging of in vivo delivery was

enabled by conjugating ^{64}Cu -labeled DOTA-LA chelating ligands to the nanoparticles. Micro-PET/CT imaging revealed accumulation of folate receptor-targeted nanoparticles in subcutaneous tumors and photothermal transfection resulted in significant decreases in p65 expression in tumor tissue. Notably, irradiated tumors that received a combination treatment of targeted siRNA nanospheres and chemotherapeutic irinotecan had enhanced tumor apoptosis and growth reduction relative to non-irradiated targeted nanospheres or irinotecan treatment alone.

Several nanoparticle carrier systems have shown promise in preliminary in vitro studies. Superparamagnetic nanoparticles have been designed with a variety of functional groups to improve stability and promote receptor-mediated uptake for cancer treatment and imaging (Mok, Veiseh et al. 2010; Veiseh, Kievit et al. 2010). Iron oxide nanoparticles functionalized with PEI, siRNA, and tumor-targeting chlorotoxin have been designed for selective enhanced cellular uptake and gene silencing in the low-pH conditions of tumor microenvironments (Mok, Veiseh et al. 2010). Multi-functional hollow manganese oxide nanoparticles have been developed as T1 contrast agents for siRNA delivery to cancer cells (Bae, Lee et al. 2011). Nanoparticles that had been surface modified with PEI, Herceptin for targeting of cancer cells with the HER2 receptor, and siRNA directed against VEGF were internalized by cancer cells. This process was detectable by in vitro T1-weighted MRI and was associated with reduction in VEGF release from human breast adenocarcinoma cancer cells that overexpressed HER2. In addition, PEI-modified large pore hollow silica nanocapsules loaded with siRNA have been shown to efficiently transfect cells and downregulate target protein by 64% (Chen, Chu et al. 2011). Their imaging potential was confirmed when nanocapsules loaded with

iron oxide nanoparticles exhibited reduced T2 relaxation. These different nanoparticle-based approaches to siRNA delivery provide strong evidence that properly modified siRNAs can be monitored in a clinical setting.

1.6 Conclusion

The preceding has been an overview of the imaging methods that have developed in parallel with siRNA delivery systems to promote tissue targeting and gene silencing efficiency. Monitoring delivery provides vital information about the in vivo handling and efficacy of siRNA molecules as they are applied to increasingly complex disease models. As RNAi-based therapeutics progress to clinical trials, image-guided methods can only serve to improve siRNA delivery and patient care.

2. Small Interfering RNA Fluorescent Probes for Ischemic Stroke

Therapy

2.1 Introduction

In the United States, stroke is the fourth leading cause of death in the general population and the main source of long term disability among the elderly (2001; Thom, Haase et al. 2006; National Center for Health 2012). Stroke is a general term that denotes cerebral cell death due to the disruption of the circulation. The most common source of disruption is an intravascular blood clot or embolus that interferes with the delivery of nutrients and oxygen to cells (Rosamond, Folsom et al. 1999). Restricted blood flow, known as ischemia, induces a cascade of pathological cell signaling events, culminating in widespread cell death (Lipton 1999). Within minutes of an ischemic insult, impairment of energy-dependent processes occurs in neurons. ATP-driven ion channels fail to maintain ionic gradients, leading to membrane depolarization and the release of the excitatory neurotransmitter glutamate in large quantities (Martin, Lloyd et al. 1994; Danbolt 2001). Excitotoxic overstimulation of glutamate receptors leads to the spread of ion imbalance and deleterious elevations in intracellular calcium levels (Danbolt 2001). Calcium, in turn, activates degradative enzymes and promotes the production of reactive oxygen species by mitochondria (Choi 1995; Brouns and De Deyn 2009). The resulting enzymatic and oxidative damage to the brain parenchyma contributes to tissue death, or infarction, within minutes to hours of blood stoppage (Doyle, Simon et al. 2008). In addition, oxidative stress to vascular structures causes blood-brain barrier dysfunction and recruitment of inflammatory cells that contribute to tissue damage over a period of days (Doyle, Simon et al. 2008; Brouns and De Deyn 2009).

The main strategy for limiting the severity of ischemic stroke damage is the restoration of blood flow, or reperfusion, to provide resources for the repair of injured cells (1995; Hacke, Donnan et al. 2004). This approach employs recombinant human tissue plasminogen activator (t-PA), a thrombolytic agent that improves neurologic outcome and increases long-term patient survival when administered intravenously within hours of stroke onset (1995). Although reperfusion by t-PA is essential for minimizing damage, it can also aggravate conditions by placing marginally-injured cells into contact with blood while their regulatory abilities are impaired (Hamann, Okada et al. 1995; Hamann, Okada et al. 1996; Wang, Tsirka et al. 1998; Wu, Tamaki et al. 1998). This is particularly critical in the cells surrounding the core of the infarct, collectively known as the ischemic penumbra, which have the potential to progress to apoptosis but can be rescued under certain conditions. Reducing the deterioration of cells in the penumbra has been the goal of numerous studies investigating neuroprotective agents for the treatment of stroke. Pharmaceuticals that inhibit cellular mediators of excitotoxicity (Lyden, Jacoby et al. 2001; Diener, AlKhedr et al. 2002), inflammation (2001), and reactive oxygen species (Shuaib, Lees et al. 2007) or that promote neuroregeneration (Bogousslavsky, Victor et al. 2002) have been investigated clinically. None have led to a successful FDA-approved therapy, partly due to the failure of drugs to reach their therapeutic targets.

2.1.1 RNA Interference and Cell Penetrating Peptide (CPP) Delivery

RNA interference (RNAi) technology is a potentially valuable approach to stroke therapy because it can easily be adapted to target any gene that minimizes cell damage after ischemia, provided that the gene sequence is known. In the past decade, RNAi has

been rapidly integrated into basic biomedical research, emerging as a premier method for regulating gene expression in a variety of model systems. As RNAi-based therapies progress to clinical trials and are applied to increasingly complex human diseases, the need for improved small interference RNA (siRNA) delivery methods and monitoring becomes critical (Castanotto and Rossi 2009). These considerations are particularly relevant in neurological pathologies, in which an intact blood-brain barrier (BBB) may limit direct contact between diseased cells and most systemically administered agents.

One approach for overcoming biological membranes exploits naturally-occurring membrane translocation sequences that are known in the literature as cell penetrating peptides (CPPs), protein transduction domains (PTDs) or Trojan peptides (Derossi, Joliot et al. 1994; Vives, Brodin et al. 1997). CPPs were originally derived from membrane permeable cationic viral protein transduction domains, transcription factors, or cell adhesion proteins and range in size from 10-30 amino acids (Langel 2007). CPPs have been modified to accommodate and promote the intracellular delivery of diverse molecular cargoes, including proteins (Schwarze, Ho et al. 1999), liposomes (Torchilin, Levchenko et al. 2003), and nanoparticles (Lewin, Carlesso et al. 2000). While the precise mechanism of CPP internalization remains controversial, most studies suggest that peptide entry is mediated by energy-dependent endocytic pathways, though there is evidence that direct translocation across membranes occurs, particularly by CPPs with an amphipathic nature. A summary of the best-characterized CPPs is presented in Table 2.1.

Recently it was demonstrated that intravenously injected siRNA, when used in conjunction with a peptide sequence from rabies virus glycoprotein, was delivered to the

Table 2.1. Cell Penetrating Peptides.

Peptide/ Amino acid Sequence	Source	Internalization Mechanism	Cargo Molecules Delivered
HIV-Tat/ GRKKRRQRRRPPQ	Peptides 48-60 of the Tat protein of human immunodeficiency virus type 1 (HIV-1)(Vives, Brodin et al. 1997).	Clathrin-dependent and caveolin-independent endocytosis (Richard, Melikov et al. 2005), lipid raft-dependent endocytosis (Wadia, Stan et al. 2004), temperature-dependent caveolar endocytosis (Fittipaldi, Ferrari et al. 2003).	<ul style="list-style-type: none"> • Fusion peptides (Schwarze, Ho et al. 1999). • Liposomes (Torchilin, Rammohan et al. 2001). • Iron nanoparticles (Lewin, Carlesso et al. 2000). • Oligonucleotides (Astrib-Fisher, Sergueev et al. 2002).
Penetratin/ RQIKIWFQNRRMKWKK	Peptides 43-58 of the Antennapedia (Antp) homeodomain third helix (Derossi, Joliot et al. 1994).	Direct translocation (Derossi, Chassaing et al. 1998; Letoha, Gaal et al. 2003), adsorptive-mediated endocytosis with endosomal acidification (Fischer, Kohler et al. 2004).	<ul style="list-style-type: none"> • Oligonucleotides (Troy, Derossi et al. 1996). • Peptides (Perez, Lledo et al. 1994; Theodore, Derossi et al. 1995; Troy, Stefanis et al. 1996).
Oligoarginine/ RRR...R [6-15 R's]	Designed (Futaki, Suzuki et al. 2001).	Endocytosis (Fuchs and Raines 2004), macropinocytosis (Nakase, Niwa et al. 2004), energy-independent entry (Thoren, Persson et al. 2003).	<ul style="list-style-type: none"> • Nucleic acids and peptides (Kim, Christensen et al. 2006; Kumar, Wu et al. 2007).
Transportan/ GWTLNSAGYLLGKIN LKALAALAKKIL	Chimeric protein formed by the fusion of the neuropeptide galanin and wasp venom toxin mastoparan (Pooga, Hallbrink et al. 1998).	Clathrin dependent and independent endocytosis (Saalik, Elmquist et al. 2004; Padari, Saalik et al. 2005).	<ul style="list-style-type: none"> • Gold nanoparticles (Saalik, Elmquist et al. 2004).
pVEC/ LLIILRRRIRKQAHAAHS K	Peptides 615-632 of murine vascular endothelial cadherin (Elmquist, Lindgren et al. 2001).	Clathrin-dependent endocytosis (Elmquist, Hansen et al. 2006).	<ul style="list-style-type: none"> • Peptide nucleic acids (Elmquist, Lindgren et al. 2001). • Streptavidin-FITC (Elmquist, Lindgren et al. 2001).

Table 2.1. (Continued).

Pep-1/ KETWWETWWTEWSQ PKKKRKV	Designed, chimeric CPP with tyrosine-rich hydrophobic region and a nuclear localization sequence derived from simian virus 40 large T antigen (Morris, Depollier et al. 2001).	Direct membrane translocation (Deshayes, Morris et al. 2005; Henriques, Quintas et al. 2007).	<ul style="list-style-type: none"> • Peptides (Morris, Depollier et al. 2001). • Proteins [e.g., β-galactosidase] (Henriques, Costa et al. 2005).
MPG/ GALFLGFLGAAGSTM GAWSQPKSKRKV	N-terminal residues derived from HIV gp41 transmembrane protein (Morris, Vidal et al. 1997).	Direct translocation (Morris, Vidal et al. 1997; Simeoni, Morris et al. 2003; Deshayes, Morris et al. 2005).	<ul style="list-style-type: none"> • DNA (Morris, Vidal et al. 1997).
VP22/ DAATATGRSAASRPT ERPRAPARSASRPRRP VD	Herpes simplex virus type 1 (HSV-1) tegument protein (Elliott and O'Hare 1997).	Macropinocytosis (Normand, van Leeuwen et al. 2001).	<ul style="list-style-type: none"> • Fusion proteins (e.g., p53 (Phelan, Elliott et al. 1998) and thymidine kinase (Dilber, Phelan et al. 1999)). • Oligonucleotides (Normand, van Leeuwen et al. 2001).
KALA/ WEAKLAKALAKALAK HLAKALAKALKACEA	Designed (Wyman, Nicol et al. 1997), amphipathic molecule with a hydrophobic leucine-rich region for DNA binding (Mascotti and Lohman 1993) and a hydrophilic lysine-rich region for cell membrane penetration (Subbarao, Parente et al. 1987)	Pore formation (Wyman, Nicol et al. 1997)	<ul style="list-style-type: none"> • Oligonucleotides and plasmid DNA (Wyman, Nicol et al. 1997).
Model Amphipathic Peptide (MAP)/ KLALKLALKALKAAL KLA	Designed (Oehlke, Scheller et al. 1998)	Endocytotic and non-endocytotic entry (Oehlke, Scheller et al. 1998).	<ul style="list-style-type: none"> • Peptide nucleic acids (Oehlke, Wallukat et al. 2004).

Table 2.1. (Continued).

VPR/ DTWPGVEALIRILQQL LFIHFRIGCQH	From the 96 amino acid protein of human immunodeficiency virus 1 (HIV-1) (Taguchi, Shimura et al. 2004).	Clathryn-mediated endocytosis (Coeytaux, Coulaud et al. 2003). Direct translocation via membrane permeabilization (Coeytaux, Coulaud et al. 2003).	<ul style="list-style-type: none">• Protein (e.g., GFP (Taguchi, Shimura et al. 2004) and β-galactosidase (Taguchi, Shimura et al. 2004)).• Plasmid DNA (Coeytaux, Coulaud et al. 2003).
------------------------------------------------	----------------------------------------------------------------------------------------------------------	-----------------------------------------------------------------------------------------------------------------------------------------------------------	----------------------------------------------------------------------------------------------------------------------------------------------------------------------------------------------------------------------------------

brain and retained its gene silencing capabilities (Kumar, Wu et al. 2007; Pulford, Reim et al. 2010). In our laboratory, we have investigated a cationic arginine-based CPP modified with myristic acid that has a high affinity for lipid bilayer membranes, which promotes enhanced entry into cells relative to well-established Tat and oligoarginine CPPs (Pham, Kircher et al. 2004). Hydrophobic moieties in CPPs, like myristic acid, are important because they improve CPP escape from endosomal vesicles to the cytoplasm (Takayama, Hirose et al. 2012). We have used our myristoylated poly-arginine peptide, or MPAP, to promote cellular delivery of nanoparticle imaging agents to solid tumors after intravenous injection (Medarova, Pham et al. 2007; Kumar, Medarova et al. 2010). Furthermore, MPAP has demonstrated BBB permeability in vivo, where it was shown to localize to neurons, astrocytes and endothelial cells after intravascular administration (Pham, Zhao et al. 2005). These properties make MPAP ideally suited for use with siRNA to form a dual optical imaging and therapeutic probe for neurological applications, provided that a method of complexation is developed that does not inhibit the bioactivity of siRNA molecules.

2.1.2 MPAP-siRNA Stroke Therapeutics

This chapter details our investigation of fluorescently labeled MPAP, comprising a poly-arginine peptide modified with a 14-carbon myristic acid moiety, for siRNA delivery. We describe the generation and testing of an MPAP and siRNA (MPAP-siRNA) imaging probe complex for the treatment of ischemic stroke. We hypothesized that if siRNA directed against genes implicated in stroke pathology were effectively delivered to primary neurons and astrocytes to intercede in this process, neuroprotection could be elicited. With this in mind, we developed dual MPAP-siRNA optical imaging

probes directed against c-Src (Src), a protein tyrosine kinase with activity that becomes upregulated after stroke and is associated with increased tissue damage in cerebral ischemia models (Korematsu, Goto et al. 1994; Paul, Zhang et al. 2001). Src is involved in numerous cellular roles ranging from proliferation and adhesion to cell survival (Collett, Brugge et al. 1978; Oppermann, Levinson et al. 1979; Thomas and Brugge 1997). In vitro hypoxia studies have demonstrated an increase in Src activation within minutes of hypoxic stimulus that is at least partially mediated by reactive oxygen species (Sato, Sato et al. 2005). Src expression increases in ischemic stroke soon after the induction of reperfusion (Korematsu, Goto et al. 1994). *Src* knockout mice are protected from ischemic damage, with an approximately 50% decrease in infarct size relative to wild-type controls (Paul, Zhang et al. 2001). Protection from ischemia extends to wild-type mice when treated with a Src-inhibitor within six hours of stroke induction, probably through reduction of VEGF-induced cerebral edema and inflammation. Src may also contribute to excitotoxicity-related stroke damage through phosphorylation of proteins associated with NMDA (*N*-methyl-D-aspartate) receptors and increases in pathological calcium currents (Liu, Zhang et al. 2001; Liu, Hou et al. 2003; Du, Gao et al. 2009). The conclusions drawn from these studies regarding the role of Src in stroke pathology and the effectiveness of Src-inhibitors after stroke induction made Src a strong potential target for stroke therapy in the proposed work.

Src-directed probes were assembled by utilizing the natural affinity of cationic peptides for oligonucleotides, a process that was optimized to ensure maximum siRNA incorporation. MPAP complexes with Src siRNA (MPAP-Src) were tested for stability. Their internalization in primary central nervous system cells and an endothelial cell line

was monitored by flow cytometry and confocal microscopy. The probes were also evaluated for cytotoxicity and siRNA silencing efficiency. In vitro studies confirmed that MPAP-Src complexes become internalized by cells and cause statistically-significant reductions in endogenous *Src* levels without significantly affecting cell viability. Next we transitioned to testing MPAP-Src complexes in experimental mouse models of stroke. Intravenous administration of MPAP-Src before or after transient middle cerebral artery occlusion resulted in marked accumulations of probe that were evident by *ex vivo* optical imaging. However, neither treatment paradigm mitigated stroke damage to a statistically significant degree. Direct intracerebral injection of probes resulted in significant reductions in *Src* mRNA expression, demonstrating that MPAP-Src can modulate gene expression in the brain. Despite the observation that *Src* reduction was not neuroprotective, our results indicate that MPAP is a viable platform for siRNA delivery that may prove effective against alternative stroke targets.

2.2 Experimental Procedures

2.2.1 MPAP Probe Synthesis

Myristoylated polyarginine peptide (MPAP), C14- β Ala-(Arg)₇-Cys(SH)-NH₂, was synthesized and purified as described previously (Pham, Zhao et al. 2005) and conjugated to Cy5.5 fluorescent dye (Amersham, Piscataway, NJ) to form MPAP-Cy5.5. Conjugation of the fluorescent dye, Cy5.5 mono maleimide (0.87 mmol), to purified MPAP (1.5 mmol) was carried out in 1:1 acetonitrile/50 mM NaOAc (pH 7.4) buffer at room temperature overnight with constant agitation. The MPAP-Cy5.5 product was purified by reversed-phase HPLC. The mass of MPAP-Cy5.5 determined by MALDI mass spectroscopy was 2536.42 (calculated 2537.04). Scrambled siRNA and siRNA

directed against mouse Src, both labeled on the 5' sense strand with fluorescent tag Dy547 (absorbance/emission max: 548/562nm), were designed and synthesized by Dharmacon (Chicago, IL). To promote probe complex formation, MPAP-Cy5.5 was dissolved in water, combined with siRNA-Dy547 solution, and mixed through gentle aspiration. The resulting probe mixture was incubated for 20 minutes at room temperature to induce complete complexation of the two components.

2.2.2 Gel Mobility Shift Assay and Zeta Potential Characterization

To optimize stoichiometry of MPAP-Cy5.5 and siRNA complexes, we performed polyacrylamide gel electrophoresis. For this, various dilutions of MPAP-Cy5.5 solution were added to siRNA (20 pmol) to obtain 1:10, 1:5, 1:2.5, 1:1, 2.5:1, 5:1 and 10:1 siRNA-to-peptide molar ratios. Samples were incubated for 20 minutes at room temperature to allow complexation, and loaded onto 20% polyacrylamide-TBE gels (Novex, Invitrogen, Carlsbad, CA) along with reference siRNA solutions (20, 10, 5, and 1 pmol). The gel was subjected to electrophoresis at 200 V for 30 minutes. In each sample solution, free siRNA that had failed to associate with MPAP traveled through the gel, while complexes remained stationary in the gel's loading well. The gel was stained with ethidium bromide and visualized by UV-illumination. The amount of free siRNA in each sample was quantified using ImageJ software (NIH) to analyze the density of each siRNA band relative to reference siRNA solutions. The molar ratio for which complete incorporation of siRNA was demonstrated (i.e., 1:5 siRNA:MPAP ratio) was selected for further study. The zeta potentials of MPAP-Src complexes were measured with a Malvern Zetasizer Nano Series ZS instrument.

2.2.3 Serum Stability

Solutions of free siRNA or MPAP-Cy5.5 complexed with siRNA (MPAP-Src) were incubated in mouse serum to evaluate the protective effect of MPAP-Cy5.5 against nuclease digestion of siRNA. MPAP-Cy5.5 and c-Src siRNA were combined at a 1:5 siRNA-to-peptide molar ratio and incubated for 20 minutes at room temperature. The complexes were then incubated at 37°C in 75% fresh mouse serum. Aliquots were removed at 0, 0.5, 1, 2, 4, and 8 hour time points, placed in 1 mg/ml proteinase K (Invitrogen, Carlsbad, CA) to remove any associated protein, and frozen in preparation for subsequent gel electrophoresis. MPAP-Src samples were subjected to gel electrophoresis in 20% polyacrylamide-TBE gels alongside samples of free siRNA that had been digested in serum. The gels were visualized by SYBR Gold (Molecular Probes, Invitrogen, Eugene OR) staining. For each sample, the amount of siRNA spared from nuclease digestion was quantified using ImageJ software (NIH) and normalized by undigested free siRNA or undigested siRNA complexed with MPAP-Cy5.5 to obtain the percentage of intact siRNA over time. Results are a compilation of four separate experiments.

2.2.4 Cell Culture and MPAP-Mediated siRNA Delivery

Primary Mouse Cortical Neurons and Astrocytes

Cortical neuron cultures were generated from embryonic day 18 C57BL/6 mouse fetuses following the procedures outlined in (1998) with modifications. After brain removal, cortices were dissected and separated from meningeal tissues. Cortices were finely chopped, washed with HBSS, and suspended in Papain enzyme solution (Worthington Biochemical Corporation, Lakewood, NJ). Following 15 minutes of

incubation in enzyme solution at 37°C, cortices were washed with Neurobasal medium (Gibco, Invitrogen, Grand Island, NY) and triturated through a small-bore pipet tip to form a single cell suspension. The cells were passed through a 70-micron cell strainer, pelleted by centrifugation, and resuspended in Neurobasal medium containing 10% fetal bovine serum (FBS), 100 U/mL penicillin and 100 mg/mL streptomycin (pen-strep). Neurons were plated in 12-well plates coated with poly-D-lysine and laminin (Sigma, St. Louis, MO) at a density of 1×10^5 cells per well and incubated at 37°C for 1 hour. Media was replaced with Neurobasal medium containing Glutamax and B-27 supplements (Gibco, Invitrogen, Grand Island, NY) and pen-strep. Neurons intended for confocal microscopy were plated on glass coverslips coated with poly-D-lysine and laminin and maintained in 12-well plates. The cells were treated with mitotic inhibitor cytosine-b-D-arabino-furanoside (Sigma, St. Louis, MO) 24 and 48 hours after initial plating to inhibit glial cell growth. Experiments were initiated 5-7 days after plating.

Cell culture of cortical astrocytes was performed using a slight modification of the procedure for neurons. Cortices were dissected from C57BL/6 mouse pups, postnatal day 1-2. Following enzymatic digestion, cells were washed with DMEM containing 10% FBS and pen-strep, triturated, filtered, pelleted, and resuspended in DMEM media. Cells were grown in culture flasks with media changes three times per week. When confluent, the cells were placed on an orbital shaker at 250 rpm for four hours to promote removal of non-astrocytes. Media was removed and astrocytes were dissociated with 0.05% Trypsin/0.53 mM EDTA and subcultured in DMEM/FBS solution in 12-well plates at 1×10^5 cells per well. Cells intended for confocal microscopy were plated on glass coverslips contained in 12-well plates. All experiments were performed one day after

plating. Media was changed to serum-free DMEM containing pen-strep prior to experiments.

bEnd.3 Cell Culture

An endothelial cell line, bEnd.3, was obtained from American Type Culture Collection (Manassas, VA). Cells were grown in DMEM containing 10% FBS and pen-strep. Cells were plated in 12-well plates at a density of 5×10^4 cells per well for all experiments except for confocal microscopy, for which cells were plated on glass coverslips. Experiments were performed one day after plating on cells in serum-free DMEM containing pen-strep.

In vitro MPAP-siRNA Delivery

Cy5.5-labeled MPAP (500 pmoles, 20 pmol/ μ l) was added to 100 pmoles (200 pmol/ μ l) of Dy547-labeled scrambled or c-Src specific siRNA (Dharmacon, Chicago, IL). The solution was incubated for 20 minutes at room temperature and added to primary astrocytes, primary neurons, or bEnd.3 cells plated in serum-free media in 12-well plates. Total siRNA and MPAP concentrations during incubation were 100 nM and 500 nM, respectively. Cells were incubated with the probe for 48 hours, unless otherwise stated.

2.2.5 Cytotoxicity Assays

Cells were obtained according to the procedures described above, plated in 96-well plates and grown to 80% confluency. MPAP-Src was added to the cells in concentrations scaled down to accommodate 96-well conditions. Experiments were performed at probe concentrations of 100 nM siRNA and 500 nM MPAP, with approximately 8 pmol:40 pmol siRNA:MPAP added per well. Following 48 hours of

incubation with MPAP-Src or media only, cells were processed for 3-(4,5-Dimethyl-2-thiazolyl)-2,5-diphenyl-2H-tetrazolium bromide (MTT) or caspase-3 analysis. For MTT assays, cells were incubated in 0.5 mg/ml MTT (Sigma, St. Louis, MO) for 4 hours, after which the solution was replaced with dimethyl sulfoxide (DMSO). The absorbance values of the resulting solutions were acquired by microplate reader at 570 nm with 630 nm used as reference. Cells incubated in 1 µg/ml staurosporine for 24 hours were used as positive controls. Caspase-3 assays were performed using the CASP-3-C caspase-3 assay kit according to the manufacturer's protocol (Sigma, St. Louis, MO). All cytotoxicity measurements were performed in triplicate and normalized by total protein content (BCA (bicinchoninic acid) assay, Pierce, Rockford, IL). Statistical analysis of differences between treatment groups was performed using Student's t-testing, in which a value of $p < 0.05$ was considered statistically significant.

2.2.6 Fluorescence-Activated Cell Sorting (FACS)

The extent of probe internalization by astrocytes, neurons and bEnd.3 cells was investigated using FACS analysis. Cells incubated with MPAP-Src or MPAP associated with scrambled control siRNA (MPAP-Ctrl, designed by Dharmacon) for 24 hours were washed with HBSS, dissociated with trypsin, fixed with 2% paraformaldehyde and stored at 4°C until analysis. Untreated cells served as a negative control. Measurements of Dy547-labeled siRNA (FL-2) and Cy5.5-labeled MPAP (FL-4) fluorescence were performed using a FACS Caliber flow cytometer (Becton Dickinson Biosciences, San Jose, CA).

2.2.7 Fluorescence Confocal Microscopy of MPAP-siRNA Delivery

Confocal microscopy was used to visualize the intracellular distribution of MPAP-Src complexes. Following 24 hour incubation with probe at 37°C, cells were washed with PBS and fixed in 4% paraformaldehyde. Neurons and astrocytes were permeabilized in 0.1% Triton-X, blocked with bovine serum albumin, and incubated with rabbit antibody to mouse beta III tubulin specific for neurons or rabbit antibody to mouse glial fibrillary acidic protein specific for astrocytes (Abcam, Cambridge, MA). This was followed by incubation with goat anti-rabbit secondary antibody labeled with Alexa Fluor 488 (Molecular Probes, Invitrogen, Eugene OR). Endothelial bEnd.3 cells were stained with a CD31 antibody that was labeled with a FITC conjugate (Invitrogen, Camarillo, CA). The precise intracellular localization of probes was investigated using LysoSensor Green DND-153 (Molecular Probes, Invitrogen, Eugene, OR). In preparation for live-cell confocal microscopy, cells were incubated in 62 nM LysoSensor Green DND-153 in DMEM for 30 minutes. Cells were washed with HBSS and imaged immediately. Imaging was performed with an Axiovert 200M inverted microscope (Carl Zeiss Inc., Oberkochen, Germany) that included the Zeiss LSM Pascal Vario RGB Laser Module (Arg 458/488/514 nm, HeNe 543 nm, HeNe 633 nm). Cells were imaged in the Cy5.5 channel to detect MPAP, the Cy3 channel to detect siRNA, and the FITC channel to detect LysoSensor Green and cell-specific stains.

2.2.8 Real-Time Quantitative RT-PCR

For in vitro studies, astrocytes, neurons and bEnd.3 cells were incubated for 24 or 48 hours with MPAP-Src (n=7) or MPAP-Ctrl (n=7) probes. Total RNA was purified from cells using the RNeasy Mini kit (Qiagen, Valencia, CA). For in vivo studies, fresh

brain tissue was disrupted on ice in lysis buffer (RP1 buffer, Clontech) and β -mercaptoethanol using a rotor-stator homogenizer. Total RNA was isolated from the lysate using the Nucleospin Total RNA and Protein Isolation kit (Clontech).

The RNA was subjected to real-time quantitative RT-PCR (TaqMan) to determine relative levels of *c-src* mRNA. The sequences of primers and probe used for amplification are as listed: forward primer, 5'-AGCGGCGGTTTCTACATCAC-3' (*c-src* isoform 1 nucleotides 1033-1052); reverse primer, 5'-GTAAGCCACGAGCTGCTGC-3' (nucleotides 1077-1095); TaqMan probe, 5'-TCCCGCACCCAGTTCAACAGCC-3' (nucleotides 1054-1075). Statistical analysis of RT-PCR results was performed using Student's t-tests in which a value of $p < 0.05$ was considered statistically significant.

2.2.9 Middle Cerebral Artery Occlusion (MCAo) Surgery

All animal experiments were approved by the Subcommittee on Research Animal Care at Massachusetts General Hospital and carried out according to institutional guidelines. Adult male C57BL/6N mice of 10-12 weeks of age, weighing between 25-31 grams, were purchased from Charles River Laboratories. Animals were housed in a facility with ambient temperature and humidity control and 12-hour light/dark cycles. Transient cerebral ischemia through middle cerebral artery occlusion (MCAo) was induced using a modification of the procedure developed for rats by Longa et al. (Longa, Weinstein et al. 1989) and later adapted to mice (Belayev, Busto et al. 1999). General anesthesia was induced with inhalational anesthetic isoflurane (Forane, Baxter) applied at a dose of 2-2.5% in a mixture of 30% oxygen and 70% nitrous oxide using a precision vaporizer (Ohmeda Isotec). Surgical depth of anesthesia was confirmed by reduction in

respiratory rate and the loss of pedal withdrawal reflexes (Flecknell 1996). During the surgical procedure, anesthesia was applied via facemask with a vacuum scavenging system and maintained at 1.0-1.5% isoflurane in oxygen/nitrous oxide gas at a total flow rate of 2.0 L/min. Mice were placed on a cleaned and sanitized surgical table, equipped with a heat pad with adjustable temperature control for maintenance of body temperature within normal physiological limits ($37\pm 0.5^{\circ}\text{C}$). Temperature was monitored with a T-type thermocouple temperature probe (AD Instruments) that was advanced 15 mm into the rectum and kept in place through the entirety of the experiment. Surgeries were carried out using modified aseptic techniques with protective clothing, sterile supplies, sterile surgical field, and disinfection of animal skin surfaces with the iodophor Betadine. All surgical instruments were decontaminated using the Germinator dry bead sterilizer (Roboz) prior to use. For analgesia, 2% lidocaine hydrochloride (10 ul, Hospira), was injected locally at the incision site pre-operatively, while postoperative buprenorphine (0.05 mg/kg subcutaneous, Bedford Labs) was administered every 12 hours or as needed. Fluid supplementation during surgery was performed through subcutaneous injections of 0.9% NaCl (Flecknell 1993).

In preparation for the MCAo procedure, a laser doppler fine needle probe unit (AD Instruments) was implanted over the middle cerebral artery brain territory. For this, the anesthetized mouse was placed in prone position. A 5-mm midline incision was made through the scalp to reveal bregma, the anatomical marker of the skull where the sagittal and coronal sutures meet (Figure 2.1a). To keep the doppler probe stationary during the experiment, a doppler probe holder was fashioned from PE-50 polyethylene catheter tubing modified on one end with a rubberband (Figure 2.1b). The holder was

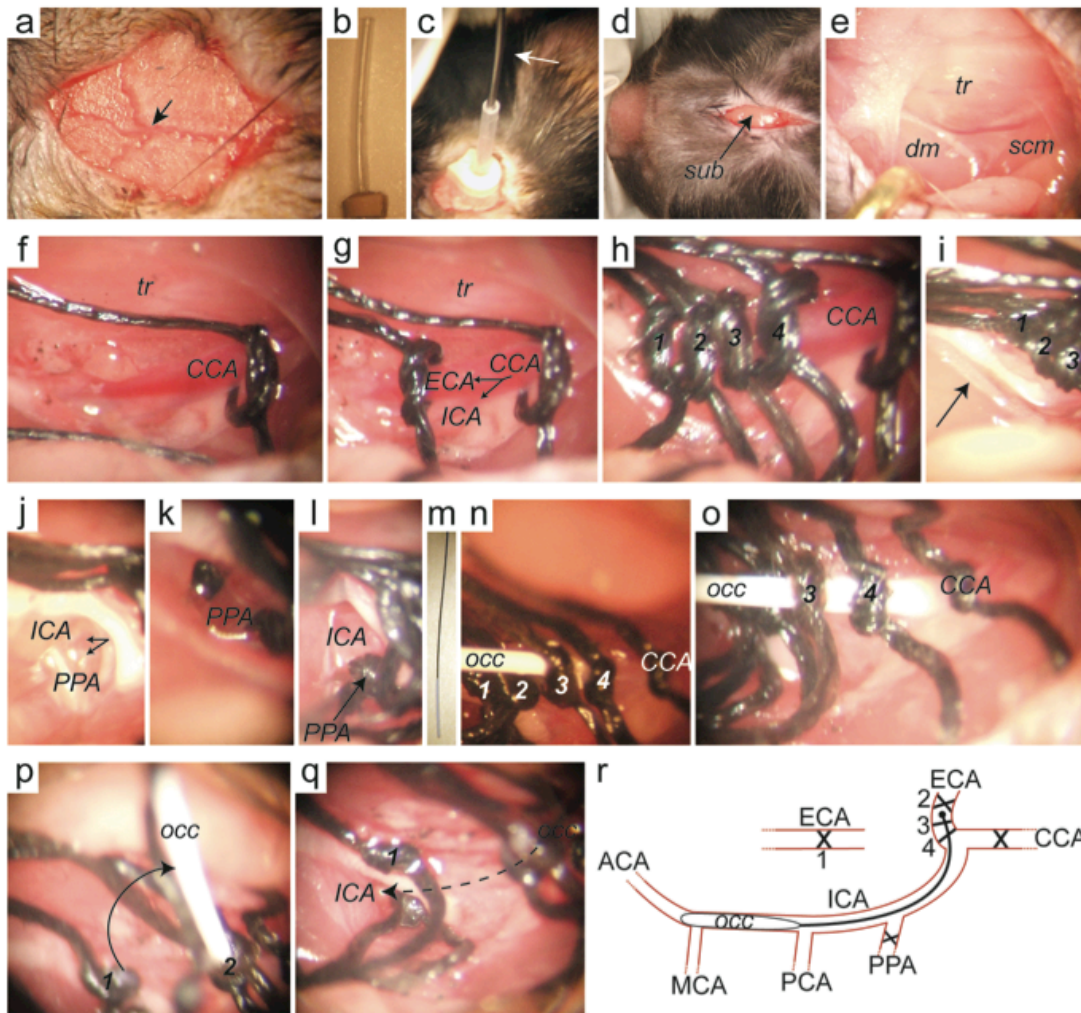


Figure 2.1. Middle cerebral artery occlusion (MCAo) surgery with cerebral blood flow monitoring. Cerebral blood flow for MCAo was recorded by positioning a laser doppler flow unit on the skull overlying MCA territory as measured relative to (a) bregma (arrow). The unit was held in place by (b) a doppler probe holder fashioned from PE-50 catheter tubing and attached to the skull surface before insertion of (c) a fine needle doppler probe (arrow). For MCAo, (d) a midline incision was made in the ventral neck of the mouse, revealing the submandibular gland (sub). Blunt dissection of the gland revealed the underlying (e) trachea (tr), right digastric muscle (dm), and sternocleidomastoid muscle (scm). Coursing parallel to tr is the (f) common carotid artery (CCA), that was loosely tied with 6-0 silk suture thread caudal to its bifurcation into (g) internal carotid artery (ICA) and external carotid artery (ECA) branches (arrows). (h) Four additional sutures (1-4) were tied along the ECA. Just medial to ECA sutures 1-3 lies (i) a nerve (arrow) that was separated from dm to reveal (j) the pterygopalatine artery (PPA) branch of the ICA (arrows). (k-l) The PPA (arrow) was permanently ligated, as were ECA sutures 1 and 2. (m) An occluding monofilament (occ) was (n) introduced into external carotid artery between ECA sutures 2 and 3 and (o) advanced to the carotid

Figure 2.1 (Continued).

bifurcation. The ECA was cut between sutures 1 and 2, and (p) the occluding monofilament rotated such that it entered the ICA (arrow). (q) The monofilament was advanced through the ICA (arrow) to the branchpoint of the MCA, where it induces ischemia. (r) A schematic of the final monofilament placement relative to the ICA, ECA, the posterior cerebral artery (PCA) and anterior cerebral artery (ACA) is shown with ligatures marked by 'X' and collar sutures around the monofilament denoted by '\

attached to the skull surface 3.5 mm lateral and 1.5 mm posterior to bregma using a combination of cyanoacrylate glue and cyanoacrylate accelerator solution (ZAP). This site was selected because it overlies the central core of ischemic territory in the MCAo model (Shimizu-Sasamata, Bosque-Hamilton et al. 1998). The doppler probe was introduced into the probe holder lumen and held in full contact with the skull using a hands-free clamp (Figure 2.1c). The outputs of the doppler and rectal temperature probes were collected using the Powerlab Data Acquisition System (AD Instruments). Real-time cerebral blood flow and temperature readings were recorded and displayed with LabChart 5 software (AD Instruments) throughout the experiment.

MCAo surgery was carried out with the mouse in the supine position. A 1-cm midline incision was made in the neck to reveal the submandibular gland (Figure 2.1d). The gland was bluntly dissected away and retracted to reveal the triangular junction of trachea, right digastric muscle, and right sternocleidomastoid muscle (Figure 2.1e). Superficial vessels in this junction were cauterized with a fine-tipped cautery pen, and the right carotid sheath, containing the common carotid artery (CCA) and vagus nerve, identified along its course running parallel to the trachea. The CCA was dissected away from the surrounding structures without making contact with the vagus nerve, and size 6-0 silk suture thread (Ethilon) loosely tied around the artery where it emerged from beneath the sternocleidomastoid muscle (Figure 2.1f). The CCA bifurcates just rostral to this point into the internal carotid artery (ICA) and external carotid artery (ECA). Another suture was tied along the ECA (Figure 2.1g). The suture was used to pull the ECA laterally to aid in the identification and cauterization of small branches of the ECA, including the occipital and superior thyroid arteries. Three additional sutures were tied

along the ECA for a total of four (Figure 2.1h). Rostral and lateral to the tied sutures lies a nerve that runs along the digastric muscle (Figure 2.1i). Figure 2.1j shows the nerve after it has been separated from the digastric muscle and bluntly dissected medially to reveal the ICA and its branch, the pterygopalatine artery (PPA). A ligature was permanently tied around the PPA (Figure 2.1k-l) to prevent any collateral circulation to the brain that could influence the MCAo model in this strain (Chen, Ito et al. 2008). In preparation for the introduction of the occluding monofilament into the ECA, the suture loosely-tied around the CCA and ECA suture 4 was temporarily ligated, and ECA sutures 1 and 2 were permanently ligated to prevent any back-flow of blood. A pair of micro-dissecting spring scissors were used to cut a small hole between ECA sutures 2 and 3. A 20-mm long silicon rubber-coated 6-0 size occluding monofilament with coating diameter of 0.23 ± 0.02 mm (Figure 2.1m, Doccol Corporation) was introduced into the hole and advanced past suture 3, where it was tied in place by ECA suture 3 (Figure 2.1n). Suture 4 was loosened, the monofilament was advanced to the common carotid bifurcation and suture 4 tightened around it (Figure 2.1o). The ECA was sectioned between sutures 1 and 2, and suture 2 was lifted caudally to maneuver the tip of the occluding monofilament from the bifurcation into the ICA (Figure 2.1p). ECA sutures 3 and 4 were loosened slightly and the monofilament was advanced in the ICA past the PPA to the branch point of the MCA, approximately 9-11 mm from the bifurcation of the CCA (Figure 2.1q). A schematic of the final occluding monofilament placement during the ischemic phase of MCAo is shown in Figure 2.1r. Occlusion of the MCA was characterized by a sharp reduction in cerebral blood flow to less than 25% of baseline levels. In preliminary experiments, stroke volume was assessed as a function of

occlusion time (i.e., 15, 30, 60 min or permanent occlusion) to identify a duration that resulted in the most stereotyped infarcts. Transient cerebral ischemia of 60 minutes was selected for all experiments unless otherwise stated. After the designated occlusion time elapsed, the occluding monofilament was removed and blood flow restored in the ischemic right hemisphere. Upon removal of the monofilament, ECA sutures 3 and 4 were permanently ligated, and the CCA ligature was removed for full reperfusion. The fine needle doppler probe, probe holder, and rectal temperature probe were removed, and all incisions sutured closed with 5-0 silk suture thread (Ethilon). Following surgery, mice were allowed to recover from anesthesia on a heating pad attached to a circulating water heating system (Gaymar).

2.2.10 Evans Blue Dye Evaluation of Blood-Brain Barrier Permeability

The permeability of the blood-brain barrier after cerebral ischemia was evaluated using the Evans Blue dye extravasation method (Vakili, Kataoka et al. 2005). Mice were intravenously injected with 2% Evans blue dye (Sigma) in 0.9% saline at a dose of 3 ml/kg immediately after reperfusion of MCAo. Twenty-four hours later, transcardial perfusion was performed using a modification of the procedure described by Hockfield et al. (Hockfield, Carlson et al. 1993). Mice were anesthetized deeply with isoflurane in oxygen and transferred to a perfusion tray. A midline incision was made along the sternum to expose the heart. A 25-gauge winged infusion needle attached to a peristaltic pump (Econo-Pump, BioRad) for the circulation of heparinized normal saline was inserted in the left apex of the heart and advanced into the left ventricle. An incision was made in the right atrium as the peristaltic pump flow rate was initialized to 0.5 ml/min. Mice were perfused with saline for ten minutes, or until perfusate was clear and the liver

became pale in color. Following perfusion, the brain was excised and *ex vivo* imaging of Evans blue dye in whole brain or brain slices was performed using the IVIS Spectrum optical imaging system (IVIS Spectrum, Caliper Life Sciences) with excitation and emission wavelengths of 605 nm and 680 nm, respectively. Data analysis was performed using LivingImage® 4.2 software. Evans blue dyed brain slices were digitized using a Dell 810 flatbed scanner.

2.2.11 Therapeutic Treatment with MPAP-Src: Systemic Administration

The effect of systemically-administered MPAP-Src on *Src* gene expression was investigated using two treatment regimens (pre-stroke injections and post-stroke injections). Experiments were carried out using Dy547-labeled siSTABLE siRNA specific for *c-src* purchased from Dharmacon. The siRNA was dissolved in 1X siRNA buffer (Dharmacon) and separated into 50 mg aliquots (3.7 nmol Src siRNA). Twenty minutes prior to injection, a siRNA aliquot was mixed in a 1:5 ratio with Cy5.5-labeled MPAP (18.5 nmol) in 5% dextrose (Hospira) solution in a total volume of 200 μ l.

Intravenous pre-stroke tail vein injections of MPAP-Src 48 and 24 hours prior to 60-minute MCAo ischemia were tested in a cohort of mice (n=5), followed 24 hours later by behavioral testing, and *ex vivo* imaging and sacrifice. Stroke volume assessment and quantitative real time RT-PCR analysis of brains was then performed. MPAP complexes with scrambled non-targeting siRNA (MPAP-Ctrl, n=5) were selected as a negative control. Src kinase inhibitor, PP1, shown previously effective in limiting damage in stroke mice (Paul, Zhang et al. 2001), was selected as a positive control. For this, PP1 (1 mg, Enzo Life Sciences) was dissolved in sterile DMSO and further diluted in sterile 1X

PBS to a final concentration of 0.15 mg/ml. PP1 was administered by intraperitoneal injection (n=5) at a dosage of 1.5 mg/kg.

Intravenous post-stroke injection of MPAP-Src complexes (n=3, 18.5 nmol MPAP : 3.7 nmol siRNA) was also investigated. Fifteen minutes after 60-minute MCAo and reperfusion, MPAP-Src was injected by tail vein. Mice were sacrificed 72 hours after reperfusion and brains were stained with TTC (described in section 2.2.14) and processed for quantitative real time RT-PCR to evaluate the effect on stroke volume and Src expression. MPAP-Ctrl treatment served as a negative control (n=3).

2.2.12 Therapeutic Treatment with MPAP-Src: Intracerebral Injection

Intracerebral administration of MPAP-Src was investigated for its effects on *Src* gene expression. MPAP was dissolved in 5% dextrose (Hospira) in concentrations of 500 pmol/ μ l. Twenty minutes prior to injection, the MPAP solutions were mixed with an equal volume of c-Src siRNA (siSTABLE, Dharmacon) in a 5:1 molar ratio (500 pmol/ μ l MPAP:100 pmol/ μ l siRNA) to form MPAP-Src complexes. MPAP-siRNA mixtures formed using scrambled control siRNA (MPAP-Ctrl) were used as negative controls.

Ten male, 10-12-week-old C57BL/6 mice were anesthetized in 2.0-2.5% isoflurane in 30%/70% oxygen/nitrous oxide gas vehicle, and anesthesia was maintained at 1.0-1.5% isoflurane during surgery. Mice were transferred and secured to a small animal stereotactic instrument (Kopf) with a Quintessential Stereotactic Injector (Stoelting Company) for controlled microinjection. A 5-mm incision was made in the scalp, and the skull surface was wiped clean of loose tissues until the landmark bregma was clearly visible. A hole was drilled through the skull over the right hemisphere, 2.5-mm lateral and 0.8-mm posterior to bregma, using a high speed micro drill with 0.7-mm

steel burrs (Fine Science Tools). In five mice, a total of 2 μ l of MPAP-Src solution (i.e., 100 pmol siRNA per injection) was injected through the hole at a depth of 2.5 mm from the skull surface using a 701RN 10- μ l syringe with a 26-gauge needle attachment (Hamilton Company). This injection location was selected because it was the most common site of infarction identified in our preliminary middle cerebral artery occlusion studies. An identical procedure was repeated for the remaining five mice with the same volume of MPAP-Ctrl complexes. Injection occurred at a rate of 0.25 μ l/minute. After injection was complete, the hole was patched with bone wax (Fine Science Tools) and the skin incision closed with 5-0 silk suture thread (Ethilon). Postoperative buprenorphine (0.05 mg/kg subcutaneous, Bedford Labs) was administered every 12 hours or as needed. Mice were sacrificed 24-hours after injection and their brains processed for quantitative real time RT-PCR. Ten additional mice were treated as described and subjected to 60-minute MCAo 24-hours after injection to determine the influence of *Src* expression knockdown on infarct volume after stroke.

2.2.13 Concentration Dependence of Intracerebrally-Injected MPAP-Src

MPAP-Src concentration effects were evaluated in male C57BL/6 mice injected in the right and left cerebral hemispheres with MPAP-Src and MPAP-Ctrl, respectively. MPAP was dissolved in 5% dextrose (Hospira) in concentrations of 125, 500 and 2000 pmol/ μ l. Twenty minutes prior to injection, the MPAP solutions were mixed with an equal volume of c-Src siRNA in a 5:1 molar ratio (i.e., 25, 100 or 400 pmol/ μ l siRNA, respectively) to form MPAP-Src complexes. Mice were anesthetized with isofluorane and mounted on the stereotactic frame. Holes were drilled through the skull over the left and right hemispheres, 2.5-mm lateral and 0.8-mm posterior to bregma. MPAP-Src was

injected at a depth of 2.5 mm relative to the skull surface through the right hole, while MPAP-Ctrl complexes of the same concentration were injected at the same depth through the left. Seventy-two hours after injection, mice were sacrificed and their brain hemispheres evaluated by western blot analysis.

2.2.14 Stroke Volume Assessment by Triphenyltetrazolium Chloride (TTC) Staining

Quantification of cerebral infarct volume following transient MCAo by triphenyltetrazolium chloride staining was performed according to the protocol described by Joshi et al (Joshi, Jain et al. 2004). Mice were anesthetized with isoflurane and sacrificed by decapitation. The brain was removed from the skull and placed in an acrylic adjustable brain matrix (Braintree Scientific) for sectioning. The brain matrix was submerged in phosphate-buffered saline (PBS, pH 7.4) and the brain sliced into 2-mm coronal sections using a razor blade. Brain slices were transferred to 0.05% (w/v) TTC in PBS, and incubated at 37°C for 20 minutes. Upon staining, viable brain tissue acquires a deep red color, while infarcted stroke tissue remains white. Slices were placed on a glass coverslip, caudal side down, and digitized using a Dell 810 flatbed scanner. When tissues were needed for RT-PCR or western blot analysis, the third slice of the series was snap frozen, and the rostral portion of TTC-stained slice 4 was used to approximate the infarct volume of the caudal portion of slice 3 (Joshi, Jain et al. 2004). Image analysis was performed using Adobe Photoshop CS4 software. For this, the infarcted area of each slice was measured by an observer who was blinded to the type of treatment received by the mice. Infarct volume was estimated by multiplying the area by slice thickness. The total percentage of infarct volume was calculated according to the Swanson method that corrects for edematous swelling of stroke tissues (Swanson, Morton et al. 1990). The

Swanson corrected volume was calculated using the equation, $100 \times [(\text{contralateral hemisphere volume}) - (\text{non-lesioned ipsilateral hemisphere volume})] / (\text{contralateral hemisphere volume})$, where ipsilateral refers to the infarcted brain hemisphere (i.e., right hemisphere) and contralateral to the unaffected (left) hemisphere. Results were analyzed with one-way ANOVA and Bonferroni T-test for pairwise comparisons. Brain edema, as quantified by ipsilateral hemispheric enlargement (Manley, Fujimura et al. 2000), was also calculated to evaluate the effect of probe treatment on vascular permeability.

2.2.15 Behavioral Testing

Mice were subjected to behavioral tests 24-hours after ischemia according to the following procedure to determine if probe treatment had any effect on functional outcome.

Neurological Score. Evaluation of neurological deficits was performed. Mice were scored using the following scoring system to assess the functional consequences of stroke: 0 – no behavioral abnormality detected; 1 – bending of the torso to the ipsilateral side when held by tail; 2 – spontaneous turning behavior; 3 – spontaneous circling behavior, 4 - barrel rolling; 5 – no motor activity (Hara, Huang et al. 1996; Zhang, Chopp et al. 1997; Hunter, Hatcher et al. 2000). Statistical analysis of scores was using Kruskal –Wallis one-way ANOVA.

Rotarod Testing. To test the effect of stroke on coordination, mice were evaluated using a rotarod apparatus that consists of a 3-cm diameter drum that rotates at 8 revolutions per minute. Prior to surgery, mice were habituated to walking on the rotarod until they could routinely demonstrate the ability to remain on the drum for 2 minutes. Twenty-four hours after surgery the mice were tested on the rotarod and the latency

before falling was recorded. Two trials were performed, and the longest latency was selected for analysis (Hayakawa, Nakano et al. 2010).

2.2.16 Western Blot Analysis

Protein samples from mouse brains were isolated either with the Nucleospin Total RNA and Protein Isolation kit (Clontech), or by disruption with a rotor-stator homogenizer in RIPA buffer supplemented with the Halt Protease Inhibitor Cocktail (Thermo Scientific). Samples were quantified by Pierce BCA assay (Thermo Scientific). A total of 40 µg protein per sample was prepared for sodium dodecyl sulfate polyacrylamide gel electrophoresis (SDS-PAGE) by mixing with 2X Laemmli Buffer (BioRad) containing β-mercaptoethanol and denaturing at 95°C for five minutes. The samples were loaded onto Novex 4-20% Tris-Glycine Mini Gels (Invitrogen) and separated at 125 V for 90 minutes. The protein was transferred from gel to 0.2 µm nitrocellulose membrane for 90 minutes at 20 V. The membrane was blocked in 5% non-fat dry milk in Tris Buffer Saline (TBS, BioRad) for one hour at 4°C. The membrane was then incubated in primary antibody for Src (ab47405 rabbit anti-mouse polyclonal, Abcam) diluted 1:500 in TBS containing 0.1% Tween 20 (TBST) for 2.5 hours at room temperature or overnight at 4°C. This was followed by TBST washes and incubation in goat anti-rabbit secondary antibody conjugated to horseradish peroxidase (1:2000, ab6721, Abcam) for 1 hour at room temperature. The membrane was washed and incubated in SuperSignal West Pico Chemiluminescent Substrate (Thermo Scientific) for five minutes before being exposed to film or visualized by imaging system. Src protein was quantified relative to beta actin standard (primary antibody 1:2000, ab8227, abcam) using ImageJ (NIH) or Living Image 4.2 software (Caliper).

2.2.17 Fluorescence Optical Imaging

In vivo and *ex vivo* near-infrared optical imaging was performed using a whole-body optical imaging system (IVIS Spectrum, Caliper Life Sciences) for visualization of Cy5.5-labeled probe accumulations. Anesthetized mice or excised brain tissue samples were imaged at excitation and emission wavelengths 675 nm and 720 nm, respectively.

2.3 Results

2.3.1 Characterization of MPAP-Src Probes

MPAP has proven effective as a membrane translocation moiety when covalently linked to optical probes and iron oxide nanoparticles (Pham, Zhao et al. 2005; Medarova, Pham et al. 2007; Kumar, Medarova et al. 2010). In this work we wished to extend the use of optically labeled MPAP further by taking advantage of the potential for its poly-arginine residues to electrostatically interact with negatively-charged siRNA molecules. To promote the formation of siRNA dual optical imaging probes, c-Src siRNA-Dy547 and MPAP-Cy5.5 were mixed in several molar ratios. The efficiency of MPAP binding to siRNA was determined by gel electrophoresis on the resulting MPAP-Src solutions to assess the proportion of free siRNA in each mixture. MPAP-Src complexes remained in the loading well during gel electrophoresis, while uncomplexed siRNA readily entered the gel and stained with ethidium bromide (Figure 2.2a). In solutions containing a 1:5 siRNA-to-MPAP molar ratio or higher peptide content, the vast majority of siRNA was associated with MPAP. Full incorporation of siRNA into probes was deemed important to maximize siRNA internalization and silencing potential. Thus, the siRNA-to-peptide ratio at which no discernible siRNA remained unassociated with MPAP-Cy5.5, 1:5, was used for subsequent experiments. Ultimate utility of MPAP-Src *in vivo* requires

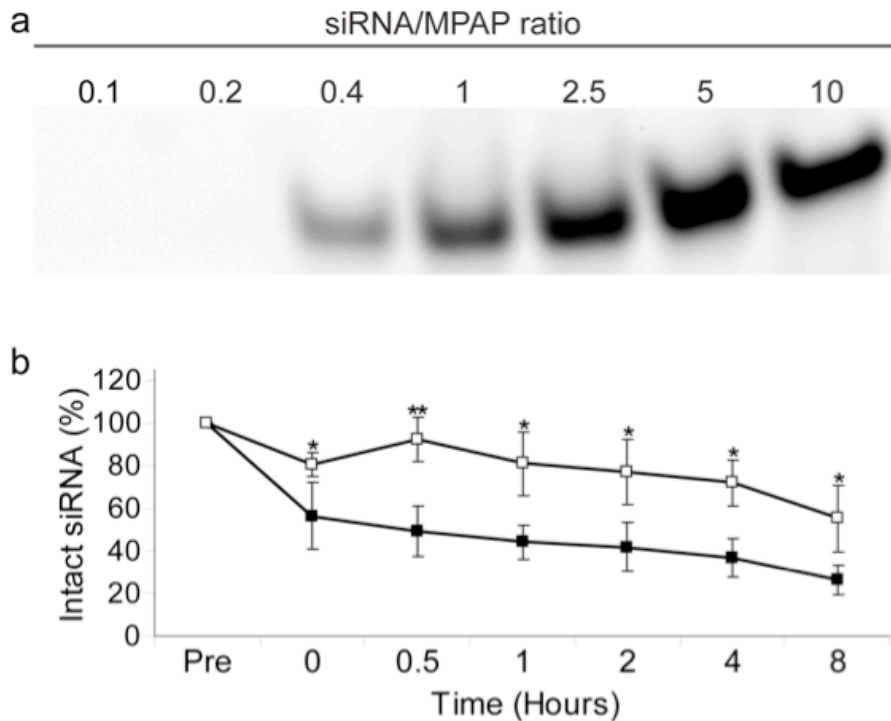


Figure 2.2. Gel mobility shift assay and serum stability. (a) MPAP-Cy5.5 was incubated with c-Src siRNA at several molar ratios to form MPAP-Src probes. At the 0.4 siRNA-to-MPAP ratio, most siRNA was incorporated into complexes. Complexes composed of 1 siRNA molecule for each 5 molecules of MPAP were used for all further analysis. (b) Stability of MPAP-Src (open squares) in serum relative to Dy547-labeled c-src siRNA alone (closed squares) was investigated by incubating probes in 75% mouse serum for 0-8 hours. MPAP complexation to siRNA confers partial protection from serum nucleases, yielding a higher percentage of intact siRNA after incubation in serum than siRNA alone (mean±s.d.) relative to undigested controls (Pre). Statistical analysis indicated significant siRNA protection by MPAP at all incubation durations (* $p < 0.01$, ** $p < 0.001$).

protection of siRNA from nucleases in the bloodstream. Generally, siRNAs are chemically modified to extend their serum half-life relative to naked siRNA, which becomes degraded and inactivated within minutes of blood exposure (Braasch, Jensen et al. 2003; Soutschek, Akinc et al. 2004). To investigate the stability of the siRNA incorporated into MPAP-Src, siRNA complexes and naked siRNA-Dy547 were exposed to serum for up to 8 hours. Following removal of serum proteins and MPAP with proteinase K (1 mg/ml), intact siRNA was analyzed by gel electrophoresis and quantified (Figure 2.2b). It was observed that the optical label Dy547 conjugated to c-Src siRNA partially protects it from degradation by nucleases, with just over 25% of the total siRNA retained after 8 hours. The presence of MPAP appears to confer an additional measure of protection, such that the amount of free siRNA after 8 hours of MPAP-Src incubation in serum was close to 55%. These results indicate that MPAP complexation has a stabilizing effect on c-Src siRNA.

2.3.2 In Vitro Testing of MPAP-Src Probes

Internalization of MPAP-Src probes was evaluated in vitro in a variety of cell types implicated in ischemic stroke pathology, including primary cortical neurons, astrocytes and the bEnd.3 brain endothelial cell line. Cells incubated for 24 hours with MPAP-Src or MPAP associated with scrambled control siRNA (MPAP-Ctrl) were subjected to flow cytometry and monitored for Cy5.5 and Dy547 fluorescence. Figure 2.3 shows significant signal from both siRNA and MPAP relative to untreated controls in all cell types. Internalization of MPAP-Src and MPAP-Ctrl occurred in similar patterns, indicating that MPAP association with Src siRNA is not sequence dependent.

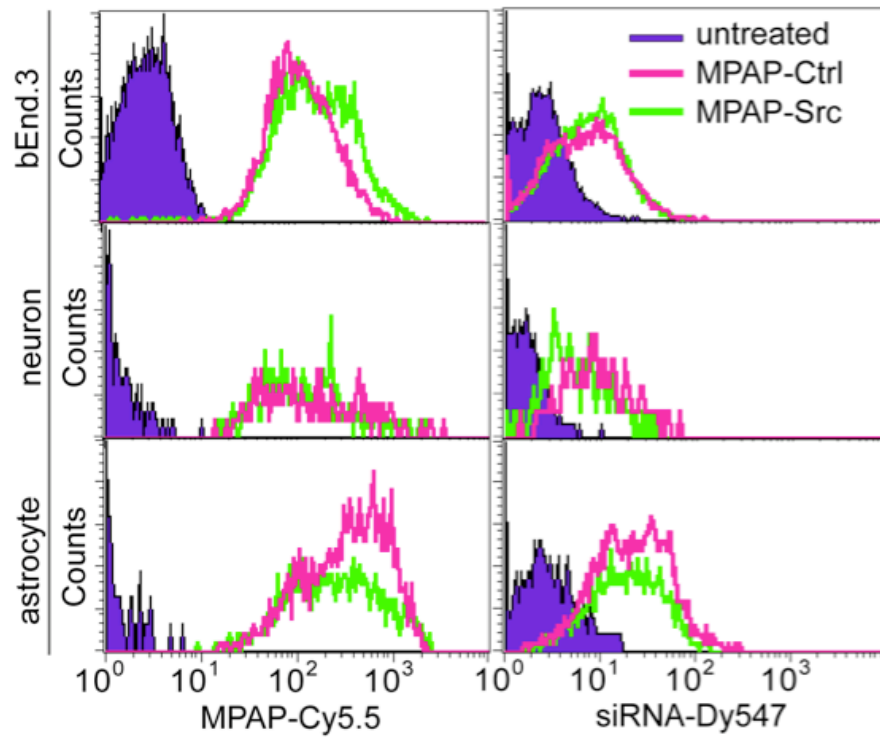


Figure 2.3. Flow cytometry. Astrocytes, neurons and bEnd.3 cells were incubated with MPAP-Src or MPAP-Ctrl for 24 hours and then analyzed with flow cytometry. All cell types were positive for the presence of both MPAP-Cy5.5 and siRNA-Dy547.

To confirm that MPAP-Src probe was internalized by cells, and not passively associated with the cell membrane, confocal microscopy was performed. Neurons, astrocytes and bEnd.3 cells stained with cell-specific antibodies (Figure 2.4a-c) were positive for the presence of both MPAP (Figure 2.4d-f) and Src siRNA (Figure 2.4g-i). In general, Src siRNA colocalized with MPAP (Figure 2.4j-l), though, for neurons in particular, there was evidence that MPAP and siRNA became dissociated to some degree when taken up by cells (Figure 2.4k). The presence of MPAP was crucial for internalization, as evident by the complete absence of Src siRNA uptake relative to MPAP-Src when cells were incubated with equivalent quantities of siRNA alone (Figure 2.4m-o).

It has been reported that fixation can induce artifacts in cell-penetrating peptides studies, causing abnormal localization of peptides in the nucleus of target cells. To provide more precise evidence of MPAP-Src delivery, we performed live cell imaging on unfixed, treated astrocytes, bEnd.3 cells and neurons. In these studies the mechanism of cellular internalization was also investigated using Lysosensor Green staining, which is specific for endosomal vesicles (Figure 2.5a-c). As in fixed cells, MPAP-Src substantially entered cells (Figure 2.5d-i). MPAP and Src signal was present in punctate form and often colocalized with Lysosensor Green staining in each of the cell types, suggesting that one mechanism of MPAP uptake is endocytosis (Figure 2.5j-l). However, diffuse probe signal was also present throughout the cytoplasm and in occasional Lysosensor negative spots, indicating that some portion of material escapes endosomal compartmentalization. Generally, MPAP and siRNA signals colocalized in cells, prompting us to wonder whether siRNA would be able access RNAi machinery to

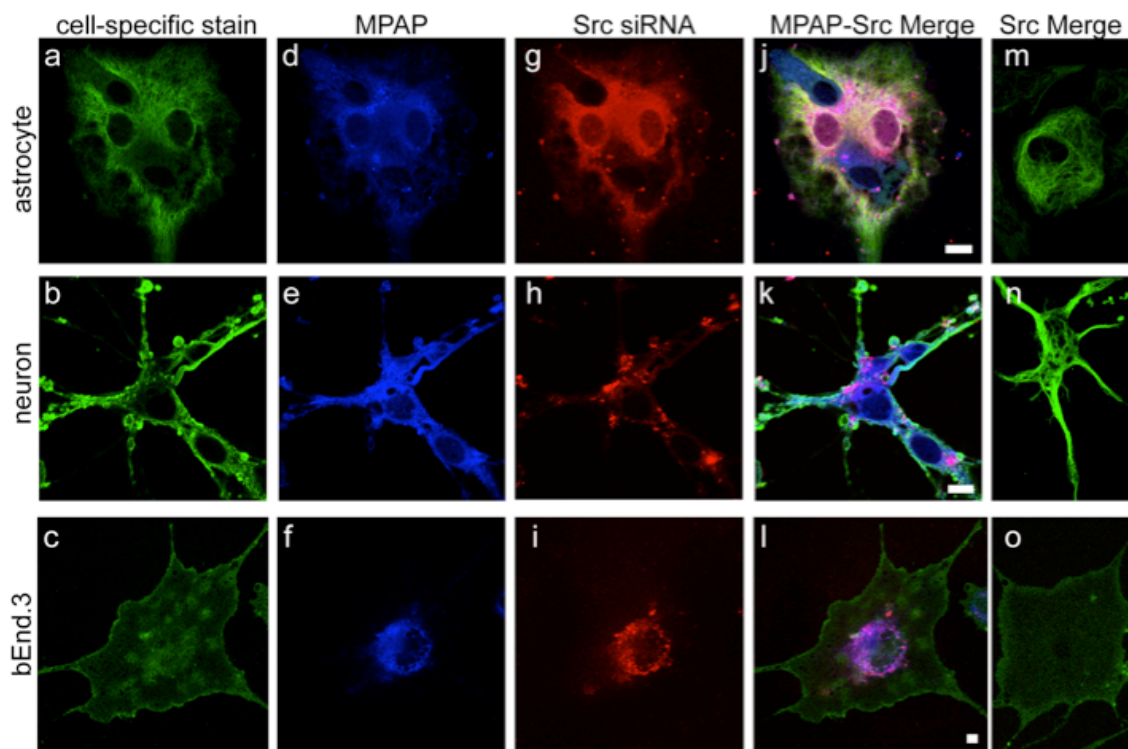


Figure 2.4. Cellular uptake of MPAP-Src probes. Confocal microscopy of astrocytes, neurons and bEnd.3 stained with GFAP (a), beta-III tubulin (b), and CD31 (c), respectively. Following incubation with MPAP-Src probe for 24 hours and cell-specific staining, cells were visualized by confocal microscopy. MPAP (d-f) and Src siRNA (g-i) were taken up by cells following MPAP-Src incubation, whereas incubation with Src siRNA alone resulted in no detectable siRNA accumulations (m-o). Scale bar = 10 μ m.

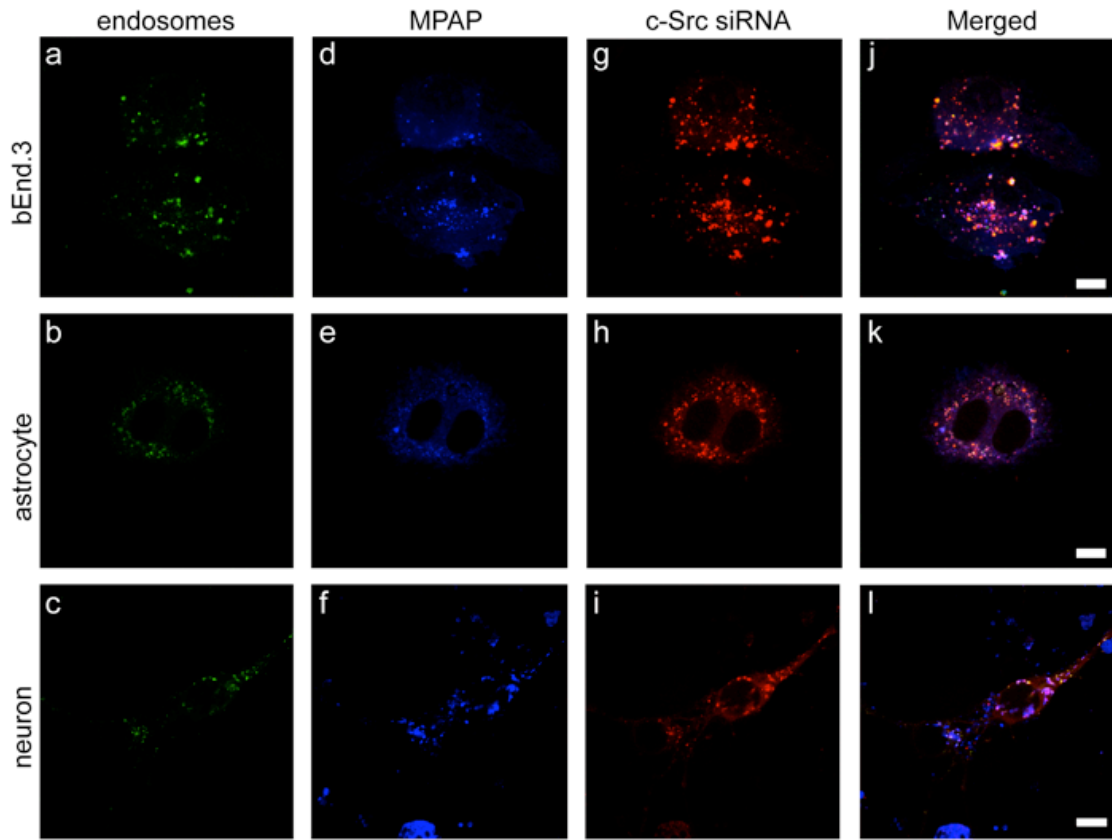


Figure 2.5. Uptake mechanism of MPAP-Src. Cells were visualized using confocal microscopy following Lysosensor Green staining of unfixed astrocytes, bEnd.3 cells and neurons (a-c) to determine the mechanism of cellular uptake of MPAP-Src. MPAP (d-f) and c-Src siRNA (g-i) generally co-localize with endosomal vesicles (j-l). Scale bar = 10 μ m.

achieve successful Src silencing. To address this, expression levels of endogenous Src mRNA were evaluated by RT-PCR following MPAP-Src uptake. Total Src expression after MPAP-Src treatment was compared to expression after treatment with MPAP-Ctrl, a control used to differentiate siRNA-induced Src inhibition from off-target effects potentially caused by the MPAP method of siRNA delivery. Endogenous Src levels were reduced to a statistically significant degree in all cell types subjected to MPAP-Src treatment for 48 hours relative to controls (Figure 2.6). For astrocytes and bEnd.3 cells, Src expression decreased to approximately 66% of controls, while in neurons the decrease was to 75%. Similar reductions in Src levels were achieved following 24-hour MPAP-Src treatment in astrocytes and bEnd.3 cells (data not shown). Thus, despite the observation that MPAP-Src appears to traffic to some extent in endosomal vesicles, the endosomal escape of siRNA and its separation from MPAP is sufficient to mediate a significant degree of endogenous gene inhibition.

To determine if MPAP-Src mediated siRNA delivery was cytotoxic, MTT assays were performed. MPAP-Src treatment resulted in no discernable increase in cytotoxicity in neurons, astrocytes or bEnd.3 cells relative to untreated controls (Figure 2.7). These data were confirmed by an additional test of cytotoxicity, the caspase-3 apoptosis assay, which likewise revealed no significant toxicity of MPAP-Src treatment. These data indicate that MPAP-Src treatment induced partial endogenous gene silencing without the degree of cytotoxicity that is often observed in other peptide-based delivery systems (Saar, Lindgren et al. 2005).

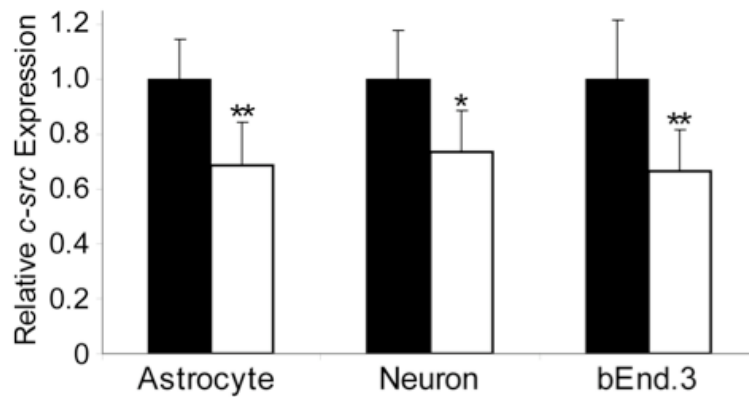


Figure 2.6. Bioactivity of MPAP-Src probes. Quantitative RT-PCR analysis of endogenous Src mRNA expression levels in astrocytes, neurons and bEnd.3 cells after MPAP-Ctrl (black bars) or MPAP-Src (white bars) treatment was performed. After administration of MPAP-Src, there was a significant reduction in *c-src* levels in all cell types tested (n=7, *p<0.05, **p<0.01).

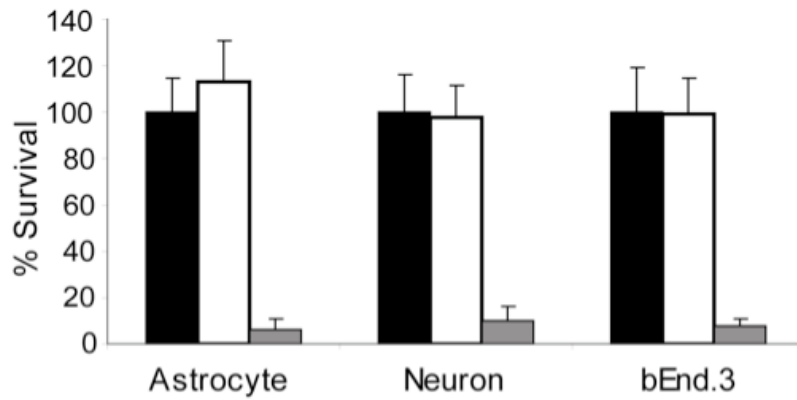


Figure 2.7. Cytotoxicity Assays. The percent survival (mean \pm s.d.) of cells treated with MPAP-Src or staurosporine (white and gray bars, respectively) relative to untreated controls (black bars) was obtained by MTT analysis. MPAP-Src treatment resulted in no significant increase in cytotoxicity in any of the cell types.

2.3.3 MPAP Delivery in Experimental Stroke

After demonstrating that MPAP facilitates the delivery of functional siRNA to cells of the central nervous system in an *in vitro* setting, we transitioned to testing of MPAP-Src in experimental stroke. Previous studies in our laboratory showed that MPAP bearing fluorescent cargoes was detected in the brain within six hours of intravenous administration, with increasing accumulations in neurons, astrocytes and endothelial cells detected at 24 and 48 hours in healthy mice (Pham, Zhao et al. 2005). During our characterization of MPAP probes, it was observed that complexation with siRNA leads to a slight depression of probe zeta potential (MPAP: 56.4 to MPAP-siRNA: 42.3 ± 6.55 in H₂O, pH 5.4). This denotes the general stability of both probes, with an increased tendency for MPAP-Src to self-associate relative to MPAP alone. In cell studies, these differences did not have a detrimental effect on MPAP-Src's ability to enter cells and downregulate endogenous Src levels. However, in an *in vivo* environment it is reasonable to assume that modification of MPAP with siRNA cargoes may change the trafficking of MPAP probes and ultimately their brain penetrating capabilities in normal animals. Although penetration of an intact blood-brain barrier would be an essential characteristic of therapeutics for many CNS diseases, it is not a crucial issue in the setting of stroke, where blood-brain barrier dysfunction leads to compromise of the vasculature and leakage in ischemic tissue. We hypothesized that this breakdown would provide an avenue for MPAP-Src delivery and enable probe accumulations beyond those observed in normal mice. This was a critical factor we considered while selecting an experimental animal model of stroke for the evaluation of MPAP-Src probes.

The middle cerebral artery is the most common site of blockage found in ischemic stroke in humans, leading to focal infarction and impairment in movement and cognition (Paciaroni, Silvestrelli et al. 2003; Ng, Stein et al. 2007). Experimental stroke models that employ middle cerebral artery occlusion (MCAo) have been developed in mice and rats (Longa, Weinstein et al. 1989; Belayev, Busto et al. 1999). These simulate the human condition through artificial restriction of blood flow to the MCA territory via occluding suture, embolus, or cautery (Zhang, Chopp et al. 1997; Belayev, Busto et al. 1999; Furuya, Kawahara et al. 2004). For our experiments, we selected the C57BL/6 mouse strain and investigated the intraluminal suture method of MCAo at a variety of occlusion durations (i.e., 15, 30, 60 and permanent). This enabled us to select the conditions that resulted in the most stereotyped infarcts and lowest animal mortality. Infarct volume was assessed by TTC staining, which causes viable brain tissue to turn a deep red color and infarcted tissue to remain white. Representative brain slices for each occlusion duration are shown in Figure 2.8. Brief 15-minute occlusion of the mouse MCA rarely led to detectable tissue death or neurological deficits. In contrast, mice subjected to 30-minute occlusion had highly variable stroke volume and territory, with an average infarct volume of $12.6 \pm 7.2 \text{ mm}^3$. Occlusion of 90 minutes or more was associated with animal morbidities that prevented long-term monitoring or behavioral evaluation. For mice subjected to 60-minute MCAo, average stroke volumes ($27.0 \pm 4.7 \text{ mm}^3$) were within the range of those published in the literature (Chen, Ito et al. 2008). Additionally, 60-minute occlusion was associated with blood-brain barrier breakdown that was grossly evident in serial tissue sections (Figure 2.8, arrows). Breakdown was confirmed by extravasation of Evans blue dye, which associates with serum albumin and is normally excluded from

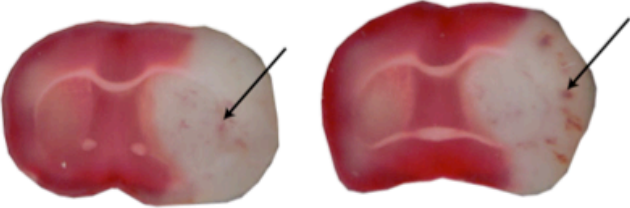
Occlusion Duration	TTC-Stained Sections	Infarct Volume (mm ³)
15 min		0 (n=2)
30 min		12.6 ± 7.2 (n=7)
60 min		27.0 ± 4.7 (n=5)
permanent		53.6 ± 14.9 (n=4)

Figure 2.8. The effect of occlusion duration on infarct volume. Mice subjected to 15 min, 30 min, 60 min, or permanent intraluminal MCAo were sacrificed 24-hours after reperfusion. Excised brains were TTC stained to identify white infarcted regions, which can be differentiated from red viable tissues after staining. Representative coronal brain slices (+0.4 to -0.8 mm rostral to bregma) are shown. Arrows denote regions of vascular breakdown observed in the infarcted tissues of mice subjected to 60-min occlusions. Infarct volumes (mean±s.d.) were calculated according to the procedure described by Swanson et. al (1990).

the central nervous system unless the blood-brain barrier is compromised (Wolman, Klatzo et al. 1981). Figure 2.9 shows *ex vivo* imaging of Evans blue dye extravasation into the ischemic hemisphere of the whole mouse brain (Figure 2.9a) and in coronal brain slices (Figure 2.9b). Vascular leakage of Evans blue dye was also apparent in fresh brain tissue sections (Figure 2.9c).

In addition, we found that the blood-brain barrier permeability detected in our experimental stroke model enhances the delivery of MPAP-Src to ischemic tissues. We used fluorescence imaging to evaluate the localization patterns of MPAP probes in the brain 48 hours after intravenous injection (Figure 2.10). MPAP (Figure 2.10b) and MPAP-Src (Figure 2.10c) exhibited a similar degree of brain accumulation above background levels (Figure 2.10a). Delivery was markedly increased in the ischemic hemisphere when MPAP-Src was administered after the induction of stroke (2.10d). Improved delivery was also observed in mice pretreated with MPAP-Src before ischemia (see Section 2.3.4). These results prompted us to evaluate the therapeutic potential of MPAP-Src probes for ischemic stroke.

2.3.4 The Efficacy of MPAP-Src Pretreatment in Experimental Stroke

MPAP-Src probes were first evaluated in a pretreatment stroke model in which male, 10-12 week old C57BL/6 mice were subjected to 60-minute occlusion after receiving two doses of MPAP-Src or control probes. Probe administration (18.5 nmol MPAP: 3.7 nmol siRNA in 200 μ l of 5% dextrose) was performed 48 and 24 hours prior to stroke induction. This dosing schedule was informed first, by our *in vitro* experiments in which knockdown of Src was first detected at 24 hours after treatment and second, by our observations of the timing of *in vivo* trafficking of MPAP, and by extension, MPAP-

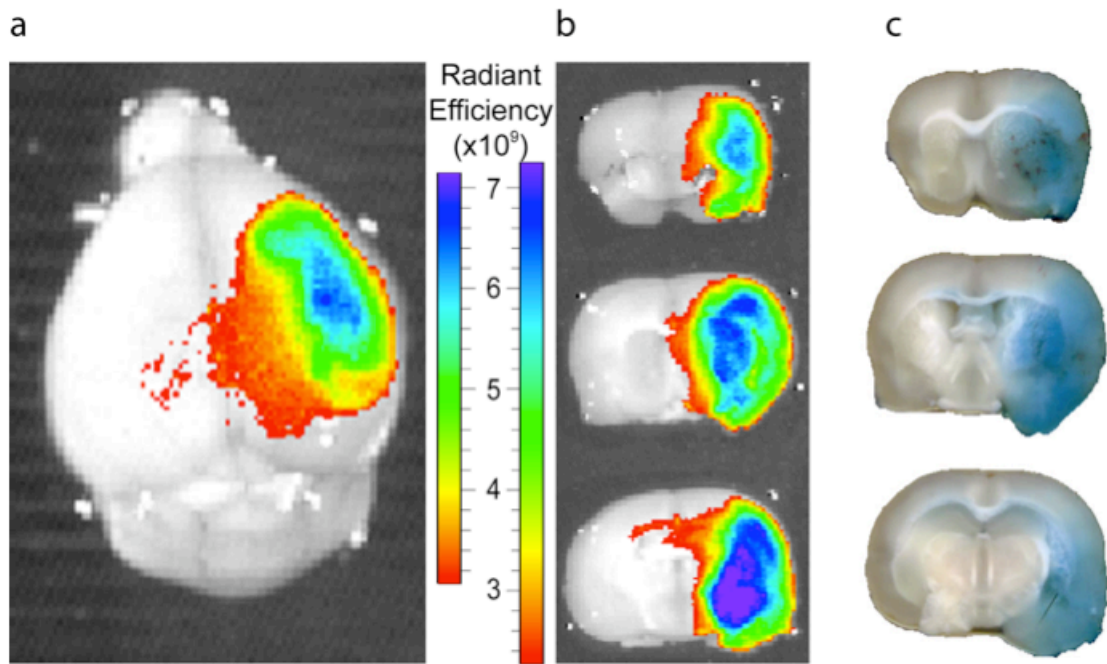


Figure 2.9. Ex vivo detection of Evans blue dye extravasation. Mice subjected to 60-minute MCAo were intravenously injected with Evans blue dye at the time of reperfusion, and sacrificed 24 hours later. Fluorescence imaging of Evans blue dye (excitation 605 nm, emission 680 nm) using the IVIS optical imaging system revealed blood-brain barrier compromise in the ischemic hemisphere of perfused whole brain (a) and in sequential coronal brain slices (b). The presence of Evans blue dye was also grossly evident in fresh tissue slices (c). Radiant efficiency: [emission light (photons/sec/cm²/str)]/[excitation light (mW/cm²)].

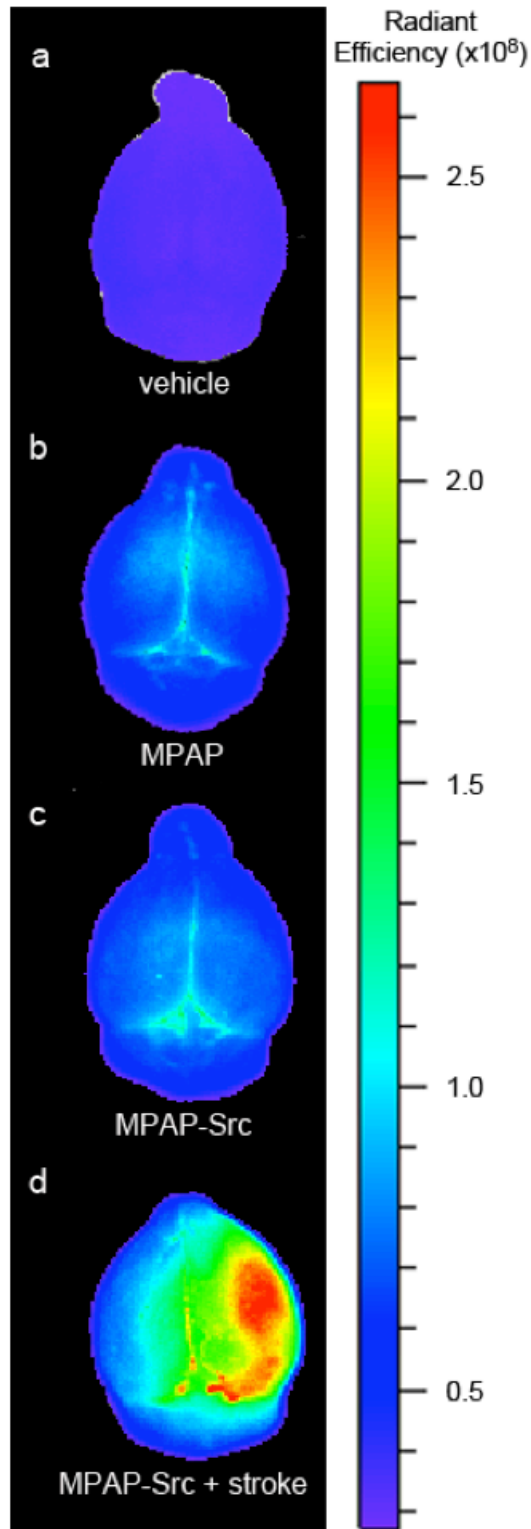


Figure 2.10. Fluorescence imaging of MPAP-Src probe delivery. Excised brains from mice intravenously injected with (a) vehicle (5% dextrose), (b) MPAP (18.5 nmol in 5% dextrose) or (c) MPAP-Src (18.5 nmol MPAP:3.7 nmol c-src siRNA in 5% dextrose) and perfused with heparinized saline (2 units/ml in 0.9% saline) 48 hours later are shown.

Figure 2.10 (Continued). When MPAP-Src is administered after ischemia at the time of reperfusion (d), delivery is enhanced beyond that observed in MPAP and MPAP-Src treated mice. Radiant efficiency: [emission light (photons/sec/cm²/str)]/[excitation light (mW/cm²)].

Src probes. MPAP complexed to scrambled non-targeting siRNA (MPAP-Ctrl) served as a negative control. Positive control treatment entailed the administration of PP1, which has been shown to mitigate stroke damage when administered 15 minutes after reperfusion (Paul, Zhang et al. 2001). Twenty-four hours after reperfusion mice were sacrificed and their brains subjected to ex vivo imaging using the IVIS Spectrum optical imaging system (Figure 2.11). Imaging revealed significant accumulations of MPAP probes (Figure 2.11a, b), particularly in the ipsilateral, or stroke hemisphere. Quantification of probe fluorescence showed that these accumulations were significant, demonstrating that the blood-brain barrier breakdown associated with stroke improves the delivery of probes (Figure 2.11c) even when they are administered prior to stroke induction. To determine if these probe accumulations had an effect on Src expression, we performed RT-PCR analysis of Src mRNA expression in a cohort of animals (n=5 per treatment type). These studies showed a 36% increase in Src expression in the ipsilateral hemispheres of MPAP-Src treated mice compared with MPAP-Ctrl treated mice. Closer examination led us to conclude that these results are likely artifactual. In these brains, mRNA extraction was performed according to a published procedure, which claimed that reliable mRNA and protein expression can be obtained from experimental stroke animals after TTC-staining (Kramer, Dang et al. 2010). However, when we compared mRNA expression from these brains to that obtained from fresh, unstained tissues, it was apparent that TTC processing had led to a skewing of the results that is probably due to degradation of the damaged tissues. Consequently, in all ensuing studies we used only fresh, snap-frozen tissues for RT-PCR processing. When only the results from fresh tissues were considered, c-src expression in MPAP-Src treated mice was 22%

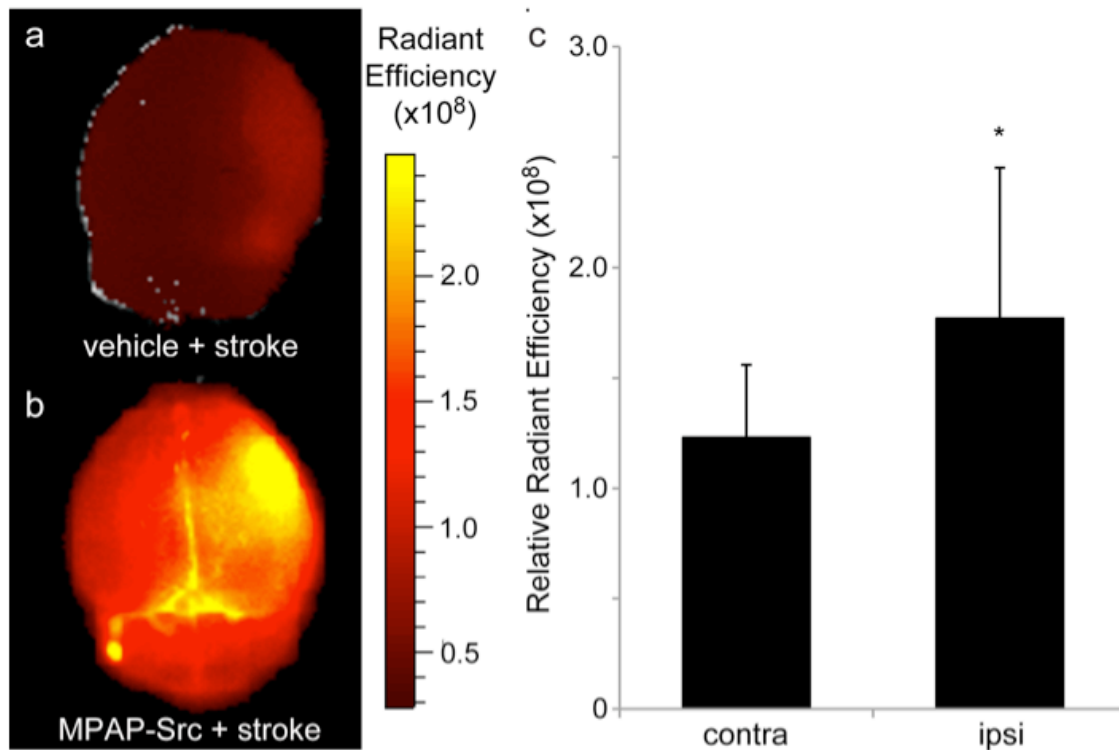


Figure 2.11. Fluorescence imaging of MPAP probe pre-stroke treatment. MPAP-Src (or MPAP-Ctrl) probes were administered 48 and 24 hours prior to 60-minute stroke induction. Imaging of brains excised 24 hours after reperfusion reveals high fluorescence in brains treated with MPAP probes (b) relative to vehicle-treated controls (a). Quantification of fluorescence was performed to compare the differences between MPAP probe uptake in the ipsilateral (ipsi), stroke hemisphere and the contralateral (contra) side (c). MPAP probes localized predominantly in the infarcted territory, with significantly more accumulation evident in the ipsilateral than in the contralateral hemisphere (c, n=8, *p=0.036). Fluorescence was calculated using region-of-interest analysis of each brain hemisphere. Results are presented normalized, with the average background fluorescence from vehicle-treated mice for each hemisphere subtracted out. Radiant efficiency: [emission light (photons/sec/cm²/str)]/[excitation light (mW/cm²)]. Error bars denote standard deviations.

lower in the ischemic hemisphere than in MPAP-Ctrl treated mice. These data suggested that MPAP-Src probes may be capable of modulating Src expression when administered before stroke induction. To clarify the effect of MPAP-Src probes, we investigated their effect on several metrics of stroke outcome, including behavioral testing, infarct volume, and edema.

To evaluate whether MPAP-Src pretreatment has any effect on functional outcome after stroke, mice were subjected to behavioral tests 24-hours after ischemia. These tests included an evaluation of neurological score, in which mice were assessed according to the following scale of neurological symptoms: 0 – no behavioral abnormality detected; 1 – bending of the torso to the ipsilateral side when held by tail; 2 – spontaneous turning behavior; 3 – spontaneous circling behavior, 4 - barrel rolling; 5 – no motor activity (Hara, Huang et al. 1996; Zhang, Chopp et al. 1997; Hunter, Hatcher et al. 2000). In these tests, MPAP-Src treated mice appeared the least impaired of all the treatment groups, with an average neurological score of 1.4 ± 1.9 . This score was influenced most by a high number of MPAP-Src mice (60%) with little or no discernible behavioral abnormalities (neurological score ≤ 1). MPAP-Ctrl mice had the worst neurological scores (3.6 ± 0.9), with no mouse having a score better than 3 in the testing. An intermediate score was obtained for PP1-treated mice (3.0 ± 0.7). The relatively high neurological score for these mice was surprising given that improvement in neurological symptoms was a key observation in the publication that serves as the motivation for this work (Paul, Zhang et al. 2001). However, statistical analysis failed to show significant differences in neurological score ($p > 0.05$). An assessment of mouse coordination after stroke was also performed using rotarod testing. Mice habituated to walking on a

rotating drum prior to surgery were tested 24 hours after ischemia. On average, all treatment groups averaged an approximately 60 second latency on the drum, with wide variations that failed to meet statistical significance. Functionally, MPAP-Src treatment did not lead to any improvement in stroke outcome relative to other treatments.

We next evaluated the effect of MPAP-Src and control treatments on the formation of an ischemic infarct. For this, excised mouse brains were sectioned in 2-mm slices and subjected to TTC staining. Infarct volumes were extracted from TTC-stained slices by an observer who was blinded to the treatment type to avoid bias. Infarct volumes for MPAP-Src, MPAP-Ctrl and PP1 treated mice are shown in Figure 2.12. Infarct volume was the smallest in mice treated with the Src inhibitor PP1, the positive control with known neuroprotective properties. Infarcts in these mice were 37.6% smaller than those of mice treated with non-targeting MPAP-Ctrl probes. MPAP-Src treated mice also had reduced infarct volumes compared to MPAP-Ctrl treated mice, averaging 81.1% of infarct volume for control mice. These results show a tendency towards reduction in infarct size for mice treated with MPAP-Src, though these reductions were not statistically significant. One mechanism for Src-related tissue damage is its tendency to increase vascular permeability and consequently, brain edema (Paul, Zhang et al. 2001). We calculated cerebral edema, as measured by hemispheric enlargement, in our treated mice and found that PP1-treated mice have the lowest edema values ($17.0 \pm 9.0\%$), followed by MPAP-Src ($23.7 \pm 8.0\%$) and MPAP-Ctrl ($27.9 \pm 10.2\%$) treated mice (Figure 2.12). Though not significant, these data suggest that Src inhibition, whether by PP1 or siRNA treatment, tends to reduce the consequences of Src upregulation after stroke.

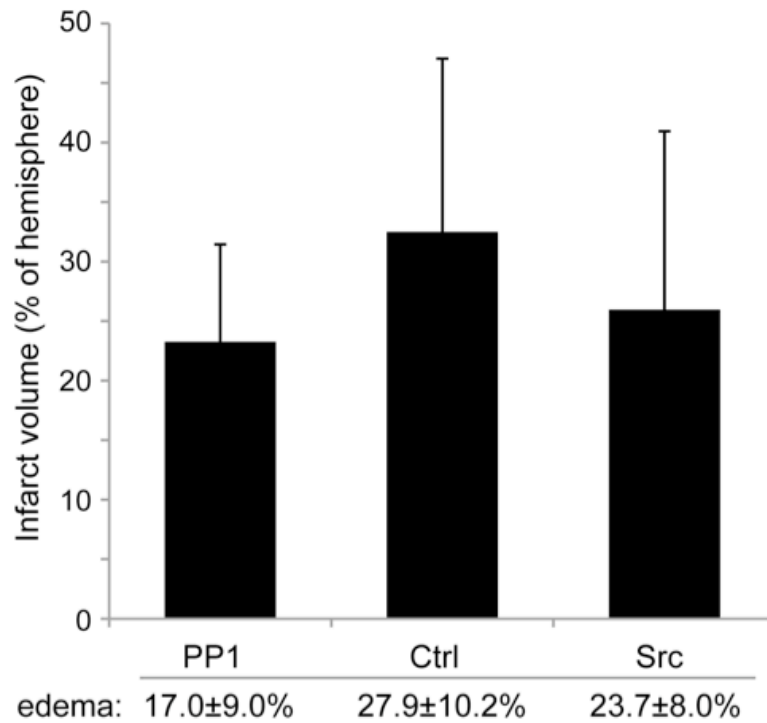


Figure 2.12. Infarct volumes and cerebral edema. TTC-staining of stroke brains revealed reductions in infarct volume in mice treated with Src inhibitor PP1 (n=5) relative to MPAP-Ctrl (Ctrl, n=5) treated mice. MPAP-Src (Src) probe treatment showed less pronounced reductions in infarct volume. The same trend was observed in measurements of cerebral edema, which is known to worsen with increasing Src expression.

2.3.5 The Therapeutic Potential of MPAP-Src Administered Post-Stroke

To this point, administration of MPAP-Src probes had been associated with a small, though insignificant, modulation in stroke outcome as measured by infarct volume, hemispheric edema, and behavioral outcome. It was known from our probe delivery studies (see Figure 2.10d) that injection of MPAP-Src at the time of reperfusion resulted in high accumulations of probe in the ischemic hemisphere. To determine if this alternative probe administration schedule would demonstrate improved probe efficacy in stroke treatment, we tested the effect of MPAP-Src probes when intravenously injected after reperfusion in the 60-minute occlusion mouse model. Mice slated for either MPAP-Src or MPAP-Ctrl treatment were subjected to stroke and injected with probe 15 minutes after reperfusion. Mice were sacrificed 72-hours after reperfusion, and their brains processed for RT-PCR analysis and TTC staining. The results of this analysis are shown in Figure 2.13. As observed with MPAP-Src pretreatment, administration of experimental probe at the time of reperfusion was associated with a minor reduction in infarct volume and a negligible effect on hemispheric edema relative to scrambled controls (Figure 2.13a). Both measures failed to achieve statistical significance. Most notably, expression of mRNA in the ischemic hemisphere remained unaffected by the experimental probe (Figure 2.13b). These results suggest that although MPAP-Src delivery to the site of ischemia appears to be robust under post-stroke treatment conditions, probe fails to access cells susceptible to infarct damage in time to influence Src expression in this model.

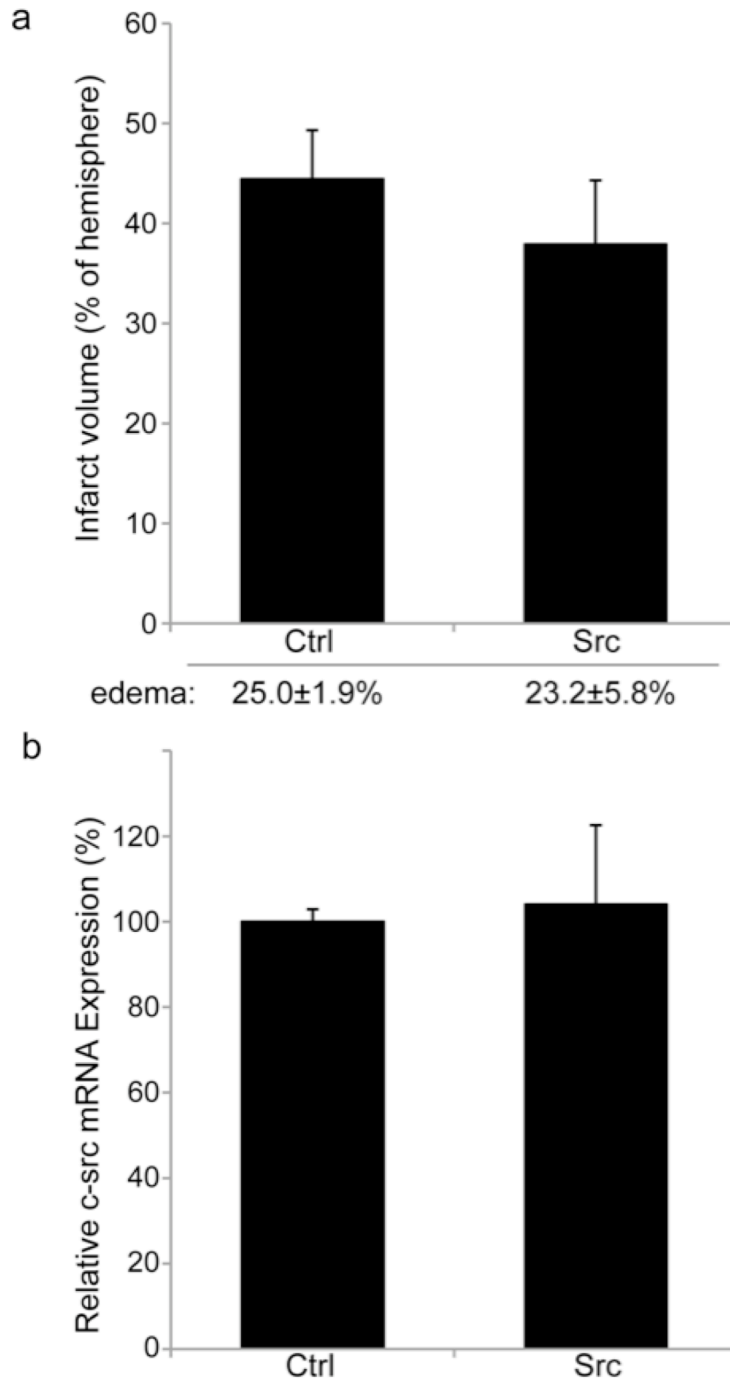


Figure 2.13. MPAP-src post-stroke treatment effects. Mice subjected to 60-minute occlusion were treated with MPAP-Src (Src) or MPAP-Ctrl (Ctrl) at the time of reperfusion. TTC-staining revealed slight, though insignificant reductions in (a) infarct volume and cerebral edema in MPAP-Src treated mice relative to controls. (b) Expression of c-src mRNA was unaffected by experimental probe treatment, suggesting that post-stroke treatment has negligible effects on the damaged brain.

2.3.6 The Efficacy of MPAP-Src Intracerebral Injection in Experimental Stroke

After determining that our intravenous administration models of stroke therapy had limited efficacy regardless whether probe is applied before stroke induction or after reperfusion, we turned to evaluate more direct injection modes. In particular, we analyzed the effects of intracerebral injection of MPAP-Src probe. Intracerebral injection involves performing a craniotomy in anesthetized mice followed by stereotactic injection of a small volume of prepared material in the stroke territory. We began by testing whether injection of MPAP-Src (n=5) in the right cerebral cortex of healthy animals has an effect on Src production relative to MPAP-Ctrl (n=5) treatment. Figure 2.14a compares Src mRNA expression in the right hemispheres of experimental and control mice. We found that MPAP-Src treatment leads to a significant 18.6% reduction in Src expression ($p = 0.027$) in treated mice 24 hours after injection. A similar trend was observed when comparing the right and left hemispheres of MPAP-Src treated mice, such that the hemisphere receiving probe displayed a 24.5% reduction in c-src expression ($p = 0.012$) relative to the untreated side. In contrast, no significant differences between the right and left hemispheres of MPAP-Ctrl treated brains were observed. It is notable that these effects on Src expression were elicited using less than 3% of the siRNA (100 pmol) used per injection in intravenous injection models (3.7 nmol).

We next tested whether this downregulation of *Src* would lead to improved outcome in our stroke model. Mice pretreated with intracerebrally injected MPAP-Src were subjected to 60-minute occlusion, and their brains were evaluated by TTC staining. Despite the significant reductions in *Src* observed previously with intracerebral MPAP-

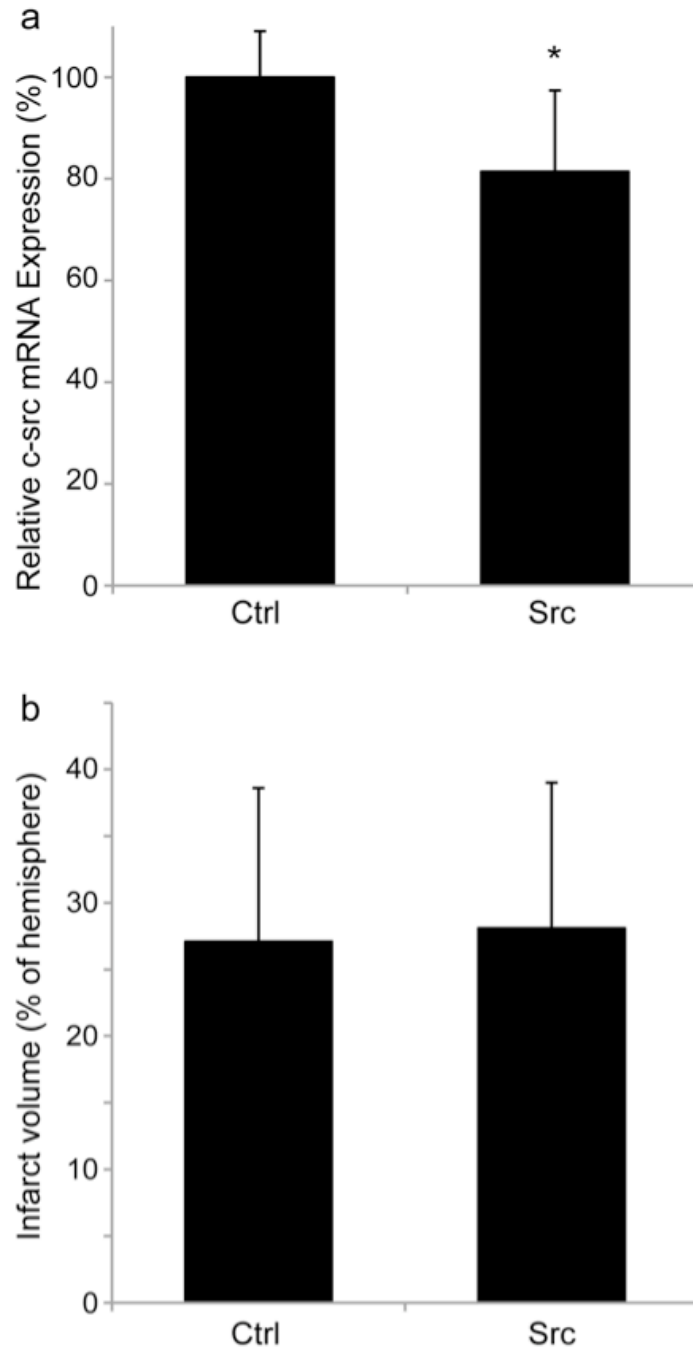


Figure 2.14. Intracerebral MPAP-Src treatment effects. MPAP-Src (100 pmol siRNA: 500 pmol MPAP) was directly injected into the stroke territory of healthy mice. (a) Analysis by rt-PCR revealed significant reductions in c-src mRNA expression approaching 20% (* $p = 0.027$) in mice treated with MPAP-Src (Src, $n=5$) compared to MPAP-Ctrl controls (Ctrl, $n=5$). Additional mice were pre-injected with MPAP-Src or MPAP-Ctrl and subjected to 60-minute occlusion. (b) MPAP-Src pretreatment did not confer protection against stroke damage.

Src treatment, total infarct volume was not reduced in mice treated with our experimental probe (Figure 2.14b). We must conclude from these results that ~20% reduction in Src expression is not sufficient to mitigate stroke damage in our model. We hypothesized that additional knockdown could be elicited if the quantity of injected siRNA were increased. Accordingly, we investigated the concentration dependence of MPAP-Src treatment by injecting healthy mice with different quantities (25, 100 or 400 pmol) of MPAP-Src (right hemisphere) and MPAP-Ctrl (contralateral hemisphere). Figure 2.15 shows *ex vivo* imaging of the injected brain hemispheres (Figure 2.15a) and fluorescence microscopy of Cy5.5-labeled MPAP-Src probe uptake by cells in the brain (Figure 2.15b). We used western blotting to quantify Src protein expression in brain tissues 72-hours after injection (Figure 2.15c-d). In brain hemispheres treated with small quantities of MPAP-Src (i.e., 25 or 100 pmol), protein expression was reduced by only 10% relative to MPAP-Ctrl treated hemispheres (Figure 2.15d). At higher siRNA contents (i.e., 400 pmol) we had difficulty creating a stable suspension of MPAP-siRNA complexes in the low injection volumes mandated by intracerebral injection. This high probe concentration was associated with aggregation of material and precipitation out of solution, rendering it ineffective.

In all, these *in vivo* results demonstrate that we have developed a siRNA delivery platform capable of reducing endogenous mRNA expression in one of the most intractable organs of the body for drug delivery. Intracerebrally injected MPAP-siRNA experimental probes had a significant effect on gene expression, though this effect did not extend to protection against stroke damage when Src was used as a target. However,

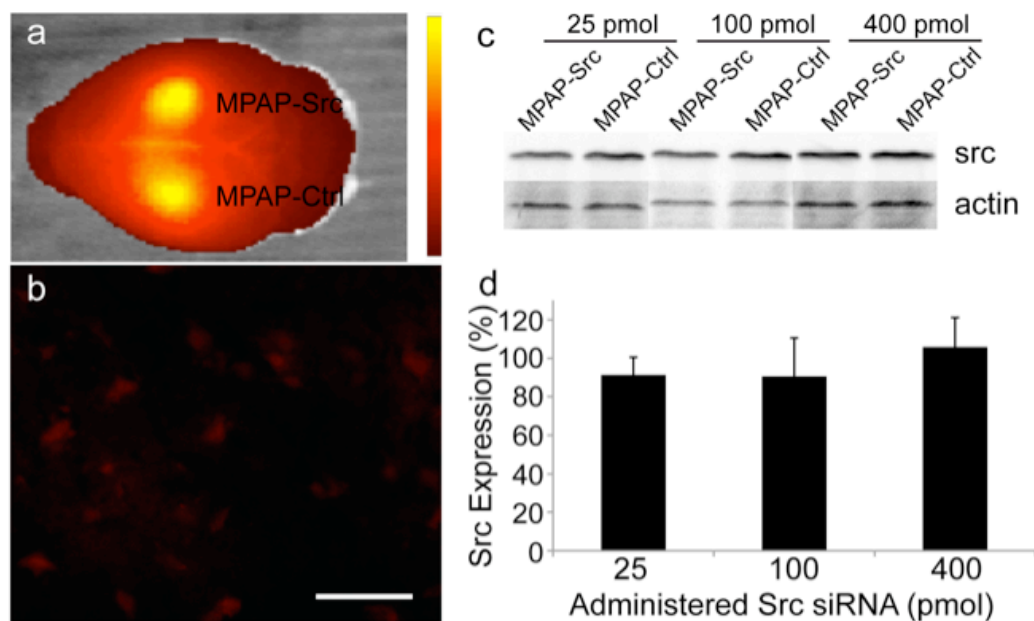


Figure 2.15. Concentration dependence of intracerebral MPAP-Src treatment. (a) Mice were intracerebrally injected in the right and left hemispheres with MPAP-Src or MPAP-Ctrl probes, respectively. Probes consisted of 25, 100, or 400 pmoles of siRNA complexed with a 5-fold excess of MPAP. (b) Cellular uptake of MPAP probes, identified as Cy5.5 signal in frozen tissue sections, was confirmed by histology (Scale bar = 50 μ m). Representative western blots of Src protein expression (with actin loading control) in each injected hemisphere are shown in (c). Reductions of Src expression approaching 10% were observed in mice receiving low concentrations of MPAP probes (d). High concentration probes (i.e., 400 pmol siRNA) were generally unstable and induced no effect in treated mice. Src expression was quantified by normalizing each Src band by the actin loading control. Results are expressed as the average percentage of Src expression in MPAP-Src treated hemispheres relative to expression in MPAP-Ctrl treated hemispheres.

results provide promising evidence that our probes could be therapeutically effective if directed against alternative stroke targets.

2.4 Discussion

In this work we have detailed the characterization, *in vitro* and *in vivo* testing of a fluorescent siRNA imaging probe for application to ischemic stroke. MPAP, an amphipathic membrane translocation peptide derivative capable of crossing the blood-brain barrier, formed probes with siRNA molecules and promoted protection from serum degradation. MPAP differs from traditional cationic cell penetrating peptides in that it contains a 14-carbon saturated fatty acid, or myristoyl lipid chain. Myristoylation is a common modification of proteins in cells that serves as a necessary, though insufficient, part of membrane binding (Resh 1999). Myristoylation promotes weak interactions with the cell membrane, a process that becomes enhanced when associated peptides include basic amino acid residues that can interact with the acidic constituents of the phospholipid bilayer and membrane-associated proteoglycans (Murray, Ben-Tal et al. 1997; Pham, Kircher et al. 2004; Nakase, Hirose et al. 2009). Thus, myristoyl-peptide conjugates demonstrate higher affinities for cells than is observed for either component alone (Pham, Kircher et al. 2004).

In our studies, after confirming that complexation of MPAP and siRNA occurs stably and reproducibly, we investigated whether the resulting probes would be an effective platform for shuttling siRNA into cells. Indeed, we found robust uptake of MPAP-Src complexes by primary cells of the central nervous system, most notably neurons and astrocytes. Live cell imaging indicated that a subset of MPAP-Src complexes was associated with vesicular compartments, suggesting that they had become

internalized via an endocytic pathway. A key consideration is the extent to which the internalized siRNA is able to access molecular mediators of RNA interference. Two steps would be required: first, navigation of siRNA from endosomes to the cytoplasm and second, decoupling of siRNA from MPAP carriers. Live cell imaging showed that while some siRNA signal was associated with endosomal vesicles, diffuse cytoplasmic MPAP-Src signal was also observed, indicating endosomal escape. Several approaches to improve the endosomal escape of molecules have been investigated, most notably the incorporation of fusogenic peptides into the delivery module that change conformation upon endosomal acidification (Wadia, Stan et al. 2004; Kobayashi, Nakase et al. 2009). It is believed that hydrophobic additions to poly-arginine peptides also promote cytosolic translocation through high affinity interactions with and destabilization of vesicular membranes (Takayama, Hirose et al. 2012). The cytoplasmic presence of hydrophobic MPAP that we observed in our studies may be due to this mechanism.

The separation of siRNA from MPAP carriers was less evident by microscopy and therefore was mainly determined through gene expression analysis. Bioactivity of the internalized siRNA was seen in downregulation of endogenous Src mRNA, providing evidence of efficient cytoplasmic delivery of siRNA with our probe. Effects were observed as early as 24 hours after probe exposure in cell types that are notoriously difficult to transfect (Washbourne and McAllister 2002). This indicates that a fraction of siRNA has been freed from MPAP binding, presumably through MPAP degradation. Clearance of the myristoyl acids that comprise MPAP would be routine given their ubiquity in cells, and several studies have reported that polyarginine peptides of six residues or more are cleaved by intracellular serine endoproteases (Cameron, Appel et al.

2000; Kibler, Miyazato et al. 2004). While mRNA knockdown in our studies was not as high as is often observed in immortalized cell lines treated with commercial transfection agents, the levels were not atypical for neurons (Omi, Tokunaga et al. 2004) and were not associated with high toxicity. The query that dominated the remainder of our experiments was whether this degree of knockdown could be achieved in an experimental stroke model and be therapeutically relevant.

Although MPAP delivery to brain tissues within hours of intravenous administration has been established, it was unclear if accumulations of MPAP-siRNA probes were sufficient to modify gene expression in a living system (Pham, Zhao et al. 2005). By selecting a disease model with blood-brain barrier breakdown, we enhanced the delivery of the probe in the MCA territory, the region of the brain in need of neuroprotection after ischemic stroke. Our intravenous stroke models enabled us to test the influence of these probes on brain tissues damaged by ischemia and on normal tissues (represented by the hemisphere contralateral to the ischemic infarct). Our analysis shows that MPAP delivery to brain regions with an intact blood brain barrier has a negligible effect on gene expression. Quantitative RT-PCR analysis of Src mRNA expression in contralateral hemispheres revealed no difference between experimental and control intravenous probe treatment. This shows that any material delivered to the ipsilateral hemisphere during the interval before stroke induction is therapeutically inconsequential. Instead, the amount of probe available for delivery at the time of ischemia becomes crucial. Fluorescent analysis of blood sampled from MPAP-Src injected mice showed that a significant portion of material (i.e., 77.9%) was excreted within six hours of injection, with an additional 31.9% lost by the time of the reperfusion period. Thus, at

the time of reperfusion there is at best 15% of the original injected dose available in the blood for delivery across an impaired blood brain barrier in the pretreatment model. This probe is presumably the source of the ipsilateral hemisphere accumulations observed by imaging in this model. In the 60-minute occlusion model, blood-brain barrier breakdown is estimated to occur within one to three hours after reperfusion (Fujimura, Gasche et al. 1999; Ishikawa, Vowinkel et al. 2005; Chen, Chen et al. 2006). Since Src inhibition has a long therapeutic window after ischemia of six hours (Paul, Zhang et al. 2001), MPAP-Src probes must induce Src protein downregulation over a period of approximately five hours to be therapeutically effective. Mathematical modeling of the kinetics of siRNA delivery indicates that inducing knockdown in this short window is feasible (Bartlett and Davis 2006), particularly since the target cells are non-dividing (i.e., neurons that are not subject to doubling-induced dilution of probe) and the target protein has a short half-life (Harris, Shoji et al. 1999; Bartlett and Davis 2006). In support of this, MPAP-Src probes showed an increased tendency to limit infarct damage in mice in our pretreatment model. This neuroprotection cannot be attributed to a passive effect of the delivery vehicle, since control probes differed from experimental only in the target strand siRNA sequence. However, since the RT-PCR analysis of the ipsilateral hemisphere in this model was inconclusive, it was unclear whether the neuroprotective trends we observed were mediated by siRNA-induced mRNA knockdown. This prompted us to shift to the post-stroke treatment model, in which the interval between blood-brain barrier breakdown and probe injection is minimized. Improved probe delivery was evident by ex vivo imaging in this model relative to the pretreatment model, providing further support for the contention that much of the probe washes out of the

blood by the time of blood-brain barrier breakdown in the latter case. Again we observed a tendency for MPAP-Src to benefit stroke mice. However, this was not accompanied by a notable change in Src mRNA expression. The lack of mRNA knockdown cannot be due to transiency of siRNA's effects, which are predicted to persist for several days in non-dividing cells (Bartlett and Davis 2006). We concluded from this data that intravenously-administered MPAP-Src probe accumulations in the ischemic hemispheres were unable to modulate Src expression rapidly enough to be therapeutically relevant.

We turned to an alternative means of evaluating Src as a target for stroke protection. Stereotactic injection of MPAP-Src probes directly into the cerebral hemisphere was first evaluated in healthy mice with an intact blood brain barrier. Direct injection led to significant knockdown of Src mRNA approaching 20%. This effect was present both when comparing MPAP-Src treated hemispheres to their contralateral counterparts and when comparing the ipsilateral hemispheres of MPAP-Src and MPAP-Ctrl treated mice. Note that the knockdown we detected was obtained by evaluating a fairly large tissue sample (i.e., 2-mm coronal slice of hemisphere), so one can assume even higher gene downregulation in regions in the immediate vicinity of the injection site. Such a concentration gradient of MPAP-Src probe was evident in *ex vivo* optical images.

The effective knockdown of stereotactically-injected probes has important implications. First, it provides proof-of-principle that the MPAP-based siRNA platform we have developed is capable of delivering cargoes in the absence of disease or defect. Consequently, the value of our probes extends beyond the treatment of stroke to any pathology associated with a focal abnormality, particularly since exchanging the targeting

siRNA in MPAP complexes is trivial. In addition, since testing of probe knockdown is performed in healthy mice, the evaluations are not subject to degradation-related errors that may be associated with analysis of infarcted tissues. Finally, our direct injection technique employed nearly two orders of magnitude less material than intravenous injection. Low effective dose of material is particularly important for siRNA drugs, which at present are often prohibitively expensive. Once knockdown was established, we could evaluate whether Src is an effective target for stroke protection. We found that the Src knockdown achieved by our probes had no effect on final stroke volume in a group of mice subjected to 60-minute occlusion. Assuming that higher knockdown might be achievable with more probe, we expanded our study to evaluate increasing concentrations of siRNA. Here we found that higher concentrations of MPAP-Src were associated with aggregation of probe complexes such that they precipitated out of solution. Here we were limited by the practicalities of stereotactic injection, which unlike intravenous injection, requires that the injection volume be constrained to a few microliters to prevent adverse effects to the mouse. Therefore, protein Src expression reductions of no more than 10% were achievable when siRNA concentration was varied. These results prompt us to consider whether our inability to achieve significant neuroprotection with our probes is a result of the choice of Src as a stroke target or insufficient Src downregulation.

Our motivation for selecting protein tyrosine kinase c-Src as a stroke target emerged from an extensive study of Src knockout mice (Paul, Zhang et al. 2001). It was shown that mice without Src expression were protected from cerebral damage after ischemic stroke and retained a higher degree of neurological function than wild-type

mice. It is believed that the detrimental effects of Src in stroke are mainly related to its activation by vascular endothelial growth factor (VEGF). VEGF is a known mediator of vascular permeability, and in the setting of stroke, leads to increases in cerebral edema and tissue damage (van Bruggen, Thibodeaux et al. 1999; Marti, Bernaudin et al. 2000). While inhibition of VEGF has been effective in ameliorating ischemic damage, the benefits of VEGF-induced angiogenesis during the recovery phase of stroke make direct manipulation of VEGF levels undesirable in the long term (Zhang, Zhang et al. 2000). It has been shown that by inhibiting Src, a downstream mediator of VEGF-induced vascular permeability, the damaging effects of ischemia are prevented and presumably, the favorable aspects of VEGF signaling are preserved (Paul, Zhang et al. 2001). Importantly, the chemical inhibitor of Src, PP1, was beneficial when administered up to six hours after reperfusion, a therapeutic window that rivals that of t-PA drugs (1995). Src family tyrosine kinase activation has also been implicated in excitotoxic, reactive oxidative and inflammatory damage after stroke (Nakamura, Hori et al. 1993; Mocsai, Jakus et al. 2000; Liu, Zhang et al. 2001). These studies provide strong evidence that Src is a potent drug target for ischemic stroke and were what first prompted us to evaluate Src with MPAP-based probes.

During the course of our experiments we routinely used Src-inhibitor PP1 as a positive control, administering it 15 minutes after reperfusion at concentrations reported in the literature to reduce infarct volume by nearly 70% (Paul, Zhang et al. 2001). In our experience, PP1 was associated with only small decreases in infarct volume that did not exceed 35% and never achieved statistical significance. Similar modest, though significant, reductions in infarct volume were achieved in a transient ischemia study in

rats using PP2, a Src inhibitor that is structurally-related to PP1 (Lennmyr, Ericsson et al. 2004). The reductions in stroke damage were not accompanied by significant reductions in vascular permeability that have been reported elsewhere (Paul, Zhang et al. 2001). In a study of transient ischemia in hyperglycemic rats, Src inhibition had no protective effect against stroke (Farrokhnia, Roos et al. 2005). Considered together with previous reports, these results provide conflicting evidence of the value of Src as a therapeutic target for stroke protection. Thus, the difficulty we experienced in achieving improvement after stroke, even using potent chemical means, may explain why the reductions in Src expression achieved by direct injection of MPAP-Src probe had little effect.

The difference in the therapeutic potential of chemical Src inhibitors and MPAP-Src probes grows larger when one considers that PP1 and related drugs appear to inactivate members of the Src tyrosine kinase family other than Src (Hanke, Gardner et al. 1996). The additional benefit derived from the non-specific activity of PP1 can be recognized in the study of Src knockout mice (Paul, Zhang et al. 2001). Src knockouts are protected from stroke damage, registering a 50% reduction in infarct volume relative to Src-positive mice. In mice where Fyn (another member of the Src tyrosine kinase family) expression was knocked out, small improvements in infarction tolerance were observed and largely dismissed. However, PP1 inhibition of Src was reported to impart a 20% improvement in infarct volume beyond that observed in Src knockout mice. This suggests that chemical inhibition by PP1 is not restricted to Src and may involve other kinases that are detrimental to stroke, such as Fyn. Therefore, the strategic advantage of RNAi, highly selective downregulation of gene expression in a sequence-specific manner, is lost in this particular context. Even complete siRNA knockdown would fail

to achieve the neuroprotection observed with non-specific chemical inhibition of Src, chemical inhibition that notably failed to result in significant neuroprotection in our studies.

2.4.1. Alternative Therapeutic Targets

In moving forward, it is important to identify targets for stroke that may be more responsive to our MPAP-based imaging probe brain delivery system than Src. Table 2.2 presents a summary of protein targets that could serve as potential alternatives for future investigation. Their selection was informed by the challenges we encountered while investigating Src silencing, as well as published guidelines that aim to improve the design of pre-clinical stroke studies (Fisher, Hanley et al. 2007; Liu, Zhen et al. 2009). Some of the criteria used for the selection of these targets include: validation of the efficacy of the target by multiple research groups; evidence that modest levels of target downregulation are therapeutically effective; effective therapies are target-specific (i.e., no off-target effects); and manipulation of the target leading to neuroprotection in more than one species or ischemic model. Each potential target is considered briefly below.

Calmodulin

One mechanism of ischemic injury involves pathological elevations in intracellular calcium levels consequent to excitatory neurotransmitter stimulation of neurons (Brouns and De Deyn 2009). This is followed by the activation of a diverse collection of degradative calcium-dependent enzymes that first requires the complexation of calcium with one of its main binding proteins, calmodulin (Ghosh and Greenberg 1995). Downregulation of calmodulin using a variety of drugs with different inhibitory mechanisms has resulted in pronounced neuroprotection in several species. For instance,

Table 2.2. Potential Targets for Neuroprotection in Stroke.

Target	Description	Antagonist	Animal Model
Calmodulin	Intracellular calcium-binding protein that participates in the activation of calcium-dependent degradative enzymes (Ghosh and Greenberg 1995).	Trifluoperazine	Transient MCAo (2 hr), Wistar rat (Kuroda, Nakai et al. 1997)
		Tamoxifen	Transient MCAo (2 hr), Sprague-Dawley rat (Kimelberg, Feustel et al. 2000; Osuka, Feustel et al. 2001)
		DY-9760e	Transient MCAo (1 hr), Wistar rat (Sato, Morishima et al. 1999)
			Permanent MCAo, spontaneously hypertensive rats (Takagi, Sato et al. 2001)
			Transient forebrain ischemia, gerbil (Hashiguchi, Kawano et al. 2003)
		Permanent MCAo, cat (Sugimura, Takamori et al. 2005)	
NMDA receptor	Glutamate receptor involved in excitotoxic cell death (Brouns and De Deyn 2009).	NR2C subunit knockout	Permanent MCAo, mouse (Kadotani, Namura et al. 1998)
		SM-31900	Permanent MCAo, spontaneously hypertensive rats (Ohtani, Tanaka et al. 2003)
		Antisense ODN to NR1 subunit	Permanent MCAo, spontaneously hypertensive rats (Wahlestedt, Golanov et al. 1993)
iNOS	Inducible isoform of nitric oxide synthase that promotes the production of NO after ischemia, involved in vasodilation, oxidative damage, and recruitment of inflammatory cells (Parmentier-Batteur, Bohme et al. 2001).	Aminoguanidine	Transient MCAo (2 hr), Sprague-Dawley rat (Iadecola, Zhang et al. 1996)
		iNOS gene knockout	Permanent MCAo, mouse (Iadecola, Zhang et al. 1997; Sugimoto and Iadecola 2002)
		Antisense ODN to iNOS	Transient MCAo (2 hr), Sprague-Dawley rat (Parmentier-Batteur, Bohme et al. 2001)
		1400W	Transient MCAo (2 hr), Sprague-Dawley rat (Parmentier, Bohme et al. 1999)
			Transient MCAo (1.5 hr), Wistar rat (Perez-Asensio, Hurtado et al. 2005)

Table 2.2. (Continued).

ICAM-1	Adhesion molecule upregulated after stroke responsible for the recruitment of inflammatory cells (Soriano, Lipton et al. 1996).	ICAM-1 knockout	Permanent MCAo, mouse (Kitagawa, Matsumoto et al. 1998)
		Antisense ODN to ICAM-1	Transient MCAo (1 hr), spontaneously hypertensive rats (Vemuganti, Dempsey et al. 2004)
		Polydatin	Transient MCAo (2 hr), Sprague-Dawley rat (Cheng, Zhang et al. 2006)
		Rosuvastatin	Transient MCAo (1 hr), insulin resistant mouse (Mayanagi, Katakam et al. 2008)
		Progesterone	Permanent MCAo, Sprague-Dawley rat (Wang, Zhao et al. 2011)
E/P-selectin	Adhesion molecules expressed by activated endothelial cells after ischemia that mediate leukocyte trafficking (Mayadas, Johnson et al. 1993).	P-selectin gene knockout	Transient MCAo (45 min), mouse (Connolly, Winfree et al. 1997)
		Anti-E-selectin antibody	Transient MCAo (45 min), C57BL/6 mouse (Huang, Choudhri et al. 2000)
		CY-1503	Transient MCAo (2 hr), Wistar rat (Zhang, Chopp et al. 1996)
		Anti-E/P-selectin antibody, HuEP5C7	Hemispheric cerebral ischemia (1 hr), baboon (Mocco, Choudhri et al. 2002)
COX-2	Expressed in neurons and upregulated by ischemia and mitogens, COX2 may contribute to ischemic injury through production of reactive oxygen species or inflammatory mediators (del Zoppo, Ginis et al. 2000).	COX2 gene knockout	Permanent MCAo, mouse (Iadecola, Niwa et al. 2001)
		Parecoxib	Transient MCAo (1.5 hr), spontaneously hypertensive rat (Kelsen, Kjaer et al. 2006)
		Valdecoxib	Transient MCAo (1.5 hr), Sprague-Dawley rat (Ahmad, Zhang et al. 2009)
		NS-398	Transient MCAo (2 hr), Sprague-Dawley rat (Hara, Kong et al. 1998)
			Permanent MCAo, C57BL/6 mouse (Sugimoto and Iadecola 2003)

Abbreviations: DY-9760e (3-[2-[4-(3-chloro-2-methylphenyl)-1-piperazinyl]ethyl]-5,6-dimethoxy-1-(4-imidazolylethyl)-1H-indazole dihydrochloride 3.5 hydrate); NMDA, N-methyl-d-aspartic acid; NS-398, N-[2-cyclohexyloxy-4-nitrophenyl]methanesulphonamide; SM-31900, (3S)-7-chloro-3-[2-((1R)-1-carboxyethoxy)-4-aminomethylphenyl]aminocarbonylmethyl-1,3,4,5-tetrahydrobenz[c,d]indole-2-carboxylic acid hydrochloride; ICAM-1, Intercellular Adhesion Molecule 1; COX-2, cyclooxygenase 2.

in a rat model of transient ischemia, trifluoperazine treatment immediately after ischemia reduced infarct size by more than 67% (Kuroda, Nakai et al. 1997). Trifluoperazine is believed to prevent the effects of calcium overload by inducing a conformational change in the calcium-calmodulin complex that blocks its enzyme recognition site (Vandonselaar, Hickie et al. 1994). Treatment with a different calmodulin inhibitor, tamoxifen, has demonstrated remarkable reductions in stroke volume in rats as large as 87% (Kimmelberg, Feustel et al. 2000; Osuka, Feustel et al. 2001). The drug DY-9760e inhibits calmodulin through direct interaction with one of its binding sites and has proven effective against stroke in both transient and permanent rat models (Sato, Morishima et al. 1999; Takagi, Sato et al. 2001). DY-9760e has also been an effective stroke therapy in animals that are closer to humans phylogenetically, including gerbils and cats (Hashiguchi, Kawano et al. 2003; Sugimura, Takamori et al. 2005). The unparalleled reductions in stroke severity observed after calmodulin targeting and its conserved role in the pathogenesis of stroke in multiple species are the main factors that make calmodulin a viable target for testing of MPAP-siRNA probes.

NMDA receptor

Excitotoxic death after ischemia occurs in part when excessive glutamate stimulation of NMDA receptors sets off a cascade of pathological ion fluxes and enzyme activation (Brouns and De Deyn 2009). Therapeutic targeting of NMDA receptor components to inhibit receptor activation has been performed in both mouse and rat ischemia models (Wahlestedt, Golanov et al. 1993; Kadotani, Namura et al. 1998; Ohtani, Tanaka et al. 2003). In one study, transgenic mice lacking the NR2C subunit had infarct volumes that were less than 50% of wild-type controls in a permanent

ischemia model (Kadotani, Namura et al. 1998). Another group investigated the inhibition of NMDA receptors at the binding site of glycine, the coagonist of glutamate, with the drug SM-31900 and achieved infarct reductions in rats ranging from 35-40% after treatment (Ohtani, Tanaka et al. 2003). Another approach targeted the NR1 subunit of the NMDA receptor using antisense oligodeoxynucleotides injected into the cerebral ventricles of rats (Wahlestedt, Golanov et al. 1993). Reduction in stroke lesion volume of 43.5% was achieved. These studies indicate that very selective targeting of NMDA receptors at multiple sites, and most notably, at the mRNA level, can be therapeutically beneficial.

Inducible nitric oxide synthase (NOS)

Inducible nitric oxide synthase (iNOS) is the one of three members of the NOS family that becomes robustly activated in response to pathological stimuli, including ischemia (Forster, Clark et al. 1999). The pathogenic role of iNOS may be related to its production of excessive levels of nitric oxide (NO). NO forms oxidating agent peroxynitrite, which is known to cause tissue injury directly and promote apoptosis (Leist, Fava et al. 1997). As in the case of Src, iNOS knockout mice were protected against ischemic insult in stroke models (Iadecola, Zhang et al. 1997; Sugimoto and Iadecola 2002), though some of these results are in dispute (Pruss, Prass et al. 2008). Mice heterozygous for iNOS exhibit small reductions in ischemic injury, providing evidence of the direct relationship between iNOS gene expression levels and infarct volumes (Zhao, Haensel et al. 2000). Neuroprotection has also been elicited in rats using two partially-selective chemical inhibitors of iNOS, aminoguanidine and 1400W, even when these drugs were administered hours after the ischemic insult (Iadecola, Zhang et

al. 1996; Parmentier, Bohme et al. 1999; Perez-Asensio, Hurtado et al. 2005). More selective reduction of iNOS has been achieved with the use of antisense oligodeoxynucleotide inhibition (Parmentier-Batteur, Bohme et al. 2001). A 39% reduction in iNOS protein expression was associated with 30% smaller infarct volumes in rats and a reduction in sensorimotor deficits. This and other studies provide strong evidence that modest reductions in iNOS may be therapeutically beneficial in stroke.

ICAM-1

ICAM-1 is an adhesion molecule expressed in a variety of central nervous system cells and implicated in ischemic stroke damage through its recruitment of inflammatory leukocytes (Hery, Sebire et al. 1995; Soriano, Lipton et al. 1996). Knockout of the ICAM-1 gene in mice diminishes both transient and permanent ischemic stroke damage (Connolly, Winfree et al. 1996; Kitagawa, Matsumoto et al. 1998). Progesterone, polydatin, and rosuvastatin administration have all been effective in partially inhibiting ICAM-1 expression and infarct volume in rodents (Cheng, Zhang et al. 2006; Mayanagi, Katakam et al. 2008; Wang, Zhao et al. 2011). Reduction in ICAM-1 mRNA expression by only 30% through treatment with ferulic acid led to notable decreases in macrophage activation, oxidative stress and apoptosis in the ischemic penumbra of rats (Cheng, Su et al. 2008). In addition, ICAM-1 specific antisense oligodeoxynucleotide treatment resulted in more than a 50% reduction in infarct volume in rats and was accompanied by improvement in neurological function (Vemuganti, Dempsey et al. 2004). These data indicate that even small decreases of ICAM-1 may be effective in alleviating stroke damage, making ICAM-1 an attractive target for MPAP-siRNA probe testing.

E-selectin and P selectin

E- and P- selectins are glycoproteins that become upregulated in brain endothelial cells upon activation by inflammatory mediators and promote neutrophil influx into ischemic tissues (Poerber, Bevilacqua et al. 1986; Geng, Bevilacqua et al. 1990; Mayadas, Johnson et al. 1993). General selectin blockage through chemical inhibition with the drug CY-1503 led to 42% reduction in infarct volume and neutrophil accumulations in a transient rat model (Zhang, Chopp et al. 1996). Blockage of distinct selectin variants through gene knockout or selectin antibody has likewise been effective against stroke (Connolly, Winfree et al. 1997; Huang, Choudhri et al. 2000). Notably, selectin targeting with antibodies has also been therapeutic in a baboon model of cerebral ischemia (Mocco, Choudhri et al. 2002). These studies provide strong evidence that E- and P-selectins are universal and potent targets for stroke treatment.

COX-2

Like iNOS, COX-2 is involved in the inflammatory response after ischemia and contributes to tissue damage by promoting the production of prostaglandins and reactive oxygen species (del Zoppo, Ginis et al. 2000). COX-2 knockout mice are protected from infarction (Iadecola, Niwa et al. 2001), as are rodents treated with a variety of COX-2 chemical inhibitors (Hara, Kong et al. 1998; Sugimoto and Iadecola 2003; Kelsen, Kjaer et al. 2006; Ahmad, Zhang et al. 2009). Most promising is evidence that COX-2 targeting up to 18 hours after stroke is effective in reducing neurological deficits and infarct volume in treated mice (Sugimoto and Iadecola 2003). This is an extensive time window of action, which is important in a clinical setting where current treatments are only effective when administered within 3 hours of stroke (1995).

In testing our MPAP-siRNA against any of these identified targets, it is important to consider a couple of additional points. First, the targets are involved in different aspects of stroke pathogenesis and are expressed in different types of cells in the central nervous system. Our MPAP-siRNA probes do not possess any targeting moieties that would promote their uptake by one cell type over another. In our previous studies with MPAP, the addition of targeting peptides to MPAP-based probes helped direct their internalization (Medarova, Pham et al. 2007). It would be straightforward to extend this approach to MPAP-siRNA probes to promote targeting of neurons, astrocytes or endothelial cells, depending on the differential expression profiles of therapeutic targets. However, incorporation of targeting peptides changes the uptake dynamics of probes and their bioactivity, which would require recharacterization beginning at the *in vitro* level.

Additionally, in most of our experiments the true effect of probes on infarct volume and neurological function was obscured by the high variability in stroke severity inherent in the intraluminal occlusion model. A good alternative surgical model involves a craniotomy and either permanent or transient occlusion of the MCA as it is directly visualized (Chen, Hsu et al. 1986; Majid, He et al. 2000). This procedure results in smaller and more defined infarcts that would make it easier to recognize small improvements in stroke outcome due to our probes.

In summary, we have demonstrated the proof-of-principle that simple complexation techniques can be employed to produce a bioactive RNAi-based optical imaging probe. We confirmed that MPAP-Src complexes become internalized by cells in the *in vitro* and *in vivo* settings where they lead to statistically-significant reductions in endogenous Src levels in central nervous system cells without adversely affecting cell

viability. The delivery platform provides a flexible method of targeted gene silencing that may prove effective against a variety of targets in experimental stroke studies.

3. Theranostic imaging probes for the treatment of malignant brain tumors.

3.1 Introduction

Glioblastoma multiforme (GBM) is grade IV glioma, the most common and malignant form of brain cancer (Kleihues, Burger et al. 1993). The median survival of GBM patients is only 12-15 months, even with aggressive medical intervention (Sathornsumetee and Rich 2008). Recent clinical trials have demonstrated improved survival when patients receive the chemotherapeutic temozolomide concomitantly with radiotherapy (Stupp, Dietrich et al. 2002; Stupp, Mason et al. 2005; Stupp, Hegi et al. 2009). Combined radiation and temozolomide treatment resulted in a patient survival benefit of 2.5 months relative to standard radiotherapy and an increase in 2-year survival (Stupp, Mason et al. 2005; Mirimanoff, Gorlia et al. 2006). This treatment regimen has since become standard of care for patients with newly diagnosed glioblastoma.

The mechanism of action of temozolomide involves its ability to alkylate DNA in tumor cells. Temozolomide transfers a methyl group to select nitrogen and oxygen atoms of the DNA bases guanine and alanine (Denny, Wheelhouse et al. 1994). Methylation primarily occurs at the N⁷ position of guanine, with additional adducts occurring at the N³ position of alanine and O⁶ position of guanine. It is mainly the latter methylation site that accounts for most of the cytotoxic effects of temozolomide, as it causes errors in the DNA mismatch repair system, accumulation of nicks in cellular DNA, interference with cancer cell cycle progression and, ultimately, cell death (Karran, Macpherson et al. 1993; Liu, Markowitz et al. 1996).

The responsiveness of GBM to the effects of temozolomide has been linked to the activity of the protein MGMT (O6-methylguanine–DNA methyltransferase) in tumor tissue (Pegg 1990; Hegi, Diserens et al. 2004; Hegi, Diserens et al. 2005). MGMT acts by removing methyl adducts from DNA, thereby reversing the cytotoxic actions of alkylating agents such as temozolomide (Kaina, Fritz et al. 1991; Dumenco, Allay et al. 1993). In glioblastoma cell lines in which the MGMT gene promoter is in the methylated, inactivated state, temozolomide has the most pronounced cytotoxic effects (Plowman, Waud et al. 1994). Similarly, epigenetic silencing of the *MGMT* gene is positively correlated with improved clinical outcome after temozolomide treatment in patients with newly diagnosed GBM (Hegi, Diserens et al. 2004; Paz, Yaya-Tur et al. 2004; Weller, Stupp et al. 2010). Furthermore, CD133 positive glioblastoma cancer stem cells, known to be involved in tumor initiation and recurrence, have been shown to express high levels of MGMT that contribute to tumor chemoresistance (Liu, Yuan et al. 2006; Beier, Rohrl et al. 2008). In addition, MGMT expression in recurrent GBMs is higher on average than for primary tumors, which may account for the poor response of these patients to therapy (Christmann, Nagel et al. 2010).

One strategy for enhancing temozolomide toxicity in resistant, MGMT-positive GBMs involves chemical depletion of MGMT in tumors. O6-benzylguanine derivatives have been actively investigated as MGMT inhibitors, but administration of these compounds is associated with hematologic toxicity (Fairbairn, Watson et al. 1995; Chinnasamy, Rafferty et al. 1997; Friedman, Pluda et al. 2000; Ranson, Middleton et al. 2006). An alternative approach is to use RNA interference directed against MGMT to transiently reduce MGMT levels prior to chemotherapy treatment. In one study, human

nasopharyngeal carcinoma cell lines treated with MGMT siRNA displayed enhanced sensitivity to chemotherapeutics (Kuo, Liu et al. 2006). In another study, MGMT knockdown by siRNA in chemoresistant glioma-initiating cells led to improved chemotherapy response (Kato, Natsume et al. 2010). We focused on extending this approach by modifying siRNA to form a nanoparticle-based dual therapeutic and multimodal imaging agent for glioblastoma treatment. We hypothesized that MGMT-directed siRNA would increase the potency of temozolomide treatment in a chemotherapy-resistant mouse model of glioblastoma. Furthermore, incorporating the siRNA onto superparamagnetic iron oxide nanoparticles renders it detectable by magnetic resonance imaging, the technique routinely used to assess glioblastoma tumor response to treatment. We have previously demonstrated that multi-modal superparamagnetic iron oxide nanoparticles can be used as vectors for the delivery siRNA molecules in a variety of cancers (Medarova, Pham et al. 2007; Kumar, Yigit et al. 2010). Nanoparticles functionalized with optical dye, membrane translocation moieties and siRNA successfully accumulated in subcutaneous human colorectal adenocarcinoma tumors following systemic injection (Medarova, Pham et al. 2007). The nanoparticle platform enabled direct noninvasive visualization of delivery by optical and magnetic resonance imaging and promoted reduction in siRNA target gene expression in a therapeutic tumor model. Tumor-specific nanoparticle-based siRNA delivery has also been demonstrated in a breast cancer model using therapeutic nanoparticles modified to target genes implicated in tumor survival *in vivo* (Kumar, Yigit et al. 2010). In addition, the feasibility of nanoparticle delivery to brain cancer has been shown using a functionalized membrane-permeant iron oxide MRI contrast agent that was internalized by tumor cells

in an orthotopic xenograft model of GBM (Kumar, Medarova et al. 2009; Kumar, Medarova et al. 2010). The success of these studies prompted our investigation of nanoparticle siRNA carriers as contrast agents that can modify the MGMT status of human gliomas and enhance sensitivity to temozolomide treatment.

In this work, nanoparticles were synthesized and conjugated to a cocktail of siRNAs specific for human *MGMT* in order to knockdown the *MGMT* gene. Glioma targeting by nanoparticles was enabled through surface modification with fluorescein-labeled chlorotoxin (Lyons, O'Neal et al. 2002). Chlorotoxin has been identified as a peptide with an affinity and selectivity for gliomas that is capable of carrying diverse cargoes to tumors and improving cellular uptake (Veiseh, Sun et al. 2005; Veiseh, Gabikian et al. 2007; Sun, Veiseh et al. 2008). Chlorotoxin was also selected to impart additional therapeutic potential to the nanoparticles given recent evidence that the peptide inhibits tumor proliferation and invasiveness (Deshane, Garner et al. 2003; McFerrin and Sontheimer 2006; Fu, Yin et al. 2007). For correlative microscopy, the chlorotoxin peptide was labeled with fluorescein and magnetic nanoparticles were conjugated to Cy5.5 near infrared optical dye. The superparamagnetic iron oxide core of the nanoparticles served as an MR imaging reporter in these studies. The cellular uptake, bioactivity, and the synergy between temozolomide and the theranostic probe were evaluated *in vitro* in cell lines with different MGMT expression levels. Our results demonstrate robust uptake of nanoparticles in cells that is detectable by optical and magnetic resonance imaging. Uptake of nanoparticles bearing MGMT-specific siRNA was associated with significant decreases in *MGMT* gene expression detected at the mRNA and protein levels and reduced MGMT activity. Furthermore, pretreatment of

MGMT-expressing tumor cells with nanoparticles bearing siRNA to MGMT was shown to improve the cytotoxic effects of temozolomide. Results also indicated that chlorotoxin alone is effective in improving the cytotoxicity of temozolomide. In vitro studies were followed by the investigation of nanoparticles in an orthotopic brain tumor mouse model. Mice bearing TMZ-resistant glioblastomas were subjected to intravenous or intratumoral nanoparticle treatment. As with in vitro studies, we found that MGMT siRNA nanoparticles effectively modulated MGMT expression and activity in tumor cells while reducing tumor volume. We also found that the chlorotoxin moiety reduces tumor size by a mechanism that is independent of MGMT expression. Our results demonstrate that siRNA delivery by nanoparticles, in combination with chlorotoxin targeting, is capable of modulating tumor response to chemotherapy in an animal model of glioblastoma.

3.2 Experimental Procedures

3.2.1 Theranostic Probe Synthesis

Dextran-coated superparamagnetic iron oxide nanoparticles were synthesized according to the procedure described previously (Moore, Medarova et al. 2004). The complete synthesis is illustrated schematically in Figure 3.1. The addition of functional groups was enabled by amine-derivatization of nanoparticles (**1**, NP-NH₂) through modification with epichlorohydrin and ammonia. Nanoparticles were labeled with Cy5.5 optical dye by reacting NP-NH₂ (120 mM, 14.4 mg Fe) with Cy5.5-NHS ester (1 mg, 1.40 mmole, 11.7 eq, GE Healthcare) in DMSO overnight at 4°C. The resulting Cy5.5-conjugated nanoparticles (**2**, Cy5.5-NP) were purified by size exclusion (SE) column. The attachment of chlorotoxin to nanoparticles was achieved by first incubating nanoparticle **2** with an excess of succinimidyl 3-(2-pyridyldithio)propionate (SPDP, 250

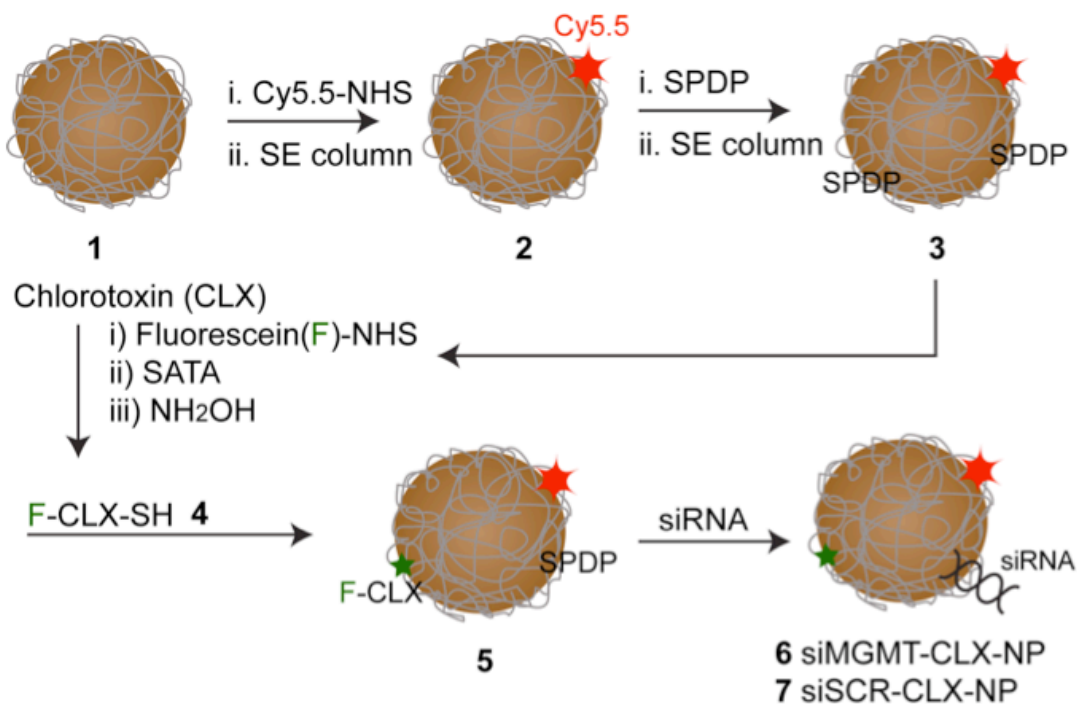


Figure 3.1. Scheme for the preparation of multifunctional nanoparticle probes. Dextran-coated superparamagnetic iron oxide nanoparticles (**1**) were labeled with Cy5.5 dye (**2**) and then modified with SPDP crosslinker (**3**) for attachment of functional groups. Chlorotoxin (CLX) tumor-targeting peptide was labeled with fluorescein dye (**4**) and conjugated to nanoparticles (**5**). The nanoparticles were then conjugated to MGMT-specific siRNA for gene silencing (**6**). Control nanoparticles bearing scrambled siRNA (**7**) served as a control.

eq) for 4 hours at 4°C to generate Cy5.5-NP-SPDP (**3**) followed by purification by size exclusion column. Chlorotoxin (CLX, Alamone) was labeled with Fluorescein-NHS ester (Thermo Scientific) and conjugated with N-succinimidyl S-acetylthioacetate (SATA) to generate Fluorescein-CLX-NH (**4**). The CLX conjugate was treated with hydroxylamine to deprotect the thiol group and enable conjugation with SPDP on nanoparticle **3** upon mixing to form Cy5.5-CLX-NP (**5**).

A cocktail of thiol-modified siRNA targeting sequences for MGMT (siMGMT) manufactured by Dharmacon (Thermo Fisher Scientific) were selected for conjugation to nanoparticles. The siRNA was treated with tris(2-carboxyethyl)phosphine (TCEP) to reduce their disulfide bonds prior to conjugation. A total of 50 nmol of Cy5.5-CLX-NP (**5**) were conjugated with siMGMT (400 nmol) to generate siMGMT-CLX-NP (**6**). Control nanoparticles were synthesized by attaching scrambled non-targeting siRNAs using the same procedure to form siSCR-CLX-NP (**7**).

3.2.2 Characterization of siMGMT-CLX-NP Probes

The number of functional groups per nanoparticle was evaluated as follows. The number of Cy5.5 molecules per nanoparticle was quantified by UV absorption at 683 nm ($\epsilon = 250,000$). The number of CLX moieties was quantified by Pierce BCA assay kit (Thermo Scientific) and confirmed by quantification of the CLX fluorescein label at 518 nm ($\epsilon = 70,000$) by UV spectrometer. The amount of siRNA on nanoparticles was determined by semi-quantitative agarose gel electrophoresis. This entailed loading siMGMT-CLX-NPs or siSCR-CLX-NPs on magnetic activated cell sorting (MACS) columns and washing in a magnetic field with nuclease-free water to remove unconjugated free siRNA. The column was removed from the magnet and the samples

were collected by eluting the column with nuclease-free water. The probes were treated with TCEP for 30 minutes to promote the release of siRNA from the nanoparticles. The TCEP-treated probes, untreated probes and siRNA standard (50, 100, 150, 200 pmol) reference solutions were loaded onto a 2% agarose gel in Tris borate-EDTA buffer (Invitrogen, Carlsbad, CA) and separated by electrophoresis at 120 V for 90 minutes. After electrophoresis, the siRNA residing in the gel was stained with 0.5 mg/ml ethidium bromide for 30 minutes and visualized using a Molecular Imager FX scanner (BioRad Laboratories, Hercules, CA). The intensities of siRNA bands in the image were quantified using ImageJ, version 1.45i software (NIH). The amount of siRNA released from nanoparticles following TCEP treatment was determined relative to reference siRNA solutions.

Iron content of nanoparticles was determined by measuring the absorbance at 540 nm using the Total Iron Reagent Set (Pointe Scientific, Canton, MI). Each experiment was performed in triplicate. The relaxivities of nanoparticles were measured using a 20 MHz NMR spectrometer (miniSpec, Bruker). Nanoparticle size was measured with a Malvern Zetasizer Nano Series ZS instrument.

3.2.3 In vitro siMGMT-CLX-NP Probe Uptake

Internalization of siMGMT-CLX-NPs and control probes was assessed in human glioma cell lines. T98G and U87MG cell lines that express high and negligible quantities of MGMT, respectively, were purchased from ATCC and propagated according to the supplier's recommendations. Cells were seeded at a density of 1×10^5 cells per well in 12-well plates. Twenty-four hours after plating, siMGMT-CLX-NPs, siSCR-CLX-NPs, or unmodified Cy5.5-labeled NPs (Cy5.5-NPs) were added to cells at concentrations

ranging from 10 to 150 $\mu\text{g Fe/ml}$. Cells were incubated with nanoparticles for 48 hours at 37°C in a humidified 6% CO_2 atmosphere. Media was removed and after washing with Hanks' Balanced Salt Solution (HBSS), cells were dissolved in 1 ml of 6-N HCl with 3% hydrogen peroxide. Iron content of the solutions was determined by Total Iron Reagent Set (Pointe Scientific) iron assay. A subset of treated cells were washed, collected by trypsinization, and counted for the purpose of normalization. Each experiment was performed in triplicate and the results were expressed as picograms of iron per cell. Cellular distribution of the nanoparticles was evaluated by fluorescence microscopy. T98G cells plated in 12-well plates on coverslips and treated for 48 hours with siMGMT-CLX-NPs or Cy5.5-NPs were fixed in 4% paraformaldehyde for five minutes and washed thoroughly with PBS. Coverslips were mounted on slides with Vectashield Mounting Media containing DAPI for nuclear staining. Intracellular Cy5.5, fluorescein and DAPI fluorescence were detected using a Nikon Eclipse 50i microscope.

3.2.4 Optical/MR Imaging of Cellular Phantoms

T98G and U87MG cells were incubated with probes for 48 hours, harvested, and pelleted in 0.2 mL PCR tubes to form cell phantoms. Probe uptake by cells was evaluated by optical (IVIS Spectrum, Caliper Life Sciences) and magnetic resonance imaging (9.4T Bruker horizontal bore scanner equipped with ParaVision 5.1 software). The MRI protocol consisted of T2-weighted spin echo (SE) pulse sequences with SE repetition time/echo time = 3,000/[8, 16, 24, 32, 40, 48, 56, 64]; FOV = 32 x 32 mm; matrix size = 128 x 128 pixels; slice thickness = 0.5 mm; and in-plane resolution = 250 x 250 μm^2 . Image reconstruction and analysis were performed with ImageJ software (NIH). Optical imaging was performed immediately after the MRI session. Imaging of phantoms was

performed using 675-nm excitation and 720-nm emission filters for detection of Cy5.5-labeled probe. The fluorescence imaging settings (i.e., exposure time, 0.5 seconds; F-stop, 2; binning, medium) were kept constant for comparative analysis. Grayscale white-light photographs and epifluorescent images were acquired and superimposed. The images were reconstructed using the Living Image software version 3.1 (Caliper Life Sciences).

3.2.5 Real Time Quantitative RT-PCR

The effect of siMGMT-CLX-NP treatment on MGMT expression in cells or brain tumor tissue was evaluated using real-time quantitative RT-PCR (TaqMan). For in vitro studies, T98G cells were seeded at a density of 2×10^4 cells per well in 12-well plates and treated with siMGMT-CLX-NPs (25 or 50 $\mu\text{g Fe/ml}$, corresponding to 238 and 475 pmol/ml siRNA, respectively), siSCR-CLX-NPs (50 $\mu\text{g Fe/ml}$, 475 pmol siRNA) or Cy5.5-NPs (50 $\mu\text{g Fe/ml}$). After 24 hours of incubation, cells were harvested and total RNA was extracted with an RNeasy Mini Kit (Qiagen) according to the manufacturer's protocol. For in vivo studies, treated brain tumors were removed and flash frozen. RNA was extracted from tissues with an RNeasy Mini Kit according to the manufacturer's protocol.

TaqMan analysis was performed using an ABI Prism 7700 sequence detection system (PE Applied Biosystems). The sequences of primers and probe used for amplification are as listed: MGMT forward primer, 5'-CTGGCTGAATGCCTACTTCC-3'; MGMT reverse primer, 5'-CAACCTTCAGCAGCTTCCAT-3'; and MGMT probe, 5'-TGTCTGGTGAACGACTCTT-GCTGGA-3'. Eukaryotic 18S rRNA served as an internal control. Statistical analysis was performed using one-way analysis of variance

followed by the Holm multiple comparisons posttest.

3.2.6 Western Blot Analysis

Western blot analysis was performed on treated cells and brain tumor extracts. For cell studies, T98G cells were seeded in 12-well plates (1×10^5 cells/well) and cultured for 24 hrs. Cells were incubated with siMGMT-CLX-NPs (25 or 50 $\mu\text{g Fe/ml}$), siSCR-CLX-NPs (50 $\mu\text{g Fe/ml}$) or Cy5.5-NPs (50 $\mu\text{g Fe/ml}$) for 48 hours and then washed thrice with HBSS. Cells were harvested by trypsinization. For animal studies, treated tumors were resected and snap frozen. Cells or tissues were treated with lysis buffer (RIPA buffer with 100 mM EDTA, 100 mM PMSF and protease inhibitor cocktail) and centrifuged (12,000 rpm for 10 min). The supernatant was collected and the amount of protein per sample was quantified by Pierce BCA assay (Thermo Scientific). Denatured protein extracts (40 mg) were loaded onto a polyacrylamide gel and subjected to SDS-PAGE. After electrophoresis, the protein was transferred onto a polyvinylidene fluoride membrane. The membrane was blocked in 5% non-fat milk for 1 hour followed by overnight incubation with the mouse monoclonal antibody to MGMT (MT3.1, 1:500 dilution; abcam) at 4°C. After washing, 1-hour incubation with secondary antibody (HRP-conjugated goat anti-mouse IgG (H+L), 1:2,000 dilution; Invitrogen) was performed at room temperature. MGMT protein was detected following membrane incubation with Amersham's ECL Plus Western Blot Detection system. MGMT protein levels were normalized by reference β -actin protein levels that were detected using the same protocol.

3.2.7 MGMT Activity Assay

MGMT activity in cells after nanoparticle treatment was assessed according to a

published O⁶-alkylguanine-DNA alkyltransferase assay procedure (Watson and Margison 1999). Assay substrate DNA was prepared by purifying 40 mg of calf thymus DNA (CT-DNA, Sigma-Aldrich) with proteinase K (100 mg, Sigma-Aldrich). The DNA was methylated with the use of 5 mCi tritylmethyl nitrosourea ([³H]-MNU, Moravek Biochemicals and Radiochemicals, Inc.) in 0.02M Ammediol (Sigma-Aldrich), pH 10. After overnight stirring, [³H-methyl]-labeled calf thymus DNA (3[H]-CT-DNA) was precipitated by adding 3M sodium acetate and cold ethanol. Protein extracts were prepared from T98G and U87MG cells after 48-hour incubation with siMGMT-CLX-NPs, siSCR-CLX-NPs or Cy5.5-NPs (50 µg Fe/ml each). The cells were harvested and homogenized by sonication in buffer (Tris-HCl, 20 mM, pH 8.5, EDTA, 1 mM; β-mercaptoethanol, 1 mM; 5% glycerol and the protease inhibitor phenylmethylsulphonyl fluoride, 0.1 mM). The cell lysate was centrifuged at 10,000 rpm for 10 min at 4°C, and the protein concentration of the supernatant was determined by Pierce BCA assay (Thermo Scientific). Substrate 3[H]-CT-DNA (200 counts per minute (cpm)/ml, 100 ml) was incubated with the extract (50 mg protein) and concentrated with bovine serum albumin (BSA, 150 ml) solution for 90 min at 37°C. The DNA substrate was then hydrolysed with the addition of BSA (100 µL), 4M perchloric acid (PCA, 100 µL), 1M PCA (2 mL) and 50 minutes of heating at 75°C. After centrifugation, the protein pellet was washed with 4 ml PCA, dispersed in 300 mL of 10 mM NaOH and then in 3 ml of Ecoscint solution. Radioactivity was determined with a liquid scintillation counter. Data are expressed as [fmol radioactivity transferred from 3H-labeled DNA to protein]/[mg of protein added]. Statistical analysis included one-way analysis of variance followed by the Holm multiple comparisons posttest.

3.2.8 Synergistic Effect of siRNA and Temozolomide Treatment.

The effect of MGMT knockdown by siMGMT-CLX-NPs on temozolomide resistance was evaluated through combination treatment of cells with nanoparticles and chemotherapeutic. A total of 1×10^5 cells were seeded in 12-well plates and allowed to adhere for 24 hrs. Each probe (siMGMT-CLX-NPs, siSCR-CLX-NPs and Cy5.5-NPs) was applied to cells in concentrations of 50 μg Fe/ml for 48 hrs. Chemotherapeutic temozolomide (TMZ, Sigma-Aldrich) was added to the cells in varying concentrations (100, 300 and 650 μM) and incubated for four hours. Cells were trypsinized and the number of surviving cells was counted. Viability was calculated relative to the mean number of cells in control wells treated with PBS.

3.2.9 Establishment of Flank Tumor Xenografts

Six-week-old athymic nude mice (nu/nu, COX-7) were selected for in vivo T98G xenograft studies. Several investigators have reported poor tumorigenicity of T98G cells following subcutaneous and orthotopic inoculation in mice (Stein 1979; Potapova, Fakhrai et al. 1996; Rubenstein, Shaw et al. 1999). The reduced tendency to form *de novo* tumors has been linked to low expression of peripheral-type benzodiazepine receptors (PBRs) by T98G cells and correlative decrease in anchorage independent growth (Veenman, Levin et al. 2004). To overcome this limitation, we seeded T98G cells in the presence of Matrigel (BD Biosciences) supportive basement membrane matrix (Rubenstein, Shaw et al. 1999). Mice were inoculated in the flank with 5×10^6 T98G cells suspended in a 1:1 mixture of Minimum Essential Medium (Cellgro) and Matrigel. Substantial tumor mass measuring approximately 8 mm in diameter was evident within three months. The xenograft was surgically resected under aseptic

conditions and sectioned into 2x2x2-mm tumor fragments. Each fragment was dipped in Matrigel and subcutaneously implanted into the flank of a recipient mouse for propagation. Flank tumors were serially passaged in vivo from donor to recipient nude mouse using this procedure at the point that xenografts measured 1 cm in diameter, or approximately 4-5 weeks following implantation.

3.2.10 Establishment of Orthotopic Tumor Xenografts

For intracranial tumor implantation, short-term explant cultures were derived from established T98G flank tumors using a modification of a published procedure (Carlson, Pokorny et al. 2011). Tumors of approximately 1 cm in diameter were surgically removed from anesthetized donor mice using sterilized instruments and under aseptic conditions. The excised tumor was placed in a petri dish containing DMEM supplemented with 2.5% FBS and 1% pen-strep and minced using a sterile scalpel. The tumor was further disrupted by triturating through a small-bore pipet tip to form a single cell suspension. The cell suspension was distributed among four 75-cm² cell culture flasks that had been coated for 30 minutes with 10% Matrigel in supplemented DMEM. Cells were allowed to adhere to culture flasks for 1-7 days, at which point culture medium was replaced with DMEM supplemented with 10% FBS and 1% pen-strep. Cells were propagated and expanded to additional flasks through trypsinization with 0.05% Trypsin/0.53 mM EDTA. Large tumor aggregates were removed by filtering cell suspensions through a 70 µm nylon mesh strainer. After 10-20 days in culture, tumor cells (~80-90% confluent) were prepared for intracranial implantation. Cells were trypsinized, centrifuged (1000 rpm, 5 minutes), resuspended in sterile PBS at 100,000 cells/µl and placed on ice to await injection.

Five- to six-week-old athymic nude mice were anesthetized with 2.0-2.5% isoflurane in 30%/70% oxygen/nitrous oxide gas vehicle after which anesthesia was maintained at 1.0-1.5% isoflurane. Mice were transferred and secured to a small animal stereotactic instrument (Kopf) with a Quintessential Stereotactic Injector (Stoelting Company) for controlled microinjection. A 5-mm incision was made in the scalp and the skull surface wiped clean of loose tissues until the landmark bregma was clearly visible. A hole was drilled through the skull over the right hemisphere, 2.0-mm lateral and 1.0-mm anterior to bregma, using a high speed micro drill with 0.7-mm steel burrs (Fine Science Tools). A 701RN 10- μ l syringe with a 26-gauge needle attachment (Hamilton Company) was loaded with 3 μ l of tumor cell suspension. The needle was advanced through the drill hole 3 mm into the brain, then retracted 0.5 mm to form a small pocket for cells. Cells were injected at a rate of 1 μ l/minute. After injection was complete, the needle was left undisturbed for 1 minute before being removed. The drill hole was patched with bone wax (Fine Science Tools) and the skin incision closed with 5-0 silk suture thread (Ethilon). Postoperative buprenorphine (0.05 mg/kg subcutaneous, Bedford Labs) was administered every 12 hours or as needed. Tumor growth was monitored weekly by magnetic resonance imaging. In a group of comparative experiments, orthotopic brain tumors were seeded in 6-week old NOD SCID mice (Charles River Laboratories) with T98G cells provided as a gift from Dr. Nava Almog of Tufts University (Naumov, Bender et al. 2006).

3.2.11 In vivo Magnetic Resonance Imaging

MR imaging was performed using a Bruker 9.4T horizontal bore magnet (Magnex Scientific) with gradient insert and operated using ParaVision 5.1 software. Mice were

placed in a birdcage radiofrequency coil. Coronal T2-weighted spin echo (SE) pulse sequences were used to acquire images for the monitoring of brain tumor size. T2 maps were acquired for quantitative analysis of iron oxide probe accumulations. The following imaging parameters were used: SE TR/TE = 2500/[10, 20, 30, 40, 50, 60, 70, 80, 90, 100, 110, 120, 130, 140, 150]; FOV = 1.91 x 1.92 cm², matrix size = 128 x 128; slice thickness 0.5 mm. Tumor volumes were quantified using ImageJ software (NIH). The tumor ROI was identified in each MR image and pixel area was calculated. The pixel area of each slice was converted to slice tumor volume (mm³) by multiplying pixel area by the in-plane resolution of the T2-weighted images and slice thickness. Total tumor volume was obtained by summing the slice tumor volumes from consecutive slices. T2 maps were calculated using Marevisi 3.5 software (Institute for Biodiagnostics, National Research Council, Canada).

3.2.12 Nanoparticle/Chemotherapy Treatment

Intravenous route of probe administration

As soon as tumors became viable on MRI (~ 2-4 weeks post-injection), mice were subjected to two rounds of nanoparticle and temozolomide treatment. Injection of siMGMT-CLX-NPs (10 mg/kg Fe, 95 nmol/kg siRNA, n=3) or control CLX-NPs (10 mg/kg Fe, n=3) was performed by tail vein injection while mice were anesthetized with 1.5% isofluorane in oxygen gas. One day later, temozolomide was administered intraperitoneally at a concentration of 50 mg/kg. Temozolomide treatment was performed for four consecutive days to complete the first round of treatment. This combination of nanoparticle treatment followed by 5-day TMZ administration was repeated the following week. Periodic T2-weighted MRI was performed to evaluate the

uptake of nanoparticles by tumor cells and tumor growth. After the completion of the second round of treatment, mice were sacrificed and their tissues collected for further analysis.

Intratumoral route of probe administration

As soon as tumors became visible by MRI, intratumoral injection of siMGMT-CLX-NPs (n=6), CLX-NPs (n=5) or PBS vehicle (n=3) was performed in combination with TMZ treatments as follows. On day one of the first week, nanoparticle treatment was initiated. Mice were anesthetized in 2.0-2.5% isoflurane in 30%/70% oxygen/nitrous oxide gas vehicle, and anesthesia was maintained at 1.0-1.5% isoflurane during surgery. An incision was made in the scalp and the drill hole through which tumor cells were originally injected into the brain was identified. Two microliters of siMGMT-CLX-NPs (10.5 μ g Fe, 100 pmol siRNA), CLX-NPs (10.5 μ g Fe), or PBS were injected into the center of the tumor (coordinates measured by MR imaging) using a 701RN 10- μ l syringe with a 26-gauge needle attachment (Hamilton Company) at a rate of 0.125 μ l/minute. After injection was complete, the hole was patched with bone wax (Fine Science Tools) and the skin incision closed with 5-0 silk suture thread (Ethilon). Postoperative buprenorphine (0.05 mg/kg subcutaneous, Bedford Labs) was administered every 12 hours or as needed. Treatment with temozolomide (50 mg/kg/day) was performed by intraperitoneal injections during each of the next 5 consecutive days. Two additional rounds of treatment with nanoparticles and temozolomide were performed using the same procedure, with nanoparticle injections occurring on day one of the second and third weeks of treatment. During the fourth week of treatment, mice were injected with TMZ without any nanoparticle treatment. Periodic T2-weighted MRI was performed to

evaluate the uptake of nanoparticles by tumors and tumor growth. After the completion of the fourth round of treatment, mice were sacrificed and their tissues collected for further analysis.

3.2.13 Histological Staining

Mouse brains containing orthotopic tumors were embedded in Tissue-tek Optical Cutting Temperature (O.C.T) compound (Sakura Finetek USA) and frozen in dry ice. Frozen tissue sections (10- μ m thickness) were cut using a Leica CM-3050S cryostat and placed on glass slides. Sequential slices of each brain were stained using Prussian blue (for iron), hematoxylin and eosin (for tumor morphology), and mounted with DAPI for fluorescence microscopy.

Prussian Blue Iron Staining

For Prussian Blue staining, slides were equilibrated at room temperature and fixed in 4% paraformaldehyde for 5 minutes. Following washing with PBS, the slides were immersed in Perl's solution (5% potassium ferrocyanide (ACROS Organics) and 5% HCl (Aldrich)) for 30 minutes at room temperature. The slides were rinsed with water and counterstained with Nuclear Fast Red stain (Sigma-Aldrich) for 2 minutes. After a wash in water, the slides were incubated in consecutive 50%, 75%, 95%, and 100% ethanol solutions for 1 minute each followed by two 2-minute incubations in xylene. After air-drying the coverslips were mounted in Permount mounting medium (Fisher Scientific).

Hematoxylin and Eosin (H&E) Staining

Flank and orthotopic tumor xenograft growth was confirmed histologically by hematoxylin and eosin staining. Fresh mouse brain tissue or subcutaneous tumor was embedded in Tissue-tek Optical Cutting Temperature (O.C.T) compound (Sakura Finetek

USA) and frozen in dry ice. Frozen tissue sections (10- μ m thickness) were cut using a Leica CM-3050S cryostat and mounted on glass slides. For staining, sections were fixed in acetone (-80°C) for 15 minutes. Following washes in PBS, slides were incubated in hematoxylin for one minute, then washed in water before incubating in eosin (Fisher Scientific) for an additional minute. This was followed by one-minute incubations in consecutive 50%, 75%, 95%, and 100% ethanol solutions to dehydrate the tissues. Five minute incubation in xylene was performed to remove any additional O.C.T. compound. Slides were air-dried and mounted using Permount mounting medium (Fisher Scientific).

Fluorescence microscopy

To enable the visualization of nanoparticle uptake by fluorescence microscopy, tissue slices were fixed in 4% paraformaldehyde for five minutes and washed thoroughly with PBS. Coverslips were mounted on slides with Vectashield Mounting Media containing DAPI for nuclear staining. Microscopy was performed using a Nikon Eclipse 50i microscope.

To evaluate the vascularity of tumors, frozen tissue sections of brains bearing U87MG or T98G tumors were fixed in 4% paraformaldehyde, blocked with bovine serum albumin, and incubated with rat antibody to mouse CD34 primary antibody (1:100, Abcam). This was followed by incubation with biotinylated anti-rat secondary antibody (1:100, Vector Labs) and streptavidin-FITC conjugate (1:1000, Invitrogen). Coverslips were mounted on slides with Vectashield Mounting Media containing DAPI for nuclear staining. Microscopy was performed using a Nikon Eclipse 50i microscope.

3.3 Results

3.3.1 Characterization of siMGMT-CLX-NP Probes

For synthesis of our theranostic probes we used dextran-coated superparamagnetic iron oxide nanoparticles. Iron oxide nanoparticles are contrast agents that reduce the T2 relaxation time of associated tissues and promote signal intensity loss in T2-weighted magnetic resonance images. The nanoparticles were modified with Cy5.5 dye to enable correlative fluorescence microscopy. Nanoparticles were further modified with fluorescein-labeled chlorotoxin peptide for glioma tumor targeting and growth inhibition, while MGMT-specific siRNAs were conjugated to the nanoparticles for gene silencing to increase tumor responsiveness to the chemotherapeutic temozolomide. We found the following ratio of functional groups/nanoparticle: Cy5.5/CLX/siRNA = 2.7/2.9/1 (Figure 3.2a). The relaxivities of the probe were measured as $R1 = 18.85 \text{ mM}^{-1}\text{sec}^{-1}$ and $R2 = 100.94 \text{ mM}^{-1}\text{sec}^{-1}$ (Figure 2b). The particle size of Cy5.5-CLX-NPs was $30.7 \pm 3.2 \text{ nm}$ and the size of siMGMT-CLX-NPs after the addition of siRNA was $37.3 \pm 7.3 \text{ nm}$.

3.3.2 *In vitro* siMGMT-CLX-NP Probe Uptake

Two human glioblastoma cell lines were selected to test probe cellular uptake and bioactivity *in vitro*. T98G cells were selected as an MGMT-expressing cell line with temozolomide resistance. The MGMT negative, temozolomide-sensitive U87MG cell line was chosen for control studies. Probe internalization was investigated through incubation of T98G and U87MG with tumor-targeted siMGMT-CLX-NPs or unmodified Cy5.5-NPs at several probe concentrations ($10 \sim 150 \mu\text{g Fe/ml}$) for 48 hours. The CLX targeting peptide promoted significant nanoparticle internalization by both T98G and

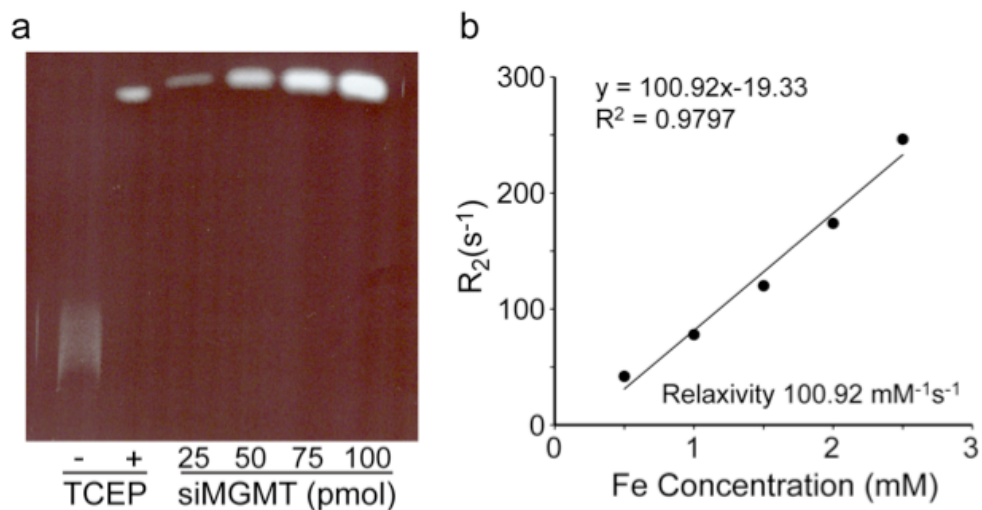


Figure 3.2. The siRNA content and R_2 relaxivity of siMGMT-CLX-NP probes. a) The number of siRNA molecules per nanoparticle was determined by semi-quantitative agarose gel electrophoresis. TCEP was used to cleave MGMT siRNA from nanoparticles and enable its migration into the agarose gel. The amount of free siRNA in TCEP-treated samples (+) was determined relative to siRNA standards (25, 50, 75 and 100 pmol). b) Probe relaxivity was determined by measuring T2 parameters as a function of iron concentration using a 20 MHz NMR spectrometer.

U87MG cell lines as shown by iron uptake assay (Figure 3.3). There was a concentration dependent nanoparticle accumulation that plateaued to saturation levels at a concentration of approximately 50 $\mu\text{g Fe/ml}$. Since there was little improvement in cellular nanoparticle uptake above this concentration, all further experiments were performed at 50 $\mu\text{g Fe/ml}$. Iron levels per cell were generally higher in T98G than U87MG cells, which may be a function of differences in cell doubling rates or cell membrane distribution of CLX's target, matrix metalloproteinase-2 (MMP-2), between the two cell lines. In contrast, unmodified nanoparticle treatment resulted in negligible uptake at every probe concentration tested, demonstrating how crucial the presence of CLX is for nanoparticle internalization. Cellular uptake of siMGMT-CLX-NPs was confirmed by fluorescence microscopy. T98G cells incubated with siMGMT-CLX-NPs or control Cy5.5-NPs are shown in Figure 3.4. Co-localization of Cy5.5 and FITC signal indicated the uptake of the probe by the cells. In contrast, virtually no uptake was observed with control probe, confirming the necessity of CLX presence for probe uptake.

Additional verification of nanoparticle uptake was obtained from magnetic resonance imaging of NP-treated cell phantoms. T98G cells treated with siMGMT-CLX-NPs, siSCR-CLX-NPs, or Cy5.5-NPs were trypsinized and pelleted to make cell phantoms. The phantoms were subjected to optical and T2-weighted MR imaging. Optical imaging shows significant uptake of siMGMT-CLX-NPs and siSCR-CLX-NPs by cells relative to Cy5.5-labeled nanoparticles that lack the CLX targeting peptide (Figure 3.5a). Phantom studies also demonstrate that siMGMT-CLX is an effective MR T2 contrast agent. In pellets of the cells treated with siMGMT-CLX-NPs and siSCR-CLX-NPs, the signal intensity in T2-weighted images decreased significantly compared

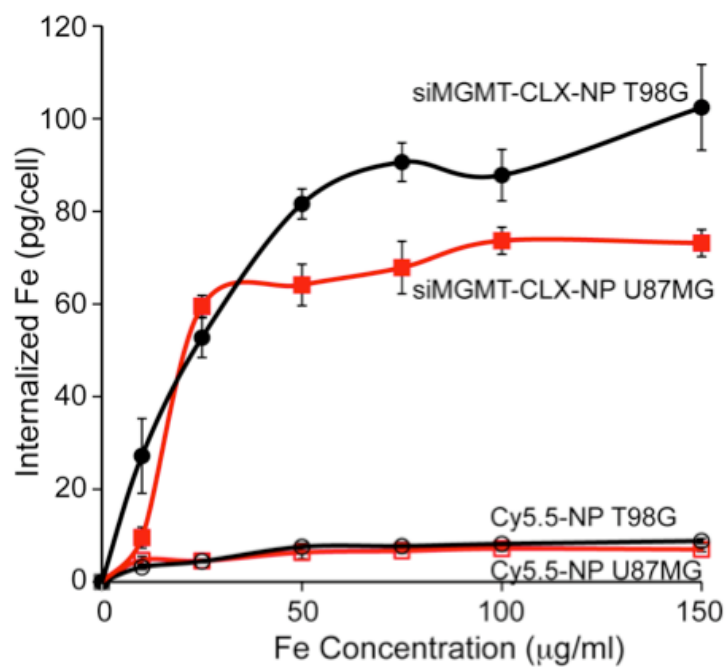


Figure 3.3. Iron uptake assay. T98G and U87MG cells were treated with different concentrations of siMGMT-CLX-NPs or unmodified Cy5.5-NPs for 48 hours. The internalized iron content was determined by iron assay and normalized by cell number. CLX promoted significant nanoparticle uptake in both cell lines.

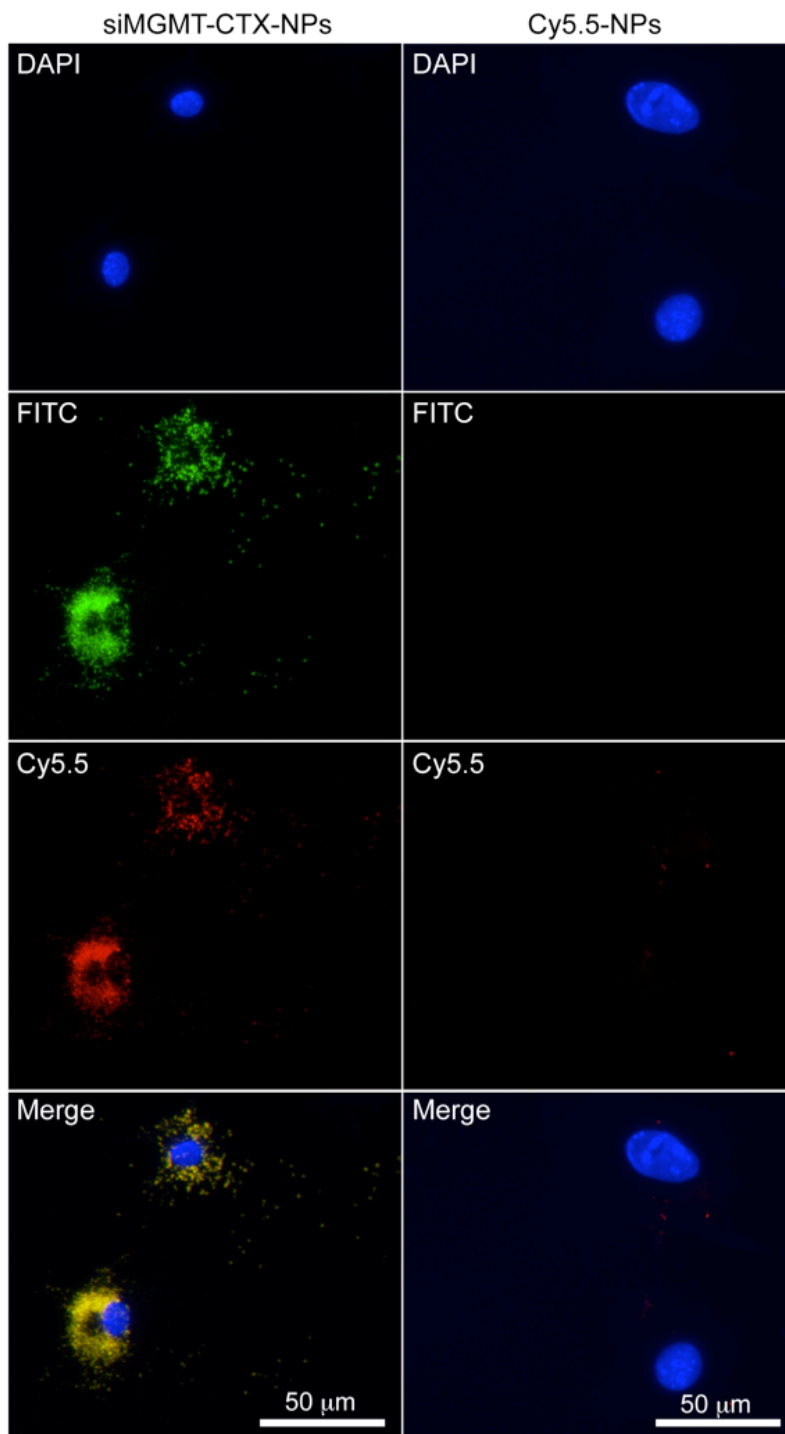


Figure 3.4. Cellular distribution of siMGMT-CLX-NPs. T98G cells treated with siMGMT-CLX-NPs or Cy5.5-NPs were evaluated by fluorescence microscopy. There was a co-localization of Cy5.5 and FITC signal indicating probe uptake by the cells. In contrast, Cy5.5-NP treatment was not accompanied by any significant probe accumulation, indicating that CLX is necessary for probe uptake.

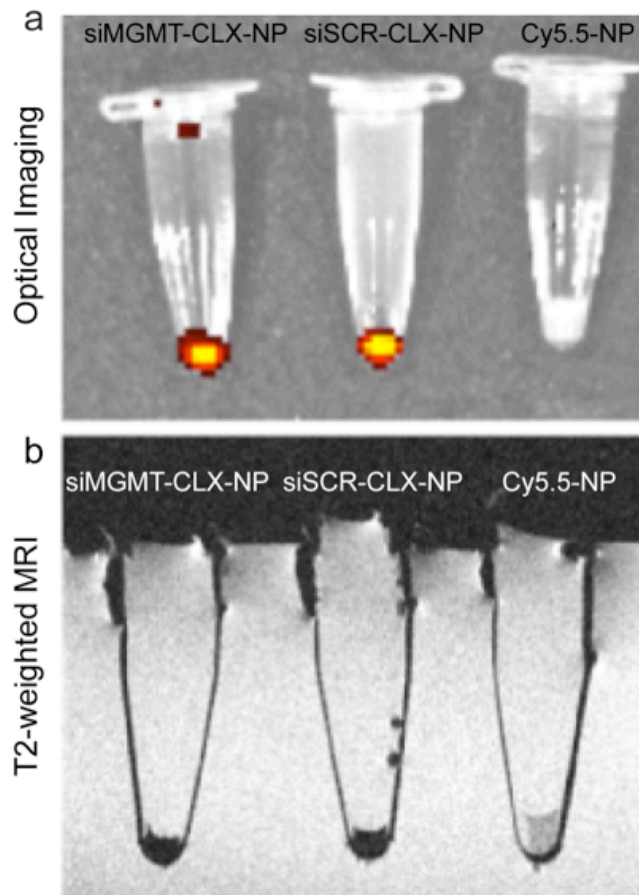


Figure 3.5. Optical and MR imaging of cell pellets. T98G cells were incubated with siMGMT-CLX-NPs, siSCR-CLX-NPs or Cy5.5-NPs and harvested to form cell pellet phantoms. a) Uptake of nanoparticles was evident by optical imaging, with significant Cy5.5 signal present in cells treated with nanoparticles functionalized with tumor-targeting peptide CLX. b) Cellular uptake was also confirmed by T2-weighted magnetic resonance imaging. Internalized nanoparticles were associated with signal loss in siMGMT-CLX-NP and siSCR-CLX-NP treated cell pellets in MRI images. No corresponding effect was observed in cells treated with Cy5.5-NPs.

to the cells treated with Cy5.5-NPs, signifying T2 shortening in phantoms that denotes uptake of probes (Figure 3.5b).

3.3.3 Bioactivity of siMGMT-CLX-NPs

After establishing that siMGMT-CLX-NPs and control siSCR-CLX-NPs are taken up by glioma cells after incubation, we focused on evaluating the molecular consequences of probe internalization. First, the baseline expression of MGMT in the T98G and U87MG GBM cell lines was determined by western blot analysis, which confirmed that T98G cells have high MGMT expression and U87MG cells have no MGMT expression (results not shown). To evaluate the silencing effect of probes on MGMT expression, cultured T98G cells were treated with siMGMT-CLX-NPs, siSCR-CLX-NPs or unmodified Cy5.5-NPs and then processed for real time quantitative RT-PCR analysis. The siMGMT-CLX-NPs caused 38.3% reduction in MGMT mRNA expression relative to unmodified NPs and 26.2% relative to NP containing scrambled siRNA (Figure 3.6a). A small silencing effect observed with scrambled siRNA nanoparticles is common and associated with off-target effects that may be caused by the siRNA transfection process. The MGMT gene knockdown achieved by siMGMT-CLX-NPs at the mRNA level was associated with a reduction in protein expression as assessed by western blot analysis (Figure 3.6b). MGMT protein expression decreased by 52% in T98G cells treated with 50 $\mu\text{g/ml}$ of Fe (475 pmol/ml siRNA) siMGMT-CLX-NPs. No apparent changes in expression were observed in cells treated with low-dose siMGMT-CLX-NPs (25 $\mu\text{g/ml}$ of Fe) or with siSCR-CLX-NPs (50 $\mu\text{g/ml}$ of Fe) relative to unmodified NP controls. We evaluated whether this apparent decrease in protein expression had functional consequences by performing MGMT activity assays on lysates

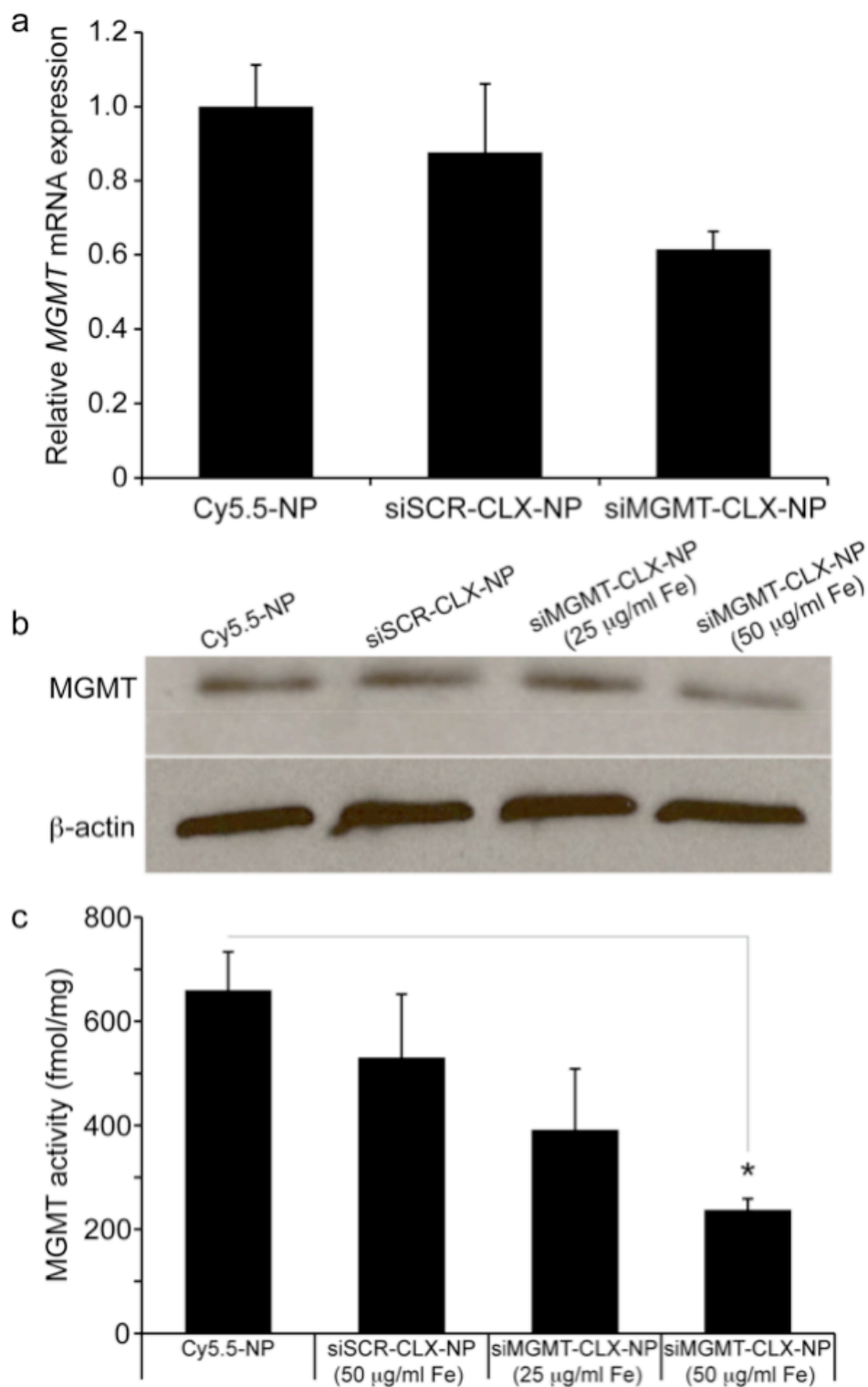


Figure 3.6. Bioactivity of probes. T98G cells were treated with siMGMT-CLX-NPs, siSCR-CLX-NPs, or unmodified nanoparticles (Cy5.5-NPs). Gene expression was evaluated at the mRNA and protein levels by real time quantitative RT-PCR and western

Figure 3.6. (Continued). blotting, respectively. Treatment with siMGMT-CLX-NPs was associated with a reduction in MGMT (a) mRNA expression and (b) protein expression. The effect of this gene knockdown on cellular MGMT activity was determined by (c) MGMT activity assay. Treatment with targeted nanoparticles (siMGMT-CLX-NP, 50 $\mu\text{g/ml}$ of Fe) resulted in a significant reduction in MGMT activity. The * denotes statistical significance.

of treated cells. MGMT activity was quantified by the transfer of radioactive trityl methyl group from donor calf thymus DNA (CT-DNA) to MGMT from cells. Consistent with the results of RT-PCR and western blotting, siMGMT-CLX-NP treatment (50 $\mu\text{g/ml}$ of Fe) was effective in reducing MGMT activity. In these cells, a pronounced 64.1% decrease in MGMT activity relative to unmodified NP treatment was achieved, a reduction that proved to be significant (Figure 3.6c). MGMT expression was not significantly affected by treatment with nanoparticles containing non-targeting, scrambled control siRNA, though activity levels were reduced by 19.6% in these cells. This is consistent with off-target effects potentially caused by the CLX nanoparticle mode of delivery. Low concentration siMGMT-CLX-NP treatment (25 $\mu\text{g/ml}$ of Fe) was associated with MGMT activity reduction of 40.7% relative to unmodified NP treatment. However, this reduction also failed to achieve statistical significance.

After demonstrating that nanoparticles targeting MGMT expression were effective in reducing MGMT enzyme activity, we tested whether siMGMT-CLX-NP pretreatment enhances TMZ cytotoxicity. T98G cells pre-incubated with siMGMT-CLX-NP or control probes were exposed to TMZ (100 μM) for four hours. Cell survival is shown in Figure 3.7 for the different treatment groups. Cells treated with unmodified nanoparticles exhibited no significant response to TMZ, with nearly 100% survival. In contrast, cells treated with siMGMT-CLX-NPs had a dramatic reduction in survival by 38.5% relative to PBS-treated cells. It is notable that reduction in cell survival by 24.3% after siSCR-CLX-NPs treatment was also observed. The reductions after siMGMT-CLX-NP and siSCR-CLX-NP treatments are significant relative to both PBS-treated and Cy5.5-NP-treated cells. These results suggest that suppression of MGMT by

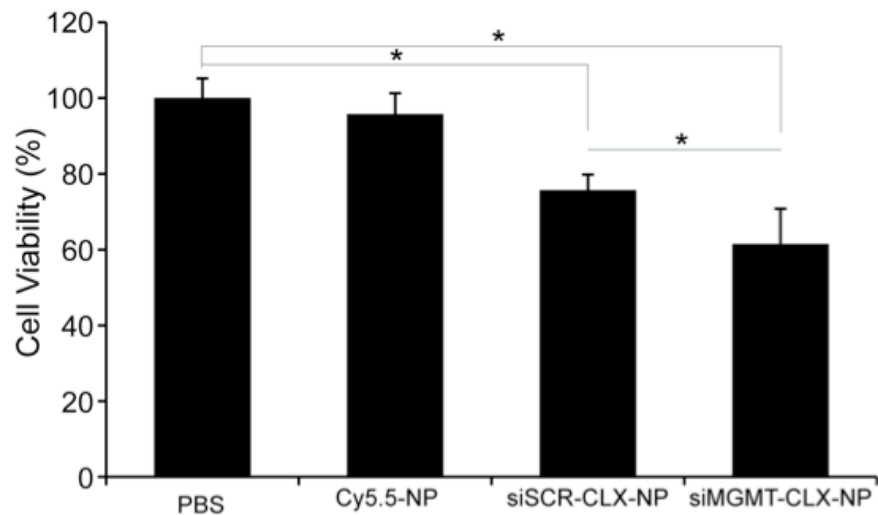


Figure 3.7. Synergic effects of siMGMT-CLX-NP and temozolomide (TMZ) treatment. T98G cells pretreated with siMGMT-CLX-NP, control nanoparticles (Cy5.5-NP and siSCR-CLX-NP) or PBS were exposed to TMZ (100 μ M) and cell survival was assessed. The viabilities of cells treated with siMGMT-CLX-NPs and siSCR-CLX-NPs were both reduced relative to PBS and Cy5.5-NP-treated cells, indicating that chlorotoxin contributes to cell death after TMZ treatment. MGMT gene knockdown also contributed to cell death, and was observed as a reduction in cell viability in siMGMT-CLX-NP treated cells relative to siSCR-CLX-NP treated cells. The * denotes statistical significance.

nanoparticles contributes to enhancement of TMZ chemotherapy, resulting in a significant decrease in cell viability of approximately 36% beyond that achieved by siSCR-CLX-NP treatment. More importantly, they show that chlorotoxin is the main contributor to cell death after TMZ treatment. After demonstrating that functionalized CLX nanoparticles are effective in improving the tumor cell responsiveness to temozolomide treatment, we proceeded to in vivo models.

3.3.4 Intravenous Delivery of siMGMT-CLX-NP Probes in Glioblastoma Model

To test whether siMGMT-CLX-NPs can be effectively delivered to glioblastoma tumors in vivo and enhance temozolomide cytotoxicity, we first developed a T98G xenograft model. MGMT-expressing cell lines like T98G are associated with low de novo tumorigenicity that has hampered in vivo studies (Stein 1979; Potapova, Fakhrai et al. 1996; Rubenstein, Shaw et al. 1999; Naumov, Bender et al. 2006). Therefore, it was necessary for us to develop a procedure that would induce the formation of tumors from T98G cells. For this, we employed a method that has been used to transform primary glioblastomas to xenografts (Carlson, Pokorny et al. 2011). First, a subcutaneous tumor model was established by inoculating immunocompromised mice in the flank with T98G cells that have been incorporated into a basement membrane matrix for improved tumor nucleation (Figure 3.8a-c). Next, the excised tumor was processed to form short-term explant cultures that were propagated in culture flasks prior to inoculation in the brains of recipient mice (Figure 3.8d). We elected to use short-term explants rather than tumor pieces in the formation of orthotopic brain tumors because the former method is associated with more uniform tumor growth (Carlson, Pokorny et al. 2011). Explant

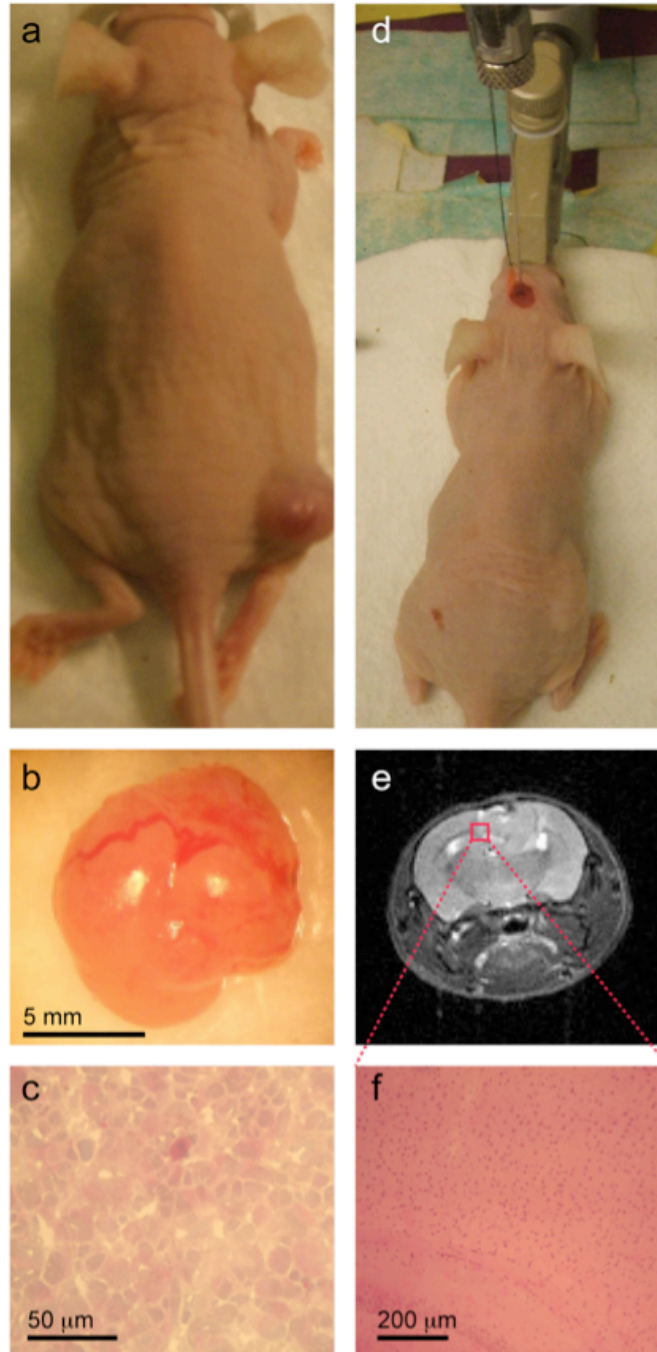


Figure 3.8. Establishment of T98G xenograft model. (a) Subcutaneous T98G tumors were grown by inoculating T98G cells with Matrigel (BD Biosciences) in the flanks of nude mice. (b) Flank tumors were excised and observed by (c) H&E staining to confirm the presence of cancer cells. Excised flank tumor explants were disrupted to form cell suspensions that were propagated in cell culture. (d) Explant cultures were stereotactically injected into the brain and evaluated by (e) MRI and (f) histology.

cultures were tested for iron uptake and MGMT expression, and each were similar to those observed in parental T98G cells (data not shown).

Following orthotopic injection of T98G cells, weekly MRI scanning was used to monitor brain tumor growth (Figure 3.8e). Brain tumors appeared as hyperintense regions in MRI scans (Figure 3.9a, Pre-contrast). At the time of brain tumor appearance, we initiated two rounds of nanoparticle/TMZ treatment. Each round of treatment entailed intravenous injection of mice with siMGMT-CLX-NPs (10 mg/kg Fe, 95 nmol/kg siRNA) or control CLX-NPs (10 mg/kg Fe), followed a day later by 5 days of TMZ administration (i.p. 50 mg/kg/day). MRI was performed after the first nanoparticle injection to evaluate probe delivery. Ideally, nanoparticle accumulations should lead to T2 shortening and image darkening of tumors in MRI scans. However, no significant negative contrast enhancement was observed in treated mice (Figure 3.9a, Post-contrast), calling into question whether efficient tumor delivery had taken place. To investigate this further we performed histology and quantitative RT-PCR analysis on nanoparticle-treated brain tumors after sacrifice. The presence of a small number of nanoparticles in tumor tissue was confirmed by fluorescence microscopy of Cy5.5 (Figure 3.9b). However, nanoparticles failed to induce any significant change in MGMT expression (Figure 3.9c). Furthermore, no difference in tumor volume between siMGMT-CLX-NP and control treated mice was observed (Figure 3.9d). These results indicate that nanoparticle accumulation observed in the tumor after intravenous injection was insufficient to induce gene silencing or improve tumor responsiveness to TMZ chemotherapy. Since elevated MGMT expression has been shown to cause poor vascularization of tumors (Chahal, Xu et al. 2010), we next investigated whether this was the case with T98G tumors. We

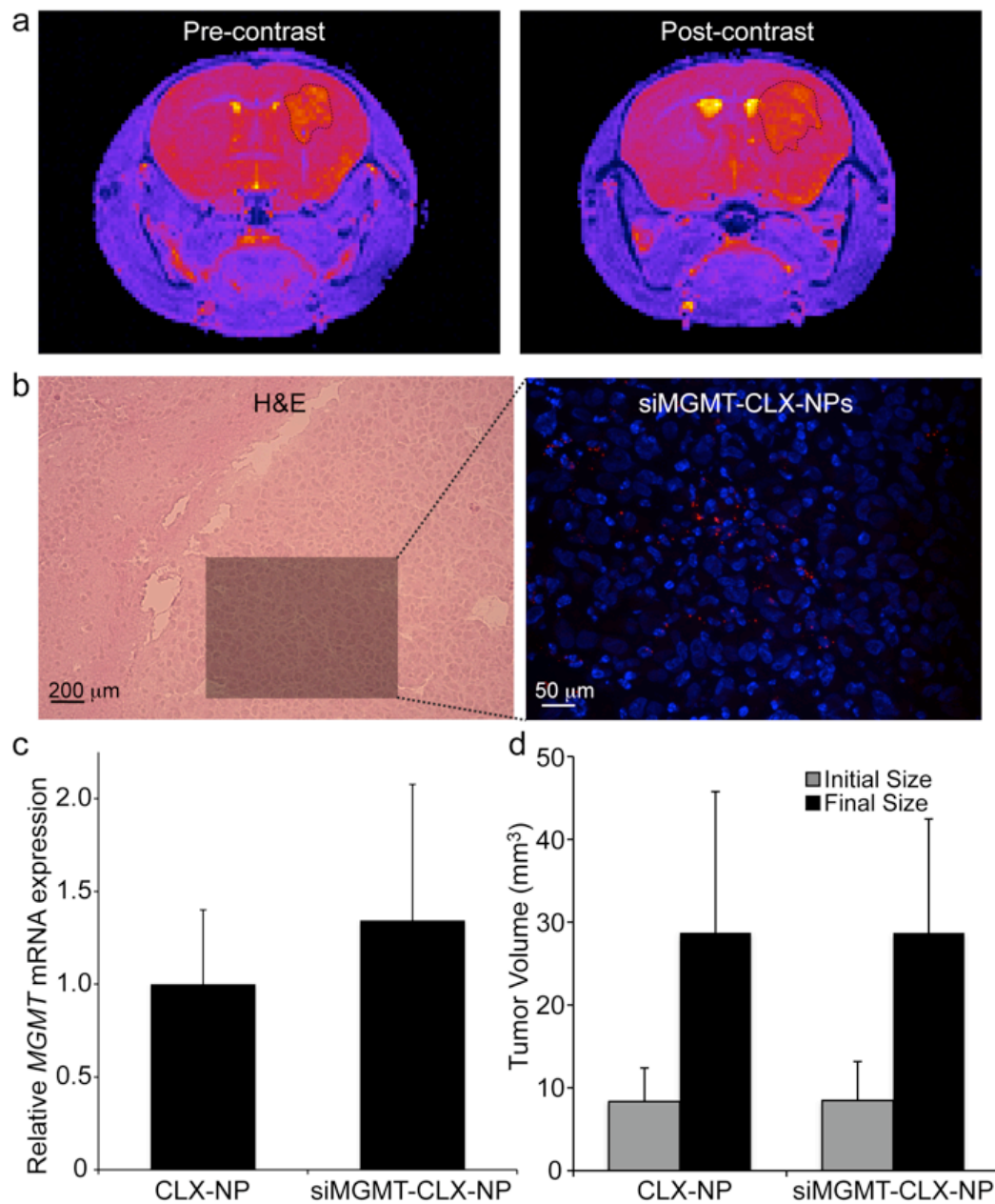


Figure 3.9. Intravenous delivery of siMGMT-CLX-NPs. T98G orthotopic tumors in mice were visualized by (a) magnetic resonance imaging before (Pre-contrast) and after (Post-contrast) the injection of siMGMT-CLX-NPs or control CLX-NPs. Nanoparticle injection was not associated with tumor enhancement despite (b) traces of nanoparticle accumulations observed as Cy5.5 signal in fluorescence microscopy images. (c) Real time quantitative RT-PCR also indicated no significant effect of nanoparticles on tumor MGMT expression. (d) Likewise, no difference in final tumor volume between TMZ-treated mice injected with siMGMT-CLX-NPs and control NPs was observed.

compared vascularization of T98G and U87MG tumors and found that there were approximately two times fewer blood vessels in any given field of view in T98G tumors (60.8 ± 27.3 vessels/ mm^2) compared to U87MG tumors (131.9 ± 21.3 vessels/ mm^2) that lack MGMT expression (Figure 3.10). We next evaluated alternative methods of siMGMT-CLX-NP administration for glioblastoma treatment.

3.3.5 Intratumoral Delivery of siMGMT-CLX-NP Probes in Glioblastoma Model

Improving siMGMT-CLX-NP delivery and effectiveness through direct intratumoral injection was investigated in the mouse orthotopic glioblastoma model that we developed in the previous study. The nanoparticle and TMZ treatment schedule used for this series of experiments is illustrated in Figure 3.11a. After orthotopic brain tumor growth was confirmed by MRI (Figure 3.11b-d, Pre-treatment), a first dose of siMGMT-CLX-NPs ($10.5 \mu\text{g Fe}$, 100 pmol siRNA), CLX-NPs ($10.5 \mu\text{g Fe}$), or PBS was injected into the tumor using a stereotactic frame at injection coordinates derived from MR scans. This was followed one day later by five consecutive days of TMZ treatment (i.p. 50 mg/kg/day). Two additional rounds of nanoparticle and TMZ treatment were performed, followed by one round of TMZ treatment alone.

MR images of control PBS-treated mice (Figure 3.11b, Pre-sacrifice) show that brain tumors grew unabated despite TMZ treatment. This confirmed the chemotherapy resistance of MGMT-expressing cells that had been observed clinically. MR imaging of nanoparticle-treated tumors revealed abundant uptake of siMGMT-CLX-NPs and CLX-NPs by tumors, which was evident as image-darkened regions in T2-weighted MR scans (Figure 3.11c-d, Pre-sacrifice). Nanoparticle accumulations were generally restricted to within the boundaries of the tumor, though in select cases they were observed in the

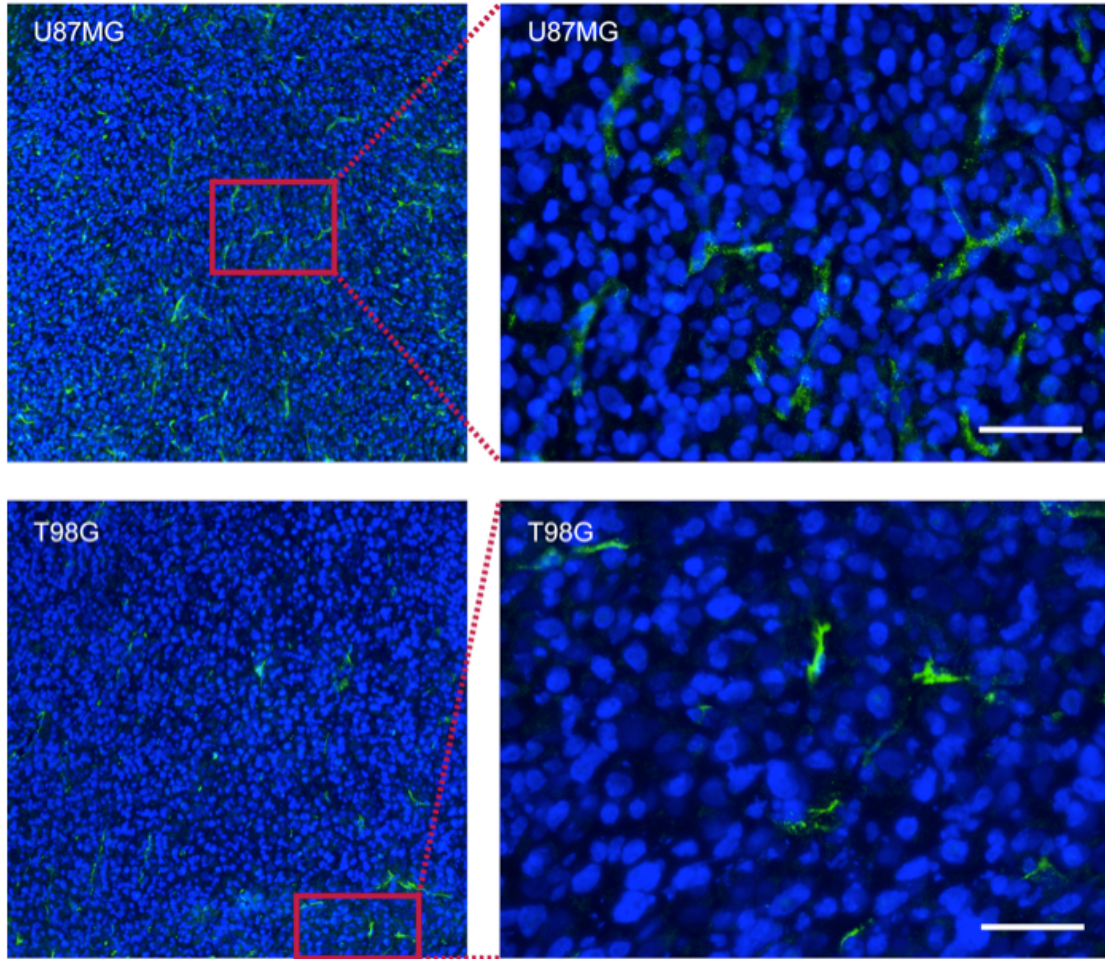


Figure 3.10. T98G and U87MG tumor vasculature. Orthotopic T98G and U87MG tumors were stained for CD34 expression of endothelial cells to identify differences in vascularity. MGMT-positive T98G tumors were associated with decreased vessel number relative to MGMT-null U87MG tumors. Scale bar = 50 μ m.

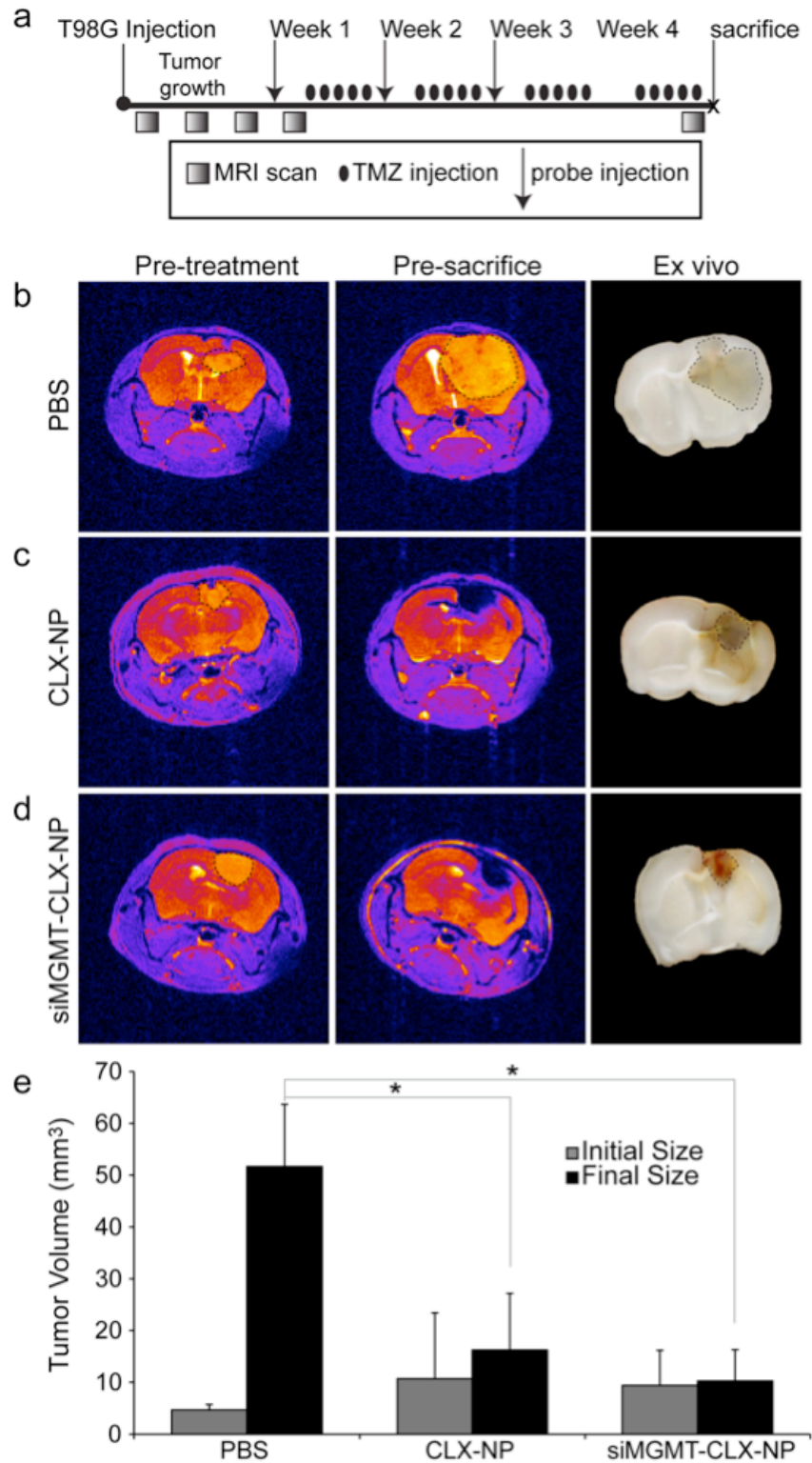


Figure 3.11. Intratumoral siMGMT-CLX-NP delivery and efficacy. The administration of siMGMT-CLX-NPs, CLX-NP or PBS to tumors by direct stereotactic injection with periodic MRI imaging was performed as illustrated (a). For each of three

Figure 3.11. (Continued). weeks, intratumoral injection of probes was followed by five days of TMZ treatment. During the fourth week, probe injection was omitted and a final course of TMZ was administered. MR imaging performed at the time of tumor appearance (Pre-treatment) and sacrifice (Pre-sacrifice) for PBS-treated (b), CLX-NP treated (c) and siMGMT-CLX-NP treated (d) mice demonstrated robust uptake of nanoparticles by tumors. Tumor margins and nanoparticle uptake was also evident in ex vivo tissue scans. (d) Both siMGMT-CLX and CLX nanoparticle treatments were associated with significant reductions in tumor volume relative to PBS-treated control mice. There was a small reduction in tumor size in siMGMT-CLX-NP-treated animals compared to CLX-NP-treated animals. The * denotes statistical significance.

lateral ventricles of the brain. Following the full course of treatment, mice were sacrificed and their brains excised, sectioned and scanned with a Dell 810 flatbed scanner (Figure 3.11b-d, Ex vivo). Initial tumor volumes, obtained from pre-treatment MR images, and final tumor volumes, obtained from ex vivo brain scans, are shown in Figure 3.11e. Interestingly, tumor sizes in siMGMT-CLX-NP and CLX-NP treated mice were both significantly reduced relative to PBS-treated mice. This shows that tumor volume is impacted by the combination treatment of nanoparticles and chemotherapy. The final tumor volumes of mice treated with each type of nanoparticles were not significantly different than their respective initial volumes, demonstrating that nanoparticle treatment was effective in almost eliminating tumor growth in these animals. The final tumor volume of mice treated with siMGMT-CLX-NPs was smaller than for mice treated with CLX-NPs, which is consistent with our observations in the in vitro synergistic studies. However, this difference was not statistically significant. The outcome of this study suggests that while MGMT-specific siRNA contributes to the reduction in tumor size by synergizing TMZ treatment, chlorotoxin contribution was also significant in the reduction in tumor volume that we observed. To obtain greater insight into these results we analyzed the MGMT gene expression and activity in the tumor tissues of treated mice (Figure 3.12). Western blot analysis showed that mice treated with siMGMT-CLX-NPs had a marked reduction in MGMT gene expression of nearly 68% relative to PBS-treated mice and more than 45% relative to CLX-NP treated mice (Figure 3.12a). CLX-NP treatment was associated with a slight reduction in MGMT expression compared to PBS treatment, but this difference was not statistically significant. Furthermore, siMGMT-CLX-NP treatment led to a reduction in MGMT activity to below the limit of detection of

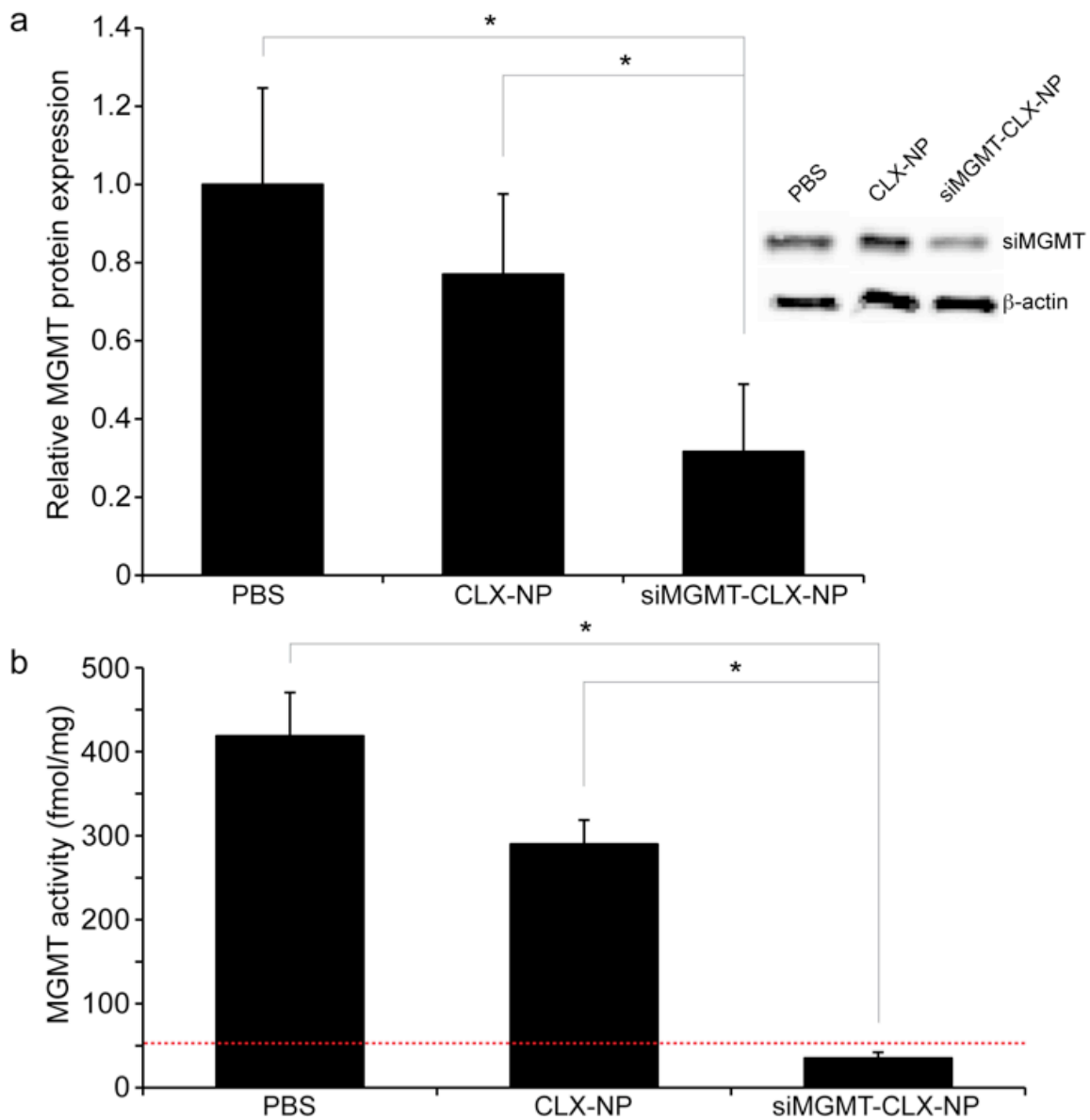


Figure 3.12. Bioactivity of siMGMT probes in glioblastoma tumors. (a) Western blot analysis revealed that tumors receiving siMGMT-CLX-NP treatment had significant reductions in MGMT protein expression relative to both PBS and CLX-NP treated tumors. (b) MGMT activity assay showed that MGMT activity was suppressed in siMGMT-CLX-NP treated tumors. The * denotes statistical significance.

the assay (Figure 3.12b, red dashed line), demonstrating a potent suppressive effect. It is noteworthy that CLX-NP treatment led to reductions in tumor size without comparable suppressions in MGMT expression or activity.

Histological staining of tissues for the presence of iron with Prussian blue stain revealed abundant nanoparticle uptake in tumor cells treated with siMGMT-CLX-NPs and CLX-NPs (Figure 3.13a-c). This was confirmed by fluorescence microscopy of the Cy5.5 nanoparticle label (Figure 3.13d-f). PBS treated mice had intact tumors with large nuclei and irregular cell morphology characteristic of neoplastic tissues as seen by H&E staining (Figure 3.13g). In both types of nanoparticle treated tumors there was evidence of degenerated tumor nuclei and tissue degradation associated with internalized nanoparticles (Figure 3.13h-i). In these treated tissues several signs of cell death, including condensation of the chromatin in the nucleus and fragmentation of nuclear material, were apparent. This was most pronounced for siMGMT-CLX-NP tumors, in which there were fewer instances of healthy intact tumor cells than were observed in tumors treated with CLX-NPs.

Together, these results suggest that the presence of nanoparticles influences the response of tumor cells to TMZ-induced cell death. Although almost complete reductions in MGMT activity were achieved using siMGMT-CLX-NPs, the overall tumor responses we observed in mice cannot be attributed solely to MGMT-dependent mechanisms. There is evidence that the progression to cell death was also due to the presence of the CLX targeting moiety. Below we consider the implications of this finding and future directions of investigation.

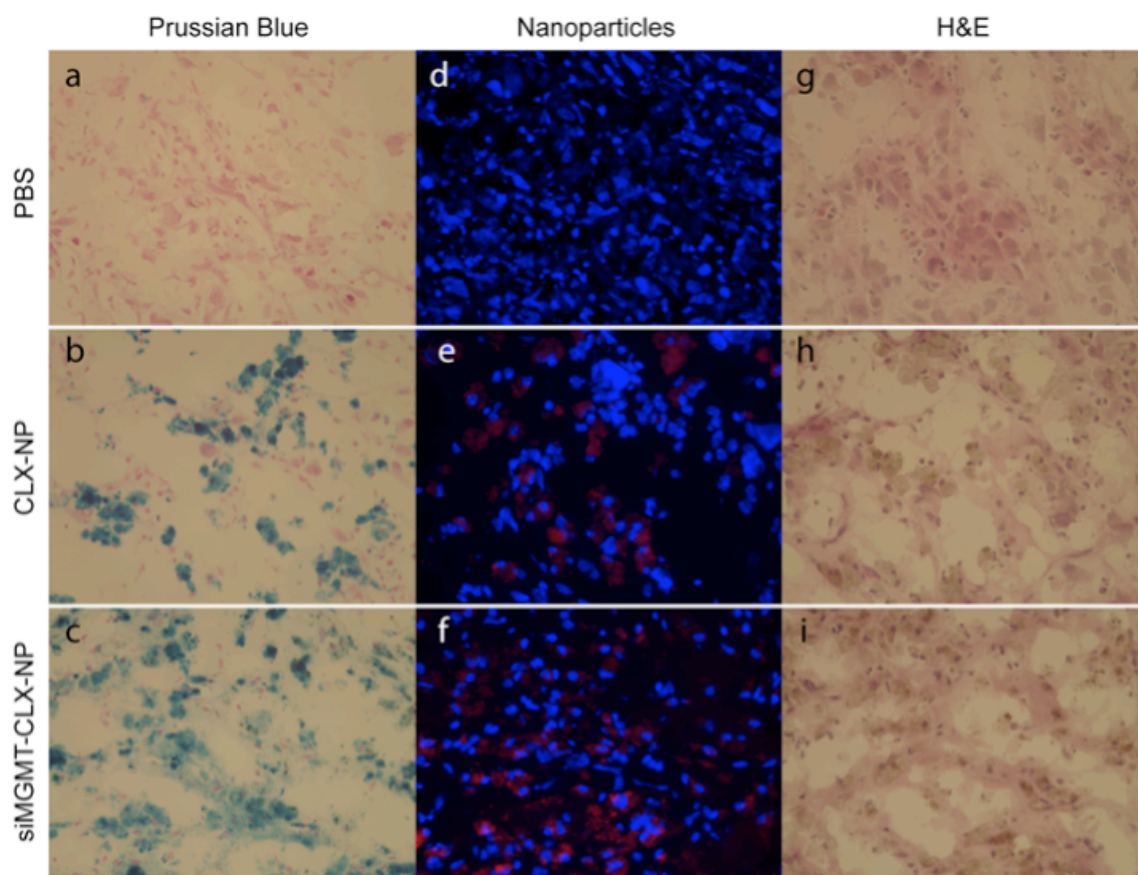


Figure 3.13. Histological staining of T98G brain tumors. Tumors treated with PBS, CLX-NP or siMGMT-CLX-NP (a-c) were stained with Prussian blue to visualize iron content. DAPI stained tissues were evaluated by fluorescence microscopy (d-f) for the presence of Cy5.5-labeled nanoparticles. (g-i) H&E (hematoxylin and eosin) staining revealed that nanoparticle uptake was associated with tumor degradation.

3.4 Discussion

In this work our focus was to use RNA interference to reduce the tumor expression of MGMT, a protein implicated in chemotherapy resistance, in order to improve the response of gliomas to temozolomide. For this we investigated iron oxide nanoparticles as targeted vectors for the delivery of siRNA to tumor cells in culture and in an animal model of glioblastoma. In cell studies we demonstrated that functionalizing nanoparticles with chlorotoxin peptide promoted their uptake by glioblastoma cell lines. The internalized nanoparticles were visible by magnetic resonance imaging due to the intrinsic MR contrast imparted by iron oxide nanoparticles, and by optical imaging through the dual fluorescent labels incorporated into the probes. Internalized nanoparticles were bioactive, leading to reductions in MGMT mRNA expression, protein expression, and activity in a TMZ-resistant cell line, T98G. Suppression of MGMT expression led to enhanced cytotoxicity of temozolomide in these cells. We also investigated nanoparticles for intravenous treatment in an orthotopic glioblastoma mouse model of brain cancer. It was evident from MRI and confirmed by RT-PCR analysis that intravenous injection of nanoparticles failed to traffic to tumor tissues. In our previous experience with U87MG tumors, intravenous nanoparticle injection was associated with significant reduction in T2 relaxation that was grossly evident in T2-weighted images and T2 maps (Kumar, Medarova et al. 2010). In that study, accumulation of nanoparticles in tumors was attributed to vascular changes occurring in late stage U87MG tumor development that led to their increased permeability to materials in the nanometer size range (Hobbs, Monsky et al. 1998). Evidence of highly vascularized U87MG tumors was also suggested by the high T2 values of unenhanced tumor tissues that easily

distinguished them from surrounding normal brain. In contrast, the T98G tumors in our studies generally had much lower (by > 5 ms) average T2 values than U87MG tumors, values that were only slightly elevated above the T2 values of normal tissue. MRI analysis suggests that T98G brain lesions are less vascularized and permeable than their U87MG counterparts, which would account for the limited intravenous delivery to tissues we observed in these tumors. This observation was confirmed histologically by staining of brain tumor vasculature of the two cell types. The scientific literature also suggests that MGMT-expressing tumors are poorly vascularized (Chahal, Xu et al. 2010).

After confirming that systemic administration of nanoparticles was unable to modulate MGMT expression and sensitize cells to the effects of temozolomide, we investigated direct intratumoral administration of siMGMT-CLX-NPs. Intratumoral administration techniques are feasible and have been used clinically to improve delivery to gliomas and to decrease systemic toxicity of drugs and imaging agents (Oshiro, Tsugu et al. 2006; Cordier, Forrer et al. 2010; Jenkinson, Smith et al. 2010). Stereotactically-injected nanoparticles were generally well-tolerated by the mice in our experiments. After injection, nanoparticles spread throughout the tumor parenchyma and remain therein through the full course of the experiment as observed by MRI. Weekly nanoparticle injections were performed to overcome the siRNA dilution and blunted silencing response that occurs for cells with short doubling times such as T98G (i.e., 26 ± 2 hours) (Stein 1979; Bartlett and Davis 2006). Our investigations of direct siMGMT-CLX-NP administration revealed several important findings. First, siMGMT-CLX-NPs differed significantly from CLX-NPs in its effects on MGMT protein expression and activity. Our siMGMT-CLX-NPs performed as they were designed to,

resulting to reductions in MGMT protein expression so complete that enzyme activity was effectively eliminated in treated tumor samples. One would expect that once MGMT activity ceased, tumors would be completely susceptible to the effects of TMZ. In fact, we did observe large reductions in tumor volume in these mice relative to PBS controls. Moreover, within two weeks of siMGMT-CLX-NP injection, tumors generally appeared quiescent when monitored by MRI, with no large increases in apparent tumor volume over time. However, these characteristics were not restricted to tumors treated with siMGMT-CLX-NPs. Despite having little effect on MGMT expression or activity, CLX-NPs were also associated with reductions in tumor volume, though less than those observed for siMGMT-CLX-NPs. Given the important contribution of chlorotoxin to the efficacy of our nanoparticles, we would like to briefly consider the effects of this targeting peptide.

Chlorotoxin is a 36-amino acid peptide derived from scorpion venom (Soroceanu, Gillespie et al. 1998; Lyons, O'Neal et al. 2002). Its selectivity for all grades of gliomas, and not normal astrocytes and neurons, has made chlorotoxin an attractive tumor-targeting moiety for nanoparticles (Veiseh, Sun et al. 2005). When chlorotoxin nanoparticles were applied at diagnostic concentrations they were not found to be toxic (Veiseh, Sun et al. 2009). Accordingly, chlorotoxin has generally been used in combination with potent cancer drugs or therapeutic siRNAs to trigger cell death in tumors (Sun, Fang et al. 2008; Veiseh, Kievit et al. 2010). However, there is significant evidence that chlorotoxin has its own anti-angiogenic and anti-proliferative effects on cancers. It is believed that chlorotoxin binds to glioma chloride channels and disrupts the generation of chloride gradients that are essential for the migration and invasiveness of

glioma cells (McFerrin and Sontheimer 2006). Chlorotoxin treatment of glioma cells in vitro at concentrations below those used in some of our experiments was associated with reductions in cell proliferation (Fu, Yin et al. 2007). Another study found that chlorotoxin binds specifically to matrix metalloproteinase 2 on the surface of gliomas, inhibiting its catalytic activity and ultimately reducing degradation and remodeling of the extracellular matrix that is essential for cell invasion (Deshane, Garner et al. 2003). More recently, Annexin A2, expressed in a variety of tumor types, was identified as a binding partner for chlorotoxin (Kesavan, Ratliff et al. 2010). Chlorotoxin binding to Annexin A2 inhibits VEGF-induced tissue plasminogen activator and angiogenesis. These studies provide insight into the reason for the chlorotoxin-induced cytotoxicity we observed in cell and in vivo studies. Histologically there is some evidence that siMGMT-CLX-NPs induce more complete tumor destruction than CLX-NPs. In tissues with siMGMT-CLX-NP treatment and MGMT knockdown, more widespread nuclear fragmentation and condensation were observed than in CLX-NP treated tissues. This observation provides evidence that MGMT knockdown is an important factor in the complete destruction of tumors after temozolomide treatment. However, more work needs to be done to quantify the differential cytotoxic effects of the two types of nanoparticle treatments and to more precisely characterize their mechanisms of action in our model.

In summary, we have demonstrated that iron oxide nanoparticles functionalized with siRNA induce robust knockdown of endogenous MGMT levels and activity in glioma cells and in an orthotopic glioblastoma mouse model. Suppression of MGMT enhanced cell sensitivity to temozolomide treatment and was associated with widespread tumor destruction. Furthermore, we confirmed the therapeutic efficacy of the chlorotoxin

component of nanoparticles, which proved cytotoxic when administered independent of siRNA. These results suggest that combination chlorotoxin and siRNA delivery by nanoparticles may be an effective treatment option for cells that are resistant to the effects of standard chemotherapies. Future studies will focus on investigating the mechanism and extent of tumor destruction after nanoparticle treatment.

4. References

- (1995). "Tissue plasminogen activator for acute ischemic stroke. The National Institute of Neurological Disorders and Stroke rt-PA Stroke Study Group." N Engl J Med **333**(24): 1581-7.
- (1998). *Culturing Nerve Cells*. G. a. K. G. Banker. Cambridge, MA, MIT Press.
- (2001). "Prevalence of disabilities and associated health conditions among adults--United States, 1999." MMWR Morb Mortal Wkly Rep **50**(7): 120-5.
- (2001). "Use of anti-ICAM-1 therapy in ischemic stroke: results of the Enlimomab Acute Stroke Trial." Neurology **57**(8): 1428-34.
- Agrawal, A., D. H. Min, et al. (2009). "Functional delivery of siRNA in mice using dendriworms." ACS Nano **3**(9): 2495-504.
- Ahmad, M., Y. Zhang, et al. (2009). "Prolonged opportunity for neuroprotection in experimental stroke with selective blockade of cyclooxygenase-2 activity." Brain Res **1279**: 168-73.
- Astriab-Fisher, A., D. Sergueev, et al. (2002). "Conjugates of antisense oligonucleotides with the Tat and antennapedia cell-penetrating peptides: effects on cellular uptake, binding to target sequences, and biologic actions." Pharm Res **19**(6): 744-54.
- Bae, K. H., K. Lee, et al. (2011). "Surface functionalized hollow manganese oxide nanoparticles for cancer targeted siRNA delivery and magnetic resonance imaging." Biomaterials **32**(1): 176-84.
- Bartlett, D. W. and M. E. Davis (2006). "Insights into the kinetics of siRNA-mediated gene silencing from live-cell and live-animal bioluminescent imaging." Nucleic Acids Res **34**(1): 322-33.
- Bartlett, D. W. and M. E. Davis (2007). "Effect of siRNA nuclease stability on the in vitro and in vivo kinetics of siRNA-mediated gene silencing." Biotechnol Bioeng **97**(4): 909-21.
- Bartlett, D. W., H. Su, et al. (2007). "Impact of tumor-specific targeting on the biodistribution and efficacy of siRNA nanoparticles measured by multimodality in vivo imaging." Proc Natl Acad Sci U S A **104**(39): 15549-54.
- Beier, D., S. Rohrl, et al. (2008). "Temozolomide preferentially depletes cancer stem cells in glioblastoma." Cancer Res **68**(14): 5706-15.
- Belayev, L., R. Busto, et al. (1999). "Middle cerebral artery occlusion in the mouse by intraluminal suture coated with poly-L-lysine: neurological and histological validation." Brain Res **833**(2): 181-90.

- Bogousslavsky, J., S. J. Victor, et al. (2002). "Fiblast (trafermin) in acute stroke: results of the European-Australian phase II/III safety and efficacy trial." Cerebrovasc Dis **14**(3-4): 239-51.
- Boussif, O., F. Lezoualc'h, et al. (1995). "A versatile vector for gene and oligonucleotide transfer into cells in culture and in vivo: polyethylenimine." Proc Natl Acad Sci U S A **92**(16): 7297-301.
- Braasch, D. A., S. Jensen, et al. (2003). "RNA interference in mammalian cells by chemically-modified RNA." Biochemistry **42**(26): 7967-75.
- Brouns, R. and P. P. De Deyn (2009). "The complexity of neurobiological processes in acute ischemic stroke." Clin Neurol Neurosurg **111**(6): 483-95.
- Cameron, A., J. Appel, et al. (2000). "Polyarginines are potent furin inhibitors." J Biol Chem **275**(47): 36741-9.
- Carlson, B. L., J. L. Pokorny, et al. (2011). "Establishment, maintenance and in vitro and in vivo applications of primary human glioblastoma multiforme (GBM) xenograft models for translational biology studies and drug discovery." Curr Protoc Pharmacol **Chapter 14**: Unit 14 16.
- Castanotto, D. and J. J. Rossi (2009). "The promises and pitfalls of RNA-interference-based therapeutics." Nature **457**(7228): 426-33.
- Chahal, M., Y. Xu, et al. (2010). "MGMT modulates glioblastoma angiogenesis and response to the tyrosine kinase inhibitor sunitinib." Neuro Oncol **12**(8): 822-33.
- Chen, H. Y., T. Y. Chen, et al. (2006). "Melatonin decreases neurovascular oxidative/nitrosative damage and protects against early increases in the blood-brain barrier permeability after transient focal cerebral ischemia in mice." J Pineal Res **41**(2): 175-82.
- Chen, S. T., C. Y. Hsu, et al. (1986). "A model of focal ischemic stroke in the rat: reproducible extensive cortical infarction." Stroke **17**(4): 738-43.
- Chen, Y., C. Chu, et al. (2011). "Reversible Pore-Structure Evolution in Hollow Silica Nanocapsules: Large Pores for siRNA Delivery and Nanoparticle Collecting." Small.
- Chen, Y., A. Ito, et al. (2008). "Blocking pterygopalatine arterial blood flow decreases infarct volume variability in a mouse model of intraluminal suture middle cerebral artery occlusion." J Neurosci Methods **174**(1): 18-24.
- Cheng, C. Y., S. Y. Su, et al. (2008). "Ferulic acid provides neuroprotection against oxidative stress-related apoptosis after cerebral ischemia/reperfusion injury by inhibiting ICAM-1 mRNA expression in rats." Brain Res **1209**: 136-50.

- Cheng, Y., H. T. Zhang, et al. (2006). "Involvement of cell adhesion molecules in polydatin protection of brain tissues from ischemia-reperfusion injury." Brain Res **1110**(1): 193-200.
- Chinnasamy, N., J. A. Rafferty, et al. (1997). "O6-benzylguanine potentiates the in vivo toxicity and clastogenicity of temozolomide and BCNU in mouse bone marrow." Blood **89**(5): 1566-73.
- Choi, D. W. (1995). "Calcium: still center-stage in hypoxic-ischemic neuronal death." Trends Neurosci **18**(2): 58-60.
- Christmann, M., G. Nagel, et al. (2010). "MGMT activity, promoter methylation and immunohistochemistry of pretreatment and recurrent malignant gliomas: a comparative study on astrocytoma and glioblastoma." Int J Cancer **127**(9): 2106-18.
- Coeytaux, E., D. Coulaud, et al. (2003). "The cationic amphipathic alpha-helix of HIV-1 viral protein R (Vpr) binds to nucleic acids, permeabilizes membranes, and efficiently transfects cells." J Biol Chem **278**(20): 18110-6.
- Collett, M. S., J. S. Brugge, et al. (1978). "Characterization of a normal avian cell protein related to the avian sarcoma virus transforming gene product." Cell **15**(4): 1363-9.
- Connolly, E. S., Jr., C. J. Winfree, et al. (1997). "Exacerbation of cerebral injury in mice that express the P-selectin gene: identification of P-selectin blockade as a new target for the treatment of stroke." Circ Res **81**(3): 304-10.
- Connolly, E. S., Jr., C. J. Winfree, et al. (1996). "Cerebral protection in homozygous null ICAM-1 mice after middle cerebral artery occlusion. Role of neutrophil adhesion in the pathogenesis of stroke." J Clin Invest **97**(1): 209-16.
- Cordier, D., F. Forrer, et al. (2010). "Neoadjuvant targeting of glioblastoma multiforme with radiolabeled DOTAGA-substance P--results from a phase I study." J Neurooncol **100**(1): 129-36.
- Czuderna, F., M. Fechtner, et al. (2003). "Structural variations and stabilising modifications of synthetic siRNAs in mammalian cells." Nucleic Acids Res **31**(11): 2705-16.
- Danbolt, N. C. (2001). "Glutamate uptake." Prog Neurobiol **65**(1): 1-105.
- Davis, M. E., J. E. Zuckerman, et al. (2010). "Evidence of RNAi in humans from systemically administered siRNA via targeted nanoparticles." Nature **464**(7291): 1067-70.
- del Zoppo, G., I. Ginis, et al. (2000). "Inflammation and stroke: putative role for cytokines, adhesion molecules and iNOS in brain response to ischemia." Brain Pathol **10**(1): 95-112.

- Denny, B. J., R. T. Wheelhouse, et al. (1994). "NMR and molecular modeling investigation of the mechanism of activation of the antitumor drug temozolomide and its interaction with DNA." Biochemistry **33**(31): 9045-51.
- Derossi, D., G. Chassaing, et al. (1998). "Trojan peptides: the penetratin system for intracellular delivery." Trends Cell Biol **8**(2): 84-7.
- Derossi, D., A. H. Joliot, et al. (1994). "The third helix of the Antennapedia homeodomain translocates through biological membranes." J Biol Chem **269**(14): 10444-50.
- Deshane, J., C. C. Garner, et al. (2003). "Chlorotoxin inhibits glioma cell invasion via matrix metalloproteinase-2." J Biol Chem **278**(6): 4135-44.
- Deshayes, S., M. C. Morris, et al. (2005). "Interactions of primary amphipathic cell penetrating peptides with model membranes: consequences on the mechanisms of intracellular delivery of therapeutics." Curr Pharm Des **11**(28): 3629-38.
- Diener, H. C., A. AlKhedr, et al. (2002). "Treatment of acute ischaemic stroke with the low-affinity, use-dependent NMDA antagonist AR-R15896AR. A safety and tolerability study." J Neurol **249**(5): 561-8.
- Dilber, M. S., A. Phelan, et al. (1999). "Intercellular delivery of thymidine kinase prodrug activating enzyme by the herpes simplex virus protein, VP22." Gene Ther **6**(1): 12-21.
- Doyle, K. P., R. P. Simon, et al. (2008). "Mechanisms of ischemic brain damage." Neuropharmacology **55**(3): 310-18.
- Du, C. P., J. Gao, et al. (2009). "Increased tyrosine phosphorylation of PSD-95 by Src family kinases after brain ischaemia." Biochem J **417**(1): 277-85.
- Dumenco, L. L., E. Allay, et al. (1993). "The prevention of thymic lymphomas in transgenic mice by human O6-alkylguanine-DNA alkyltransferase." Science **259**(5092): 219-22.
- Elbashir, S. M., J. Harborth, et al. (2001). "Duplexes of 21-nucleotide RNAs mediate RNA interference in cultured mammalian cells." Nature **411**(6836): 494-8.
- Elliott, G. and P. O'Hare (1997). "Intercellular trafficking and protein delivery by a herpesvirus structural protein." Cell **88**(2): 223-33.
- Elmqvist, A., M. Hansen, et al. (2006). "Structure-activity relationship study of the cell-penetrating peptide pVEC." Biochim Biophys Acta **1758**(6): 721-9.
- Elmqvist, A., M. Lindgren, et al. (2001). "VE-cadherin-derived cell-penetrating peptide, pVEC, with carrier functions." Exp Cell Res **269**(2): 237-44.

- Fairbairn, L. J., A. J. Watson, et al. (1995). "O6-benzylguanine increases the sensitivity of human primary bone marrow cells to the cytotoxic effects of temozolomide." Exp Hematol **23**(2): 112-6.
- Farrokhnia, N., M. W. Roos, et al. (2005). "Experimental treatment for focal hyperglycemic ischemic brain injury in the rat." Exp Brain Res **167**(2): 310-4.
- Felgner, P. L., T. R. Gadek, et al. (1987). "Lipofection: a highly efficient, lipid-mediated DNA-transfection procedure." Proc Natl Acad Sci U S A **84**(21): 7413-7.
- Fire, A., S. Xu, et al. (1998). "Potent and specific genetic interference by double-stranded RNA in *Caenorhabditis elegans*." Nature **391**(6669): 806-11.
- Fischer, R., K. Kohler, et al. (2004). "A stepwise dissection of the intracellular fate of cationic cell-penetrating peptides." J Biol Chem **279**(13): 12625-35.
- Fisher, M., D. F. Hanley, et al. (2007). "Recommendations from the STAIR V meeting on acute stroke trials, technology and outcomes." Stroke **38**(2): 245-8.
- Fittipaldi, A., A. Ferrari, et al. (2003). "Cell membrane lipid rafts mediate caveolar endocytosis of HIV-1 Tat fusion proteins." J Biol Chem **278**(36): 34141-9.
- Flecknell, P. A. (1993). "Anesthesia and perioperative care." Methods Enzymol **225**: 16-33.
- Flecknell, P. A. (1996). Laboratory animal anaesthesia: a practical introduction for research workers and technicians San Diego, Academic Press.
- Forster, C., H. B. Clark, et al. (1999). "Inducible nitric oxide synthase expression in human cerebral infarcts." Acta Neuropathol **97**(3): 215-20.
- Frank-Kamenetsky, M., A. Grefhorst, et al. (2008). "Therapeutic RNAi targeting PCSK9 acutely lowers plasma cholesterol in rodents and LDL cholesterol in nonhuman primates." Proc Natl Acad Sci U S A **105**(33): 11915-20.
- Friedman, H. S., J. Pluda, et al. (2000). "Phase I trial of carmustine plus O6-benzylguanine for patients with recurrent or progressive malignant glioma." J Clin Oncol **18**(20): 3522-8.
- Fu, Y. J., L. T. Yin, et al. (2007). "Therapeutic potential of chlorotoxin-like neurotoxin from the Chinese scorpion for human gliomas." Neurosci Lett **412**(1): 62-7.
- Fuchs, S. M. and R. T. Raines (2004). "Pathway for polyarginine entry into mammalian cells." Biochemistry **43**(9): 2438-44.
- Fujimura, M., Y. Gasche, et al. (1999). "Early appearance of activated matrix metalloproteinase-9 and blood-brain barrier disruption in mice after focal cerebral ischemia and reperfusion." Brain Res **842**(1): 92-100.

- Furuya, K., N. Kawahara, et al. (2004). "Proximal occlusion of the middle cerebral artery in C57Black6 mice: relationship of patency of the posterior communicating artery, infarct evolution, and animal survival." J Neurosurg **100**(1): 97-105.
- Futaki, S., T. Suzuki, et al. (2001). "Arginine-rich peptides. An abundant source of membrane-permeable peptides having potential as carriers for intracellular protein delivery." J Biol Chem **276**(8): 5836-40.
- Gary, D. J., H. Lee, et al. (2011). "Influence of nano-carrier architecture on in vitro siRNA delivery performance and in vivo biodistribution: polyplexes vs micelleplexes." ACS Nano **5**(5): 3493-505.
- Geng, J. G., M. P. Bevilacqua, et al. (1990). "Rapid neutrophil adhesion to activated endothelium mediated by GMP-140." Nature **343**(6260): 757-60.
- Ghosh, A. and M. E. Greenberg (1995). "Calcium signaling in neurons: molecular mechanisms and cellular consequences." Science **268**(5208): 239-47.
- Goldberg, M. S., D. Xing, et al. (2011). "Nanoparticle-mediated delivery of siRNA targeting Parp1 extends survival of mice bearing tumors derived from Brca1-deficient ovarian cancer cells." Proc Natl Acad Sci U S A **108**(2): 745-50.
- Golzio, M., L. Mazzolini, et al. (2007). "In vivo gene silencing in solid tumors by targeted electrically mediated siRNA delivery." Gene Ther **14**(9): 752-9.
- Hacke, W., G. Donnan, et al. (2004). "Association of outcome with early stroke treatment: pooled analysis of ATLANTIS, ECASS, and NINDS rt-PA stroke trials." Lancet **363**(9411): 768-74.
- Hamann, G. F., Y. Okada, et al. (1996). "Hemorrhagic transformation and microvascular integrity during focal cerebral ischemia/reperfusion." J Cereb Blood Flow Metab **16**(6): 1373-8.
- Hamann, G. F., Y. Okada, et al. (1995). "Microvascular basal lamina antigens disappear during cerebral ischemia and reperfusion." Stroke **26**(11): 2120-6.
- Hanke, J. H., J. P. Gardner, et al. (1996). "Discovery of a novel, potent, and Src family-selective tyrosine kinase inhibitor. Study of Lck- and FynT-dependent T cell activation." J Biol Chem **271**(2): 695-701.
- Hara, H., P. L. Huang, et al. (1996). "Reduced brain edema and infarction volume in mice lacking the neuronal isoform of nitric oxide synthase after transient MCA occlusion." J Cereb Blood Flow Metab **16**(4): 605-11.
- Hara, K., D. L. Kong, et al. (1998). "Effect of selective inhibition of cyclooxygenase 2 on temporary focal cerebral ischemia in rats." Neurosci Lett **256**(1): 53-6.

- Harris, K. F., I. Shoji, et al. (1999). "Ubiquitin-mediated degradation of active Src tyrosine kinase." Proc Natl Acad Sci U S A **96**(24): 13738-43.
- Hashiguchi, A., T. Kawano, et al. (2003). "The neuroprotective effect of a novel calmodulin antagonist, 3-[2-[4-(3-chloro-2-methylphenyl)-1-piperazinyl]ethyl]-5,6-dimethoxy-1-(4-imidazolylmethyl)-1H-indazole dihydrochloride 3.5 hydrate, in transient forebrain ischemia." Neuroscience **121**(2): 379-86.
- Hatanaka, K., T. Asai, et al. (2010). "Development of double-stranded siRNA labeling method using positron emitter and its in vivo trafficking analyzed by positron emission tomography." Bioconjug Chem **21**(4): 756-63.
- Hayakawa, K., T. Nakano, et al. (2010). "Inhibition of reactive astrocytes with fluorocitrate retards neurovascular remodeling and recovery after focal cerebral ischemia in mice." J Cereb Blood Flow Metab **30**(4): 871-82.
- Hegi, M. E., A. C. Diserens, et al. (2004). "Clinical trial substantiates the predictive value of O-6-methylguanine-DNA methyltransferase promoter methylation in glioblastoma patients treated with temozolomide." Clin Cancer Res **10**(6): 1871-4.
- Hegi, M. E., A. C. Diserens, et al. (2005). "MGMT gene silencing and benefit from temozolomide in glioblastoma." N Engl J Med **352**(10): 997-1003.
- Henriques, S. T., J. Costa, et al. (2005). "Translocation of beta-galactosidase mediated by the cell-penetrating peptide pep-1 into lipid vesicles and human HeLa cells is driven by membrane electrostatic potential." Biochemistry **44**(30): 10189-98.
- Henriques, S. T., A. Quintas, et al. (2007). "Energy-independent translocation of cell-penetrating peptides occurs without formation of pores. A biophysical study with pep-1." Mol Membr Biol **24**(4): 282-93.
- Hery, C., G. Sebire, et al. (1995). "Adhesion to human neurons and astrocytes of monocytes: the role of interaction of CR3 and ICAM-1 and modulation by cytokines." J Neuroimmunol **57**(1-2): 101-9.
- Hobbs, S. K., W. L. Monsky, et al. (1998). "Regulation of transport pathways in tumor vessels: role of tumor type and microenvironment." Proc Natl Acad Sci U S A **95**(8): 4607-12.
- Hockfield, S., S. Carlson, et al. (1993). Fixation by Transcardiac Perfusion. Selected methods for antibody and nucleic acid probes. Plainview, N.Y., Cold Spring Harbor Laboratory Press. **1**: 125-130.
- Hu-Lieskovan, S., J. D. Heidel, et al. (2005). "Sequence-specific knockdown of EWS-FLI1 by targeted, nonviral delivery of small interfering RNA inhibits tumor growth in a murine model of metastatic Ewing's sarcoma." Cancer Res **65**(19): 8984-92.

- Huang, J., T. F. Choudhri, et al. (2000). "Postischemic cerebrovascular E-selectin expression mediates tissue injury in murine stroke." Stroke **31**(12): 3047-53.
- Hunter, A. J., J. Hatcher, et al. (2000). "Functional assessments in mice and rats after focal stroke." Neuropharmacology **39**(5): 806-16.
- Iadecola, C., K. Niwa, et al. (2001). "Reduced susceptibility to ischemic brain injury and N-methyl-D-aspartate-mediated neurotoxicity in cyclooxygenase-2-deficient mice." Proc Natl Acad Sci U S A **98**(3): 1294-9.
- Iadecola, C., F. Zhang, et al. (1996). "Inducible nitric oxide synthase gene expression in vascular cells after transient focal cerebral ischemia." Stroke **27**(8): 1373-80.
- Iadecola, C., F. Zhang, et al. (1997). "Delayed reduction of ischemic brain injury and neurological deficits in mice lacking the inducible nitric oxide synthase gene." J Neurosci **17**(23): 9157-64.
- Ishikawa, M., T. Vowinkel, et al. (2005). "CD40/CD40 ligand signaling in mouse cerebral microvasculature after focal ischemia/reperfusion." Circulation **111**(13): 1690-6.
- Jenkinson, M. D., T. S. Smith, et al. (2010). "Phase II trial of intratumoral BCNU injection and radiotherapy on untreated adult malignant glioma." J Neurooncol **99**(1): 103-13.
- Joshi, C. N., S. K. Jain, et al. (2004). "An optimized triphenyltetrazolium chloride method for identification of cerebral infarcts." Brain Res Brain Res Protoc **13**(1): 11-7.
- Kadotani, H., S. Namura, et al. (1998). "Attenuation of focal cerebral infarct in mice lacking NMDA receptor subunit NR2C." Neuroreport **9**(3): 471-5.
- Kaina, B., G. Fritz, et al. (1991). "Transfection and expression of human O6-methylguanine-DNA methyltransferase (MGMT) cDNA in Chinese hamster cells: the role of MGMT in protection against the genotoxic effects of alkylating agents." Carcinogenesis **12**(10): 1857-67.
- Kang, L., R. F. Wang, et al. (2010). "Noninvasive visualization of RNA delivery with ^{99m}Tc-radiolabeled small-interference RNA in tumor xenografts." J Nucl Med **51**(6): 978-86.
- Karran, P., P. Macpherson, et al. (1993). "O6-methylguanine residues elicit DNA repair synthesis by human cell extracts." J Biol Chem **268**(21): 15878-86.
- Kato, T., A. Natsume, et al. (2010). "Efficient delivery of liposome-mediated MGMT-siRNA reinforces the cytotoxicity of temozolomide in GBM-initiating cells." Gene Ther **17**(11): 1363-71.

- Kelsen, J., K. Kjaer, et al. (2006). "Parecoxib is neuroprotective in spontaneously hypertensive rats after transient middle cerebral artery occlusion: a divided treatment response?" J Neuroinflammation **3**: 31.
- Kenny, G. D., N. Kamaly, et al. (2011). "Novel multifunctional nanoparticle mediates siRNA tumour delivery, visualisation and therapeutic tumour reduction in vivo." J Control Release **149**(2): 111-6.
- Kesavan, K., J. Ratliff, et al. (2010). "Annexin A2 is a molecular target for TM601, a peptide with tumor-targeting and anti-angiogenic effects." J Biol Chem **285**(7): 4366-74.
- Kibler, K. V., A. Miyazato, et al. (2004). "Polyarginine inhibits gp160 processing by furin and suppresses productive human immunodeficiency virus type 1 infection." J Biol Chem **279**(47): 49055-63.
- Kim, S. I., D. Shin, et al. (2007). "Systemic and specific delivery of small interfering RNAs to the liver mediated by apolipoprotein A-I." Mol Ther **15**(6): 1145-52.
- Kim, W. J., L. V. Christensen, et al. (2006). "Cholesteryl oligoarginine delivering vascular endothelial growth factor siRNA effectively inhibits tumor growth in colon adenocarcinoma." Mol Ther **14**(3): 343-50.
- Kimelberg, H. K., P. J. Feustel, et al. (2000). "Acute treatment with tamoxifen reduces ischemic damage following middle cerebral artery occlusion." Neuroreport **11**(12): 2675-9.
- Kitagawa, K., M. Matsumoto, et al. (1998). "Deficiency of intercellular adhesion molecule 1 attenuates microcirculatory disturbance and infarction size in focal cerebral ischemia." J Cereb Blood Flow Metab **18**(12): 1336-45.
- Kleihues, P., P. C. Burger, et al. (1993). "The new WHO classification of brain tumours." Brain Pathol **3**(3): 255-68.
- Kobayashi, S., I. Nakase, et al. (2009). "Cytosolic targeting of macromolecules using a pH-dependent fusogenic peptide in combination with cationic liposomes." Bioconjug Chem **20**(5): 953-9.
- Korematsu, K., S. Goto, et al. (1994). "Microglial response to transient focal cerebral ischemia: an immunocytochemical study on the rat cerebral cortex using anti-phosphotyrosine antibody." J Cereb Blood Flow Metab **14**(5): 825-30.
- Kramer, M., J. Dang, et al. (2010). "TTC staining of damaged brain areas after MCA occlusion in the rat does not constrict quantitative gene and protein analyses." J Neurosci Methods **187**(1): 84-9.
- Kumar, M., Z. Medarova, et al. (2010). "Novel membrane-permeable contrast agent for brain tumor detection by MRI." Magn Reson Med **63**(3): 617-24.

- Kumar, M., Z. Medarova, et al. (2009). "Novel membrane permeable contrast agent for brain tumor detection by MRI." Magn Reson Imaging **In Press**.
- Kumar, M., M. Yigit, et al. (2010). "Image-guided breast tumor therapy using a small interfering RNA nanodrug." Cancer Res **70**(19): 7553-61.
- Kumar, P., H. Wu, et al. (2007). "Transvascular delivery of small interfering RNA to the central nervous system." Nature **448**(7149): 39-43.
- Kuo, C. C., J. F. Liu, et al. (2006). "DNA repair enzyme, O6-methylguanine DNA methyltransferase, modulates cytotoxicity of camptothecin-derived topoisomerase I inhibitors." J Pharmacol Exp Ther **316**(2): 946-54.
- Kuroda, S., A. Nakai, et al. (1997). "The calmodulin antagonist trifluoperazine in transient focal brain ischemia in rats. Anti-ischemic effect and therapeutic window." Stroke **28**(12): 2539-44.
- Landen, C. N., Jr., A. Chavez-Reyes, et al. (2005). "Therapeutic EphA2 gene targeting in vivo using neutral liposomal small interfering RNA delivery." Cancer Res **65**(15): 6910-8.
- Langel, U., Ed. (2007). Handbook of Cell-Penetrating Peptides, CRC Press.
- Layzer, J. M., A. P. McCaffrey, et al. (2004). "In vivo activity of nuclease-resistant siRNAs." RNA **10**(5): 766-71.
- Leist, M., E. Fava, et al. (1997). "Peroxynitrite and nitric oxide donors induce neuronal apoptosis by eliciting autocrine excitotoxicity." Eur J Neurosci **9**(7): 1488-98.
- Lenmyr, F., A. Ericsson, et al. (2004). "Src family kinase-inhibitor PP2 reduces focal ischemic brain injury." Acta Neurol Scand **110**(3): 175-9.
- Letoha, T., S. Gaal, et al. (2003). "Membrane translocation of penetratin and its derivatives in different cell lines." J Mol Recognit **16**(5): 272-9.
- Lewin, M., N. Carlesso, et al. (2000). "Tat peptide-derivatized magnetic nanoparticles allow in vivo tracking and recovery of progenitor cells." Nat Biotechnol **18**(4): 410-4.
- Lewis, D. L., J. E. Hagstrom, et al. (2002). "Efficient delivery of siRNA for inhibition of gene expression in postnatal mice." Nat Genet **32**(1): 107-8.
- Li, C., M. F. Penet, et al. (2010). "Nanoplex delivery of siRNA and prodrug enzyme for multimodality image-guided molecular pathway targeted cancer therapy." ACS Nano **4**(11): 6707-16.
- Lipton, P. (1999). "Ischemic cell death in brain neurons." Physiol Rev **79**(4): 1431-568.

- Liu, F., Y. Song, et al. (1999). "Hydrodynamics-based transfection in animals by systemic administration of plasmid DNA." Gene Ther **6**(7): 1258-66.
- Liu, G., J. Xie, et al. (2011). "N-Alkyl-PEI-Functionalized Iron Oxide Nanoclusters for Efficient siRNA Delivery." Small.
- Liu, G., X. Yuan, et al. (2006). "Analysis of gene expression and chemoresistance of CD133+ cancer stem cells in glioblastoma." Mol Cancer **5**: 67.
- Liu, L., S. Markowitz, et al. (1996). "Mismatch repair mutations override alkyltransferase in conferring resistance to temozolomide but not to 1,3-bis(2-chloroethyl)nitrosourea." Cancer Res **56**(23): 5375-9.
- Liu, N., H. Ding, et al. (2007). "Radiolabeling small RNA with technetium-99m for visualizing cellular delivery and mouse biodistribution." Nucl Med Biol **34**(4): 399-404.
- Liu, S., G. Zhen, et al. (2009). "Rodent Stroke Model Guidelines for Preclinical Stroke Trials (1st Edition)." J Exp Stroke Transl Med **2**(2): 2-27.
- Liu, Y., X. Y. Hou, et al. (2003). "L-type voltage-gated calcium channel attends regulation of tyrosine phosphorylation of NMDA receptor subunit 2A induced by transient brain ischemia." Brain Res **972**(1-2): 142-8.
- Liu, Y., G. Zhang, et al. (2001). "NMDA receptor activation results in tyrosine phosphorylation of NMDA receptor subunit 2A(NR2A) and interaction of Pyk2 and Src with NR2A after transient cerebral ischemia and reperfusion." Brain Res **909**(1-2): 51-8.
- Longa, E. Z., P. R. Weinstein, et al. (1989). "Reversible middle cerebral artery occlusion without craniectomy in rats." Stroke **20**(1): 84-91.
- Lu, W., G. Zhang, et al. (2010). "Tumor site-specific silencing of NF-kappaB p65 by targeted hollow gold nanosphere-mediated photothermal transfection." Cancer Res **70**(8): 3177-88.
- Lyden, P., M. Jacoby, et al. (2001). "The Clomethiazole Acute Stroke Study in tissue-type plasminogen activator-treated stroke (CLASS-T): final results." Neurology **57**(7): 1199-205.
- Lyons, S. A., J. O'Neal, et al. (2002). "Chlorotoxin, a scorpion-derived peptide, specifically binds to gliomas and tumors of neuroectodermal origin." Glia **39**(2): 162-73.
- Majid, A., Y. Y. He, et al. (2000). "Differences in vulnerability to permanent focal cerebral ischemia among 3 common mouse strains." Stroke **31**(11): 2707-14.

- Manley, G. T., M. Fujimura, et al. (2000). "Aquaporin-4 deletion in mice reduces brain edema after acute water intoxication and ischemic stroke." Nat Med **6**(2): 159-63.
- Marti, H. J., M. Bernaudin, et al. (2000). "Hypoxia-induced vascular endothelial growth factor expression precedes neovascularization after cerebral ischemia." Am J Pathol **156**(3): 965-76.
- Martin, R. L., H. G. Lloyd, et al. (1994). "The early events of oxygen and glucose deprivation: setting the scene for neuronal death?" Trends Neurosci **17**(6): 251-7.
- Mascotti, D. P. and T. M. Lohman (1993). "Thermodynamics of single-stranded RNA and DNA interactions with oligolysines containing tryptophan. Effects of base composition." Biochemistry **32**(40): 10568-79.
- Mayadas, T. N., R. C. Johnson, et al. (1993). "Leukocyte rolling and extravasation are severely compromised in P selectin-deficient mice." Cell **74**(3): 541-54.
- Mayanagi, K., P. V. Katakam, et al. (2008). "Acute treatment with rosuvastatin protects insulin resistant (C57BL/6J ob/ob) mice against transient cerebral ischemia." J Cereb Blood Flow Metab **28**(12): 1927-35.
- McCaffrey, A. P., L. Meuse, et al. (2002). "RNA interference in adult mice." Nature **418**(6893): 38-9.
- McFerrin, M. B. and H. Sontheimer (2006). "A role for ion channels in glioma cell invasion." Neuron Glia Biol **2**(1): 39-49.
- Medarova, Z., W. Pham, et al. (2007). "In vivo imaging of siRNA delivery and silencing in tumors." Nat Med **13**(3): 372-7.
- Merkel, O. M., D. Librizzi, et al. (2009). "In vivo SPECT and real-time gamma camera imaging of biodistribution and pharmacokinetics of siRNA delivery using an optimized radiolabeling and purification procedure." Bioconjug Chem **20**(1): 174-82.
- Mikhaylova, M., I. Stasinopoulos, et al. (2009). "Imaging of cationic multifunctional liposome-mediated delivery of COX-2 siRNA." Cancer Gene Ther **16**(3): 217-26.
- Minakuchi, Y., F. Takeshita, et al. (2004). "Atelocollagen-mediated synthetic small interfering RNA delivery for effective gene silencing in vitro and in vivo." Nucleic Acids Res **32**(13): e109.
- Mirimanoff, R. O., T. Gorlia, et al. (2006). "Radiotherapy and temozolomide for newly diagnosed glioblastoma: recursive partitioning analysis of the EORTC 26981/22981-NCIC CE3 phase III randomized trial." J Clin Oncol **24**(16): 2563-9.

- Mocco, J., T. Choudhri, et al. (2002). "HuEP5C7 as a humanized monoclonal anti-E/P-selectin neurovascular protective strategy in a blinded placebo-controlled trial of nonhuman primate stroke." Circ Res **91**(10): 907-14.
- Mocsai, A., Z. Jakus, et al. (2000). "Kinase pathways in chemoattractant-induced degranulation of neutrophils: the role of p38 mitogen-activated protein kinase activated by Src family kinases." J Immunol **164**(8): 4321-31.
- Mok, H., O. Veiseh, et al. (2010). "pH-Sensitive siRNA nanovector for targeted gene silencing and cytotoxic effect in cancer cells." Mol Pharm **7**(6): 1930-9.
- Moore, A., Z. Medarova, et al. (2004). "In vivo targeting of underglycosylated MUC-1 tumor antigen using a multimodal imaging probe." Cancer Res **64**(5): 1821-7.
- Morris, M. C., J. Depollier, et al. (2001). "A peptide carrier for the delivery of biologically active proteins into mammalian cells." Nat Biotechnol **19**(12): 1173-6.
- Morris, M. C., P. Vidal, et al. (1997). "A new peptide vector for efficient delivery of oligonucleotides into mammalian cells." Nucleic Acids Res **25**(14): 2730-6.
- Morrissey, D. V., J. A. Lockridge, et al. (2005). "Potent and persistent in vivo anti-HBV activity of chemically modified siRNAs." Nat Biotechnol **23**(8): 1002-7.
- Murray, D., N. Ben-Tal, et al. (1997). "Electrostatic interaction of myristoylated proteins with membranes: simple physics, complicated biology." Structure **5**(8): 985-9.
- Nakamura, K., T. Hori, et al. (1993). "Redox regulation of a src family protein tyrosine kinase p56lck in T cells." Oncogene **8**(11): 3133-9.
- Nakase, I., H. Hirose, et al. (2009). "Cell-surface accumulation of flock house virus-derived peptide leads to efficient internalization via macropinocytosis." Mol Ther **17**(11): 1868-76.
- Nakase, I., M. Niwa, et al. (2004). "Cellular uptake of arginine-rich peptides: roles for macropinocytosis and actin rearrangement." Mol Ther **10**(6): 1011-22.
- National Center for Health, S. (2012).
- Naumov, G. N., E. Bender, et al. (2006). "A model of human tumor dormancy: an angiogenic switch from the nonangiogenic phenotype." J Natl Cancer Inst **98**(5): 316-25.
- Ng, Y. S., J. Stein, et al. (2007). "Comparison of clinical characteristics and functional outcomes of ischemic stroke in different vascular territories." Stroke **38**(8): 2309-14.

- Normand, N., H. van Leeuwen, et al. (2001). "Particle formation by a conserved domain of the herpes simplex virus protein VP22 facilitating protein and nucleic acid delivery." J Biol Chem **276**(18): 15042-50.
- Oehlke, J., A. Scheller, et al. (1998). "Cellular uptake of an alpha-helical amphipathic model peptide with the potential to deliver polar compounds into the cell interior non-endocytically." Biochim Biophys Acta **1414**(1-2): 127-39.
- Oehlke, J., G. Wallukat, et al. (2004). "Enhancement of intracellular concentration and biological activity of PNA after conjugation with a cell-penetrating synthetic model peptide." Eur J Biochem **271**(14): 3043-9.
- Ofek, P., W. Fischer, et al. (2010). "In vivo delivery of small interfering RNA to tumors and their vasculature by novel dendritic nanocarriers." FASEB J **24**(9): 3122-34.
- Ohtani, K., H. Tanaka, et al. (2003). "SM-31900, a novel NMDA receptor glycine-binding site antagonist, reduces infarct volume induced by permanent middle cerebral artery occlusion in spontaneously hypertensive rats." Neurochem Int **42**(5): 375-84.
- Omi, K., K. Tokunaga, et al. (2004). "Long-lasting RNAi activity in mammalian neurons." FEBS Lett **558**(1-3): 89-95.
- Oppermann, H., A. D. Levinson, et al. (1979). "Uninfected vertebrate cells contain a protein that is closely related to the product of the avian sarcoma virus transforming gene (src)." Proc Natl Acad Sci U S A **76**(4): 1804-8.
- Oshiro, S., H. Tsugu, et al. (2006). "Evaluation of intratumoral administration of tumor necrosis factor-alpha in patients with malignant glioma." Anticancer Res **26**(6A): 4027-32.
- Osuka, K., P. J. Feustel, et al. (2001). "Tamoxifen inhibits nitrotyrosine formation after reversible middle cerebral artery occlusion in the rat." J Neurochem **76**(6): 1842-50.
- Paciaroni, M., G. Silvestrelli, et al. (2003). "Neurovascular territory involved in different etiological subtypes of ischemic stroke in the Perugia Stroke Registry." Eur J Neurol **10**(4): 361-5.
- Padari, K., P. Saalik, et al. (2005). "Cell transduction pathways of transportans." Bioconjug Chem **16**(6): 1399-410.
- Parmentier, S., G. A. Bohme, et al. (1999). "Selective inhibition of inducible nitric oxide synthase prevents ischaemic brain injury." Br J Pharmacol **127**(2): 546-52.
- Parmentier-Batteur, S., G. A. Bohme, et al. (2001). "Antisense oligodeoxynucleotide to inducible nitric oxide synthase protects against transient focal cerebral ischemia-induced brain injury." J Cereb Blood Flow Metab **21**(1): 15-21.

- Paul, R., Z. G. Zhang, et al. (2001). "Src deficiency or blockade of Src activity in mice provides cerebral protection following stroke." Nat Med **7**(2): 222-7.
- Paz, M. F., R. Yaya-Tur, et al. (2004). "CpG island hypermethylation of the DNA repair enzyme methyltransferase predicts response to temozolomide in primary gliomas." Clin Cancer Res **10**(15): 4933-8.
- Peer, D., P. Zhu, et al. (2007). "Selective gene silencing in activated leukocytes by targeting siRNAs to the integrin lymphocyte function-associated antigen-1." Proc Natl Acad Sci U S A **104**(10): 4095-100.
- Pegg, A. E. (1990). "Mammalian O6-alkylguanine-DNA alkyltransferase: regulation and importance in response to alkylating carcinogenic and therapeutic agents." Cancer Res **50**(19): 6119-29.
- Perez, F., P. M. Lledo, et al. (1994). "Rab3A and Rab3B carboxy-terminal peptides are both potent and specific inhibitors of prolactin release by rat cultured anterior pituitary cells." Mol Endocrinol **8**(9): 1278-87.
- Perez-Asensio, F. J., O. Hurtado, et al. (2005). "Inhibition of iNOS activity by 1400W decreases glutamate release and ameliorates stroke outcome after experimental ischemia." Neurobiol Dis **18**(2): 375-84.
- Pham, W., M. F. Kircher, et al. (2004). "Enhancing membrane permeability by fatty acylation of oligoarginine peptides." Chembiochem **5**(8): 1148-51.
- Pham, W., B. Q. Zhao, et al. (2005). "Crossing the blood-brain barrier: a potential application of myristoylated polyarginine for in vivo neuroimaging." Neuroimage **28**(1): 287-92.
- Phelan, A., G. Elliott, et al. (1998). "Intercellular delivery of functional p53 by the herpesvirus protein VP22." Nat Biotechnol **16**(5): 440-3.
- Plowman, J., W. R. Waud, et al. (1994). "Preclinical antitumor activity of temozolomide in mice: efficacy against human brain tumor xenografts and synergism with 1,3-bis(2-chloroethyl)-1-nitrosourea." Cancer Res **54**(14): 3793-9.
- Pober, J. S., M. P. Bevilacqua, et al. (1986). "Two distinct monokines, interleukin 1 and tumor necrosis factor, each independently induce biosynthesis and transient expression of the same antigen on the surface of cultured human vascular endothelial cells." J Immunol **136**(5): 1680-7.
- Pooga, M., M. Hallbrink, et al. (1998). "Cell penetration by transportan." Faseb J **12**(1): 67-77.
- Potapova, O., H. Fakhrai, et al. (1996). "Platelet-derived growth factor-B/v-sis confers a tumorigenic and metastatic phenotype to human T98G glioblastoma cells." Cancer Res **56**(2): 280-6.

- Pruss, H., K. Prass, et al. (2008). "Inducible nitric oxide synthase does not mediate brain damage after transient focal cerebral ischemia in mice." J Cereb Blood Flow Metab **28**(3): 526-39.
- Puebla, I., S. Esseghir, et al. (2003). "A recombinant H1 histone-based system for efficient delivery of nucleic acids." J Biotechnol **105**(3): 215-26.
- Pulford, B., N. Reim, et al. (2010). "Liposome-siRNA-peptide complexes cross the blood-brain barrier and significantly decrease PrP on neuronal cells and PrP in infected cell cultures." PLoS One **5**(6): e11085.
- Ranson, M., M. R. Middleton, et al. (2006). "Lomeguatrib, a potent inhibitor of O6-alkylguanine-DNA-alkyltransferase: phase I safety, pharmacodynamic, and pharmacokinetic trial and evaluation in combination with temozolomide in patients with advanced solid tumors." Clin Cancer Res **12**(5): 1577-84.
- Resh, M. D. (1999). "Fatty acylation of proteins: new insights into membrane targeting of myristoylated and palmitoylated proteins." Biochim Biophys Acta **1451**(1): 1-16.
- Richard, J. P., K. Melikov, et al. (2005). "Cellular uptake of unconjugated TAT peptide involves clathrin-dependent endocytosis and heparan sulfate receptors." J Biol Chem **280**(15): 15300-6.
- Rosamond, W. D., A. R. Folsom, et al. (1999). "Stroke incidence and survival among middle-aged adults: 9-year follow-up of the Atherosclerosis Risk in Communities (ARIC) cohort." Stroke **30**(4): 736-43.
- Rubenstein, M., M. Shaw, et al. (1999). "In vivo establishment of T98G human glioblastoma." Methods Find Exp Clin Pharmacol **21**(6): 391-3.
- Saalik, P., A. Elmquist, et al. (2004). "Protein cargo delivery properties of cell-penetrating peptides. A comparative study." Bioconjug Chem **15**(6): 1246-53.
- Saar, K., M. Lindgren, et al. (2005). "Cell-penetrating peptides: a comparative membrane toxicity study." Anal Biochem **345**(1): 55-65.
- Santel, A., M. Aleku, et al. (2006). "A novel siRNA-lipoplex technology for RNA interference in the mouse vascular endothelium." Gene Ther **13**(16): 1222-34.
- Sathornsumetee, S. and J. N. Rich (2008). "Designer therapies for glioblastoma multiforme." Ann N Y Acad Sci **1142**: 108-32.
- Sato, T., Y. Morishima, et al. (1999). "DY-9760e, a novel calmodulin antagonist, reduces brain damage induced by transient focal cerebral ischemia." Eur J Pharmacol **370**(2): 117-23.
- Schwarze, S. R., A. Ho, et al. (1999). "In vivo protein transduction: delivery of a biologically active protein into the mouse." Science **285**(5433): 1569-72.

- Shimizu-Sasamata, M., P. Bosque-Hamilton, et al. (1998). "Attenuated neurotransmitter release and spreading depression-like depolarizations after focal ischemia in mutant mice with disrupted type I nitric oxide synthase gene." J Neurosci **18**(22): 9564-71.
- Shuaib, A., K. R. Lees, et al. (2007). "NXY-059 for the treatment of acute ischemic stroke." N Engl J Med **357**(6): 562-71.
- Simeoni, F., M. C. Morris, et al. (2003). "Insight into the mechanism of the peptide-based gene delivery system MPG: implications for delivery of siRNA into mammalian cells." Nucleic Acids Res **31**(11): 2717-24.
- Sioud, M. and D. R. Sorensen (2003). "Cationic liposome-mediated delivery of siRNAs in adult mice." Biochem Biophys Res Commun **312**(4): 1220-5.
- Soriano, S. G., S. A. Lipton, et al. (1996). "Intercellular adhesion molecule-1-deficient mice are less susceptible to cerebral ischemia-reperfusion injury." Ann Neurol **39**(5): 618-24.
- Soroceanu, L., Y. Gillespie, et al. (1998). "Use of chlorotoxin for targeting of primary brain tumors." Cancer Res **58**(21): 4871-9.
- Soutschek, J., A. Akinc, et al. (2004). "Therapeutic silencing of an endogenous gene by systemic administration of modified siRNAs." Nature **432**(7014): 173-8.
- Stein, G. H. (1979). "T98G: an anchorage-independent human tumor cell line that exhibits stationary phase G1 arrest in vitro." J Cell Physiol **99**(1): 43-54.
- Stupp, R., P. Y. Dietrich, et al. (2002). "Promising survival for patients with newly diagnosed glioblastoma multiforme treated with concomitant radiation plus temozolomide followed by adjuvant temozolomide." J Clin Oncol **20**(5): 1375-82.
- Stupp, R., M. E. Hegi, et al. (2009). "Effects of radiotherapy with concomitant and adjuvant temozolomide versus radiotherapy alone on survival in glioblastoma in a randomised phase III study: 5-year analysis of the EORTC-NCIC trial." Lancet Oncol **10**(5): 459-66.
- Stupp, R., W. P. Mason, et al. (2005). "Radiotherapy plus concomitant and adjuvant temozolomide for glioblastoma." N Engl J Med **352**(10): 987-96.
- Subbarao, N. K., R. A. Parente, et al. (1987). "pH-dependent bilayer destabilization by an amphipathic peptide." Biochemistry **26**(11): 2964-72.
- Sugimoto, K. and C. Iadecola (2002). "Effects of aminoguanidine on cerebral ischemia in mice: comparison between mice with and without inducible nitric oxide synthase gene." Neurosci Lett **331**(1): 25-8.

- Sugimoto, K. and C. Iadecola (2003). "Delayed effect of administration of COX-2 inhibitor in mice with acute cerebral ischemia." Brain Res **960**(1-2): 273-6.
- Sugimura, M., H. Takamori, et al. (2005). "DY-9760e, a calmodulin antagonist, reduces brain damage after permanent focal cerebral ischemia in cats." Biol Pharm Bull **28**(4): 629-33.
- Sun, C., C. Fang, et al. (2008). "Tumor-targeted drug delivery and MRI contrast enhancement by chlorotoxin-conjugated iron oxide nanoparticles." Nanomedicine (Lond) **3**(4): 495-505.
- Sun, C., O. Veiseh, et al. (2008). "In vivo MRI detection of gliomas by chlorotoxin-conjugated superparamagnetic nanoprobes." Small **4**(3): 372-9.
- Swanson, R. A., M. T. Morton, et al. (1990). "A semiautomated method for measuring brain infarct volume." J Cereb Blood Flow Metab **10**(2): 290-3.
- Taguchi, T., M. Shimura, et al. (2004). "Nuclear trafficking of macromolecules by an oligopeptide derived from Vpr of human immunodeficiency virus type-1." Biochem Biophys Res Commun **320**(1): 18-26.
- Takabatake, Y., Y. Isaka, et al. (2005). "Exploring RNA interference as a therapeutic strategy for renal disease." Gene Ther **12**(12): 965-73.
- Takagi, K., T. Sato, et al. (2001). "Post-ischemic administration of DY-9760e, a novel calmodulin antagonist, reduced infarct volume in the permanent focal ischemia model of spontaneously hypertensive rat." Neurol Res **23**(6): 662-8.
- Takayama, K., H. Hirose, et al. (2012). "Effect of the attachment of a penetration accelerating sequence and the influence of hydrophobicity on octaarginine-mediated intracellular delivery." Mol Pharm **9**(5): 1222-30.
- Takeshita, F., Y. Minakuchi, et al. (2005). "Efficient delivery of small interfering RNA to bone-metastatic tumors by using atelocollagen in vivo." Proc Natl Acad Sci U S A **102**(34): 12177-82.
- Tao, W., J. P. Davide, et al. (2010). "Noninvasive imaging of lipid nanoparticle-mediated systemic delivery of small-interfering RNA to the liver." Mol Ther **18**(9): 1657-66.
- Theodore, L., D. Derossi, et al. (1995). "Intraneuronal delivery of protein kinase C pseudosubstrate leads to growth cone collapse." J Neurosci **15**(11): 7158-67.
- Thom, T., N. Haase, et al. (2006). "Heart disease and stroke statistics--2006 update: a report from the American Heart Association Statistics Committee and Stroke Statistics Subcommittee." Circulation **113**(6): e85-151.

- Thomas, S. M. and J. S. Brugge (1997). "Cellular functions regulated by Src family kinases." Annu Rev Cell Dev Biol **13**: 513-609.
- Thoren, P. E., D. Persson, et al. (2003). "Uptake of analogs of penetratin, Tat(48-60) and oligoarginine in live cells." Biochem Biophys Res Commun **307**(1): 100-7.
- Torchilin, V. P., T. S. Levchenko, et al. (2003). "Cell transfection in vitro and in vivo with nontoxic TAT peptide-liposome-DNA complexes." Proc Natl Acad Sci U S A **100**(4): 1972-7.
- Torchilin, V. P., R. Rammohan, et al. (2001). "TAT peptide on the surface of liposomes affords their efficient intracellular delivery even at low temperature and in the presence of metabolic inhibitors." Proc Natl Acad Sci U S A **98**(15): 8786-91.
- Troy, C. M., D. Derossi, et al. (1996). "Downregulation of Cu/Zn superoxide dismutase leads to cell death via the nitric oxide-peroxynitrite pathway." J Neurosci **16**(1): 253-61.
- Troy, C. M., L. Stefanis, et al. (1996). "The contrasting roles of ICE family proteases and interleukin-1beta in apoptosis induced by trophic factor withdrawal and by copper/zinc superoxide dismutase down-regulation." Proc Natl Acad Sci U S A **93**(11): 5635-40.
- Vaishnav, A. K., J. Gollob, et al. (2010). "A status report on RNAi therapeutics." Silence **1**(1): 14.
- Vakili, A., H. Kataoka, et al. (2005). "Role of arginine vasopressin V1 and V2 receptors for brain damage after transient focal cerebral ischemia." J Cereb Blood Flow Metab **25**(8): 1012-9.
- van Bruggen, N., H. Thibodeaux, et al. (1999). "VEGF antagonism reduces edema formation and tissue damage after ischemia/reperfusion injury in the mouse brain." J Clin Invest **104**(11): 1613-20.
- Vandonselaar, M., R. A. Hickie, et al. (1994). "Trifluoperazine-induced conformational change in Ca(2+)-calmodulin." Nat Struct Biol **1**(11): 795-801.
- Veenman, L., E. Levin, et al. (2004). "Peripheral-type benzodiazepine receptor density and in vitro tumorigenicity of glioma cell lines." Biochem Pharmacol **68**(4): 689-98.
- Veiseh, M., P. Gabikian, et al. (2007). "Tumor paint: a chlorotoxin: Cy5.5 bioconjugate for intraoperative visualization of cancer foci." Cancer Res **67**(14): 6882-8.
- Veiseh, O., F. M. Kievit, et al. (2010). "Chlorotoxin bound magnetic nanovector tailored for cancer cell targeting, imaging, and siRNA delivery." Biomaterials **31**(31): 8032-42.

- Veiseh, O., C. Sun, et al. (2009). "Specific targeting of brain tumors with an optical/magnetic resonance imaging nanoprobe across the blood-brain barrier." Cancer Res **69**(15): 6200-7.
- Veiseh, O., C. Sun, et al. (2005). "Optical and MRI multifunctional nanoprobe for targeting gliomas." Nano Lett **5**(6): 1003-8.
- Vemuganti, R., R. J. Dempsey, et al. (2004). "Inhibition of intercellular adhesion molecule-1 protein expression by antisense oligonucleotides is neuroprotective after transient middle cerebral artery occlusion in rat." Stroke **35**(1): 179-84.
- Viel, T., R. Boisgard, et al. (2008). "Molecular imaging study on in vivo distribution and pharmacokinetics of modified small interfering RNAs (siRNAs)." Oligonucleotides **18**(3): 201-12.
- Vives, E., P. Brodin, et al. (1997). "A truncated HIV-1 Tat protein basic domain rapidly translocates through the plasma membrane and accumulates in the cell nucleus." J Biol Chem **272**(25): 16010-7.
- Wadia, J. S., R. V. Stan, et al. (2004). "Transducible TAT-HA fusogenic peptide enhances escape of TAT-fusion proteins after lipid raft macropinocytosis." Nat Med **10**(3): 310-5.
- Wahlestedt, C., E. Golanov, et al. (1993). "Antisense oligodeoxynucleotides to NMDA-R1 receptor channel protect cortical neurons from excitotoxicity and reduce focal ischaemic infarctions." Nature **363**(6426): 260-3.
- Wang, J., Y. Zhao, et al. (2011). "Progesterone inhibits inflammatory response pathways after permanent middle cerebral artery occlusion in rats." Mol Med Report **4**(2): 319-24.
- Wang, Y. F., S. E. Tsirka, et al. (1998). "Tissue plasminogen activator (tPA) increases neuronal damage after focal cerebral ischemia in wild-type and tPA-deficient mice." Nat Med **4**(2): 228-31.
- Washbourne, P. and A. K. McAllister (2002). "Techniques for gene transfer into neurons." Curr Opin Neurobiol **12**(5): 566-73.
- Watson, A. J. and G. P. Margison (1999). O6-Alkylguanine-DNA alkyltransferase assays. Cytotoxic Drug Resistance Mechanisms. R. Brown and B.-B. U. Totowa, NJ, Humana Press: 167-178.
- Weller, M., R. Stupp, et al. (2010). "MGMT promoter methylation in malignant gliomas: ready for personalized medicine?" Nat Rev Neurol **6**(1): 39-51.
- Wolman, M., I. Klatzo, et al. (1981). "Evaluation of the dye-protein tracers in pathophysiology of the blood-brain barrier." Acta Neuropathol **54**(1): 55-61.

- Wu, S., N. Tamaki, et al. (1998). "Reactive oxygen species in reoxygenation injury of rat brain capillary endothelial cells." Neurosurgery **43**(3): 577-83; discussion 584.
- Wyman, T. B., F. Nicol, et al. (1997). "Design, synthesis, and characterization of a cationic peptide that binds to nucleic acids and permeabilizes bilayers." Biochemistry **36**(10): 3008-17.
- Xiong, X. B. and A. Lavasanifar (2011). "Traceable Multifunctional Micellar Nanocarriers for Cancer-Targeted Co-delivery of MDR-1 siRNA and Doxorubicin." ACS Nano **5**(6): 5202-13.
- Xu, Y. and F. C. Szoka (1996). "Mechanism of DNA release from cationic liposome/DNA complexes used in cell transfection." Biochemistry **35**: 5616-23.
- Yagi, N., I. Manabe, et al. (2009). "A nanoparticle system specifically designed to deliver short interfering RNA inhibits tumor growth in vivo." Cancer Res **69**(16): 6531-8.
- Zhang, G. J., M. Safran, et al. (2004). "Bioluminescent imaging of Cdk2 inhibition in vivo." Nat Med **10**(6): 643-8.
- Zhang, R. L., M. Chopp, et al. (1996). "E-selectin in focal cerebral ischemia and reperfusion in the rat." J Cereb Blood Flow Metab **16**(6): 1126-36.
- Zhang, Z., M. Chopp, et al. (1997). "A mouse model of embolic focal cerebral ischemia." J Cereb Blood Flow Metab **17**(10): 1081-8.
- Zhang, Z. G., L. Zhang, et al. (2000). "VEGF enhances angiogenesis and promotes blood-brain barrier leakage in the ischemic brain." J Clin Invest **106**(7): 829-38.
- Zhao, X., C. Haensel, et al. (2000). "Gene-dosing effect and persistence of reduction in ischemic brain injury in mice lacking inducible nitric oxide synthase." Brain Res **872**(1-2): 215-8.
- Zimmermann, T. S., A. C. Lee, et al. (2006). "RNAi-mediated gene silencing in non-human primates." Nature **441**(7089): 111-4.